Master Thesis in Geosciences

Unsaturated soils and rainfall induced landslides

Jean-Sébastien L'Heureux

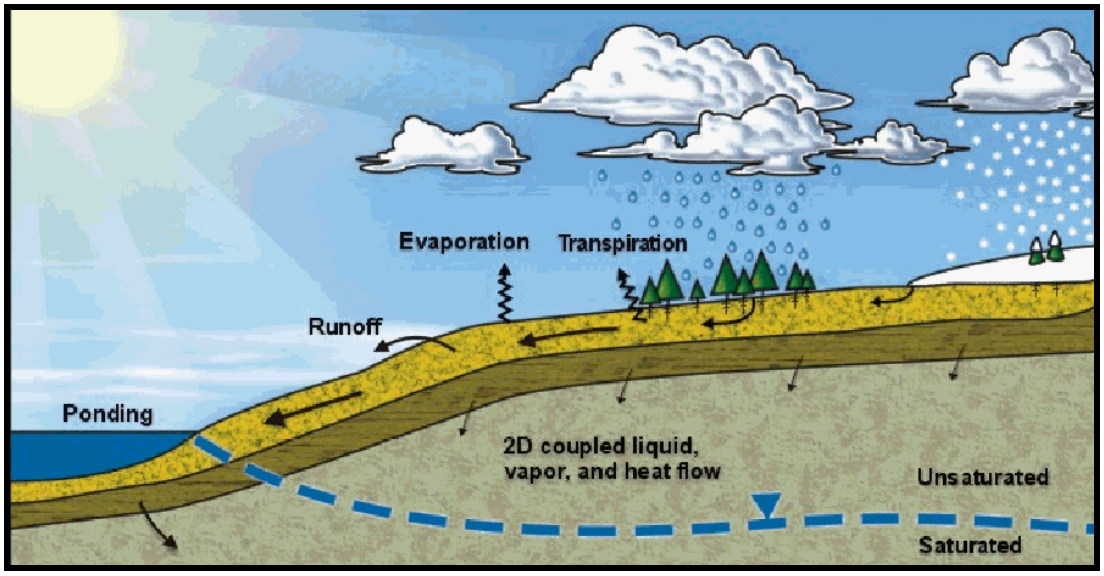

UNIVERSITY OF OSLO
FACULTY OF MATHEMATICS AND NATURAL SCIENCES

Unsaturated soils and rainfall induced landslides

Jean-Sébastien L'Heureux

Master Thesis in Geosciences

Discipline: Environmental Geology and Geohazards

Department of Geosciences

Faculty of Mathematics and Natural Sciences

UNIVERSITY OF OSLO

June 2005

Tutor(s): Kaare Høeg

This work is published digitally through DUO – Digitale Utgivelser ved UiO

http://www.duo.uio.no

It is also catalogued in BIBSYS (http://www.bibsys.no/english)

Cover Photo: Physical processes related to seepage in a slope (from Krahn 2004/Vadose zone modeling with VADOSE/W, Geo-Slope International Ltd.)

Acknowledgements

This master's thesis work started in the spring of 2004. This work is linked to the Unsaturated Soils and Rain-Induced Landslides project at the International Centre for Geohazard (ICG). The objective of the thesis was to characterise the important parameters for the assessment of rainfall-induced landslides and, especially the hydraulic behaviour of unsaturated soils.

This thesis could not have been completed without the generous assistance and contributions from many sources. The author acknowledges the financial support provided by the ICG during the whole duration of is work.

Successful completion of this thesis was greatly facilitated by the assistance of many individuals. Special thanks go to my supervisor, Professor Kaare Høeg, for the many encouragements, good advices and comments throughout my thesis work. I am particularly grateful to Øyvind A. Høydal and Håkon Heyerdahl at the Norwegian Geotechnical Institute (NGI) for the many discussions, the practical advices and all the help they provided. Thanks to Karsten Müller for helping with the geophysical investigations in the summer 2004 and to the department of Geosciences at the UIO, particularly Svein-Erik Hamran, for providing with the geophysical instruments. I am also thankful to the many persons working in the NGI laboratory. Your help during my long lasting experiments was more than appreciated.

Finally, I wish to thank my dear and love Anette. Thanks for your long-standing support, the many encouragements and for being there for me at all time.

Jean-Sébastien L'Heureux

Oslo, June 2005

"An education isn't how much you have committed to memory, or even how much you know. It's being able to differentiate between what you do know and what you don't."

Anatole France
French novelist (1844 - 1924)

Abstract

Seepage and slope stability issues concerning infiltration in unsaturated slopes are investigated and presented. 2-D finite element analyses are used to study the effects of the different hydraulic characteristics of a fine and coarse grain soil. The influence of the saturated coefficient of permeability (k_s), the air entry-value (a) and the desaturation coefficient (n) are studied. The results are showing how the changes in negative pore-water pressures in the model slope are controlled by the hydraulic properties of the soil and the initial conditions within the slope. For the coarse soil, the zero pore-water pressure surface moves gradually upslope with time. In the fine grain soil model, the rate of suction loss is nearly the same at the toe, in the middle and at the top of the slope. These different infiltration patterns are leading to different types of failure surfaces. For a coarse grain soil, slip may initiate at the foot of the slope as a consequence of positive pore pressure build-up. The fine soil model is prone to a loss of matric suction along its entire length. In this case, the infiltration pattern may lead to shallow translational type of sliding. It is also found that the geometry of the slope affects more the pore pressure distribution in a coarse grain soil than in a fine grain one.

Rainfall-induced landslides in unsaturated soils are frequent in the tropical and subtropical regions of the world. However, temperate regions are also prone to this type of failure and are attracting increasing attention of the geotechnical community. In these regions, natural slopes are constantly subjected to changing environment; from dry summer period to rainy fall and from cold winter to wet spring. The majority of these slopes can be considered as being unsaturated during normal conditions.

A numerical back-calculation of a landslide in the small community of Åmot in Norway is performed in this thesis. The 38 degree slope failed in November 2000 after an extremely wet fall. The landslide threatened and endangered more than 24 houses and their residents. To analyse this failure, the author determined the SWCC of the soil in the laboratory, and geophysical investigations on the slope during the summer 2004 to determine groundwater level and water contents.

In the 2-D finite element analyses, the rate of infiltration was based on meteorological data for a normal year and for the year of 2000.The modelled slope is found to be stable under normal rainfall conditions but failed when subjected to the rainfall conditions of the year 2000. The calculations are showing that the failure is due to a lowering of the suction and frictional strength during the intense rainfall. The calculated time to failure is in agreement with the observed failure and shows that the event could have been predicted.

Table of Contents

List of Appendices

List of Figures

CHAPTER 1 Introduction

Landslides constitute a major threat to both lives and property worldwide. One of the most common triggering mechanisms for landslides is rainfall and the consequent water infiltration. Rainfall induced landslides are mainly related to tropical and subtropical regions and are the results of a change in the groundwater conditions, especially in the unsaturated zone. This type of landslides also occurs in the temperate regions of the world when periods of extreme rain and/or rapid snowmelt take place.

During and after extreme periods of rainfall, deep-seated rotational and shallow translational slides can often be observed in slopes which used to be stable under normal rainfall conditions. The general assumption is that the water infiltration is the direct cause of these slope failures. Deep-seated slides will be generated by a rise in the groundwater level and consequently an increase in pore-water pressures and a lowering of the effective stresses in the soil. In this case, the failure surface will often be located below the phreatic line. This type of sliding occurs in fine-grained clayey soils conditions.

On the other hand, the mechanism for triggering shallow translational slides is somewhat different. This type of sliding is mainly triggered in the zone above the groundwater level in silty/sandy soils. The thickness of this zone depends much on the climatic conditions of the area. It can be of the order of a meter in temperate regions and up to tens of meters in tropical and subtropical regions. Once the rain-water starts infiltrating this vadose zone of the soil, the negative pore-water pressures will tend to dissipate due to an increase in the soil water-content. This process contributes to lowering the shear strength of the soil layers close to the surface. Under critical conditions, the shear strength of the soil can be reduced below the mobilized shear stress on a potential slip surface and failure of the slope may occur.

In temperate regions, natural slopes are constantly subjected to changing environment and climate; from dry summer period to rainy fall and from cold winter to wet spring. The majority of these slopes can be considered unsaturated during normal conditions. Due to this unsaturated state, the slopes can often be found at angles steeper than what would be “theoretically possible” by using the common saturated soil mechanics. In practice, most of the slope stability calculations are neglecting any suction present above the groundwater table.

The difficulties associated with the measurement of negative pore-water pressures and their incorporation into the slope stability analysis is the primary reason for this practice (Fredlund and Rahardjo 1993). It is difficult to predict the stability of a natural slope subjected to environmental changes due to the many factors involved in the process such as the soil hydraulic properties, climatic data and the initial groundwater conditions within the slope. Neglecting the negative pore-water pressures can be reasonable in many situations where the slip surface is mainly lying below the phreatic line. However, for situations where the groundwater level is deep and/or shallow sliding is of concern, negative pore-water pressures should not be ignored.

The goal of the present thesis is to evaluate the effects of principal parameters in the assessment of natural slope hazards subjected to environmental changes. Chapter 2 reviews the hydraulic properties of unsaturated soils and the principal mechanisms controlling the flow of water in the vadose zone. The shear strength of unsaturated soils is also discussed. In Chapter 3 and 4 numerical simulations using the finite element method are used to study the effects of the different hydraulic characteristics of a fine and coarse grain soil. The influence of the saturated coefficient of permeability (k_s), the magnitude of the infiltration flux (q_b), the antecedent rainfall (q_a), the air entry-value (a), the desaturation coefficient (n) and the geometry of the slope are studied and discussed (Chapter 5).

In Chapter 6 a specific case study is presented. A numerical back-calculation of a landslide in the small community of Åmot in Norway is performed. To correctly model this failure, the hydraulic characteristics of the sandy soil are studied by the author in the laboratory and the results are presented. Many months of laboratory testing were necessary in order to accurately define the hydraulic characteristics of the soil. Geophysical investigations were also carried out by the author on the slope during the summer of 2004 to study in-situ conditions. Results from these are presented and used in the back-calculation.

CHAPTER 2 Behaviour of Unsaturated Soils

2.1 Hydraulic Properties

To study the stability of natural slopes subjected to extreme rainfall, one needs knowledge of the pore pressures in normal conditions in addition to those during and after the event. The pore-water pressures, together with the shear strength parameters, govern the stability of a slope. In unsaturated soils, pore-water pressures are dependent upon the flux of water infiltration and upon the hydraulic properties of the soil. As stated by Zhan and Ng (2004), the most important hydraulic parameters for unsaturated soils are the storage capacity characterized by the soil-water characteristic curve and the water coefficient of permeability of the soil. These hydraulic parameters are defined in the present chapter.

2.1.1 Soil water storage

A soil consists of a combination of grain solid particles and interstitial voids. The pore space or voids can either be filled with water or air, or a mixture of both. In a saturated soil, the pore space is entirely filled with water and its volumetric water content (θ_w) is then equal to its porosity (ϕ):

$$\theta_w = \phi \cdot S_r \qquad \textbf{Equation 2-1}$$

where S_r is the degree of saturation which is equal to 100% in a saturated soil. In an unsaturated soil, the volume of water stored within the soil depends upon the negative pressure or suction within the pores. This negative pressure can be varying with time and space in the soil. A function is therefore required to describe the changes in water content related to different suction pressures in the soil. The soil-water characteristic curve[1] (SWCC) can be viewed as the continuous sigmoidal function describing the amount of water in the soil as it is subjected to changes in soil matric suction (Figure 2-1). The amount of water is usually

[1] In the literature, the SWCC may also be referred to as the retention curve or the volumetric water content curve.

defined as either the volumetric water content (θ_w), the gravimetric water content (w) or the degree of saturation (S_r). On the other hand, the matric suction (ψ) is generally described as the difference between the air and the water pressure ($\psi = \mu_a - \mu_w$)[2].

The SWCC gives an idea of the pore size distribution of the soil and important information concerning the hydraulic as well as the mechanical characteristics and behaviour of soils when unsaturated (Leroueil and Hight 2003). This curve is required in order to solve transient problems associated with the vadose zone. Many soil properties can be related to the soil-water characteristic curve such as the shear strength of the soil, the coefficient of permeability and the water volume storage (Sillers et al. 2001) which are the most important in this study.

Figure 2-1 presents a typical plot of a SWCC for fine sand. The main curve on this plot is the desorption curve, or also called the drying curve (dark curve). This one is defined by progressively drying the saturated soil sample and measuring the water content for different matric suction levels.

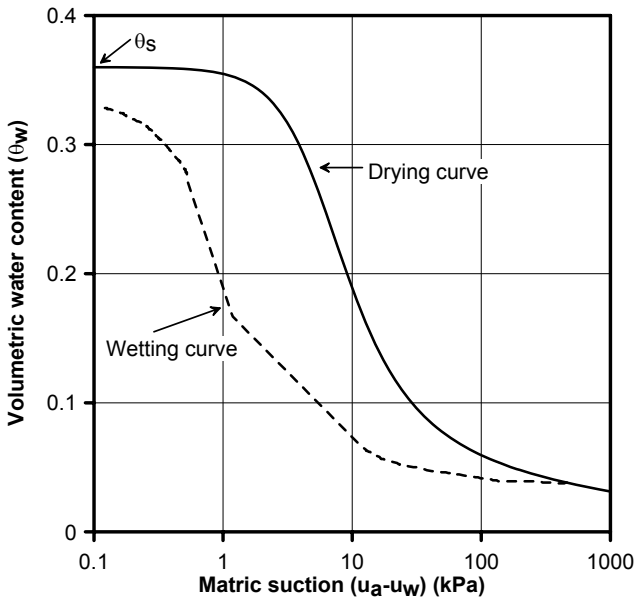

Figure 2-1: Soil-water characteristic curve showing the hydraulic hysteresis.

[2] There are several terms used interchangeably in the literature describing the matric suction of the soil. In this thesis, the term suction will refer to the matric suction (also known as capillary pressure) of a soil (μ_a - μ_w), where μ_a is the pore-air pressure and μ_w is the pore-water pressure.

Upon wetting of the sample, one gets the wetting curve or adsorption curve. As shown in Figure 2-1, this results in a hysteresis. During wetting, some air gets trapped in the soil and therefore the volumetric water content tends towards a lower value than it had initially.

Three different stages (Figure 2-2) can be defined during the process of desaturation (Sillers et al. 2001):

1. *Capillary saturation zone*: It is characterized by a relatively saturated soil sample due to capillary forces. This zone extends up until it reaches the air entry value or also called the bubbling pressure or displacement pressure. This point marks the matric suction value where air starts to enter the largest pores of the soil. It can also be considered as a measure of the maximum pore size in the soil.

2. *Desaturation zone or funicular zone*: The rate of desaturation with respect to an increase in matric suction is greatest in this section (Fredlund et al. 1995). This zone is therefore of great concern in unsaturated soils. The desaturation zone lies between the air-entry value and the residual water content where the liquid phase becomes discontinuous. In this region, water within the pores is increasingly displaced by air. The slope of this zone refers to the desaturation coefficient[3] (n).

3. *Zone of residual saturation*: At this stage, the pore-water becomes essentially immobile within the soil matrix. There is little hydraulic flow in this region and moisture movement results principally from vapour flow. In this residual zone, the suction can be regarded as the energy required to extract water from a unit mass of soil. The suction at which the water content of all soils approach zero is approximately 10^6 kPa (Fredlund and Xing 1994, Sillers et al. 2001). The intersection point between the tangent of the desaturation zone and the residual zone defines the residual water content (θ_r).

These stages are shown in Figure 2-2 which presents a SWCC for a silty soil. On this figure, the water storage capacity of the soil is defined as being the difference between the saturated

[3] The desaturation coefficient is also expressed with the symbol α in the literature.

and residual volumetric water content (θ_s-θ_r). It is a measurement of the maximum amount of water that can be absorbed or desorbed by capillary action (Zhan and Ng 2004).

The SWCC of a soil reflects its pore size distribution. It varies with the void ratio, the grain size distribution and the fabric of a soil. Figure 2-3 shows typical SWCC for a clay, silt and sand. One can observe that the air-entry value increases with the soil particles getting finer. It also increases with the plasticity of the soil. In addition, the desaturation zone is steeper for a coarser material (i.e. α is greater for coarser material). Generally the value of the water storage capacity increases with pore sizes (Vanapalli et al. 1998).

It is shown in the literature that a soil can have different SWCC for a given void ratio. Figure 2-4 shows this example illustrated for a glacial till having the same void ratio, but different fabrics due to compaction on the dry and wet side of optimal conditions. In this case, for the same soil, one can get differences in the air-entry value of one order of magnitude. The SWCC should therefore, except for coarse and clean material, not be seen as an intrinsic characteristic of a soil (Leroueil and Hight 2003). Other factor such as stress history also affects the soil-water characteristic curves (Fredlund and Xing 1994).

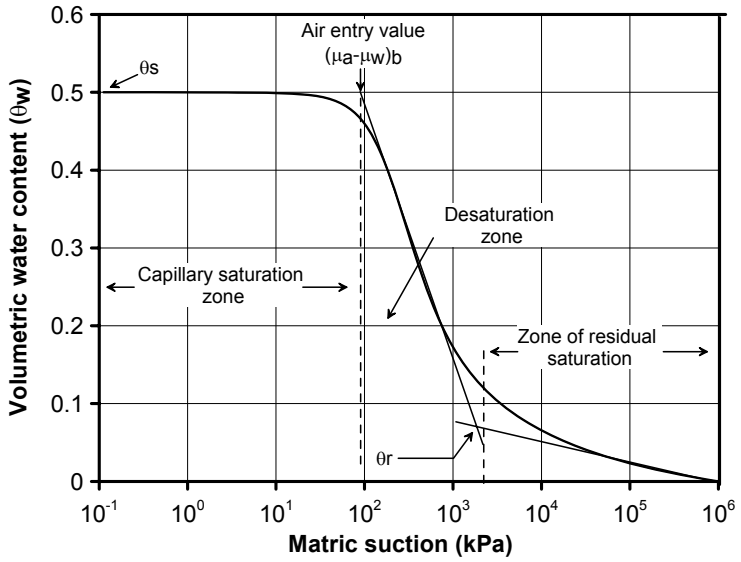

Figure 2-2: Typical SWCC curve for a silty soil illustrating the stages of desaturation (after Sillers et al. 2001).

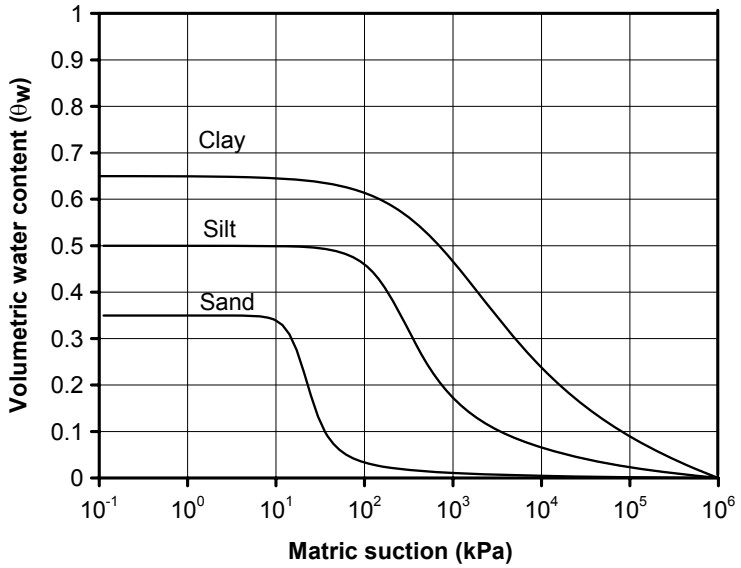

Figure 2-3: Typical soil-water characteristic curves for clay, silt and sand material.

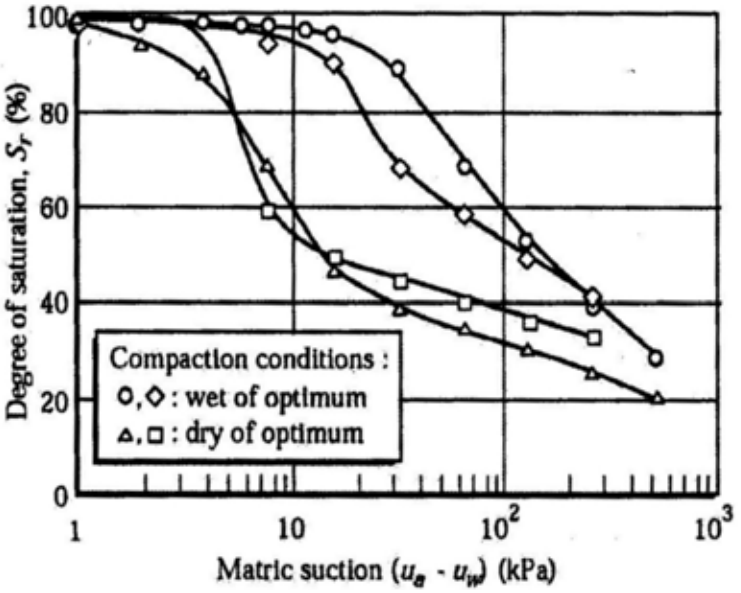

Figure 2-4: Soil-water characteristic curves of LG2 till compacted at different conditions (from Leroueil and Hight 2003, after Watabe et al. 2000).

The SWCC can be defined experimentally by laboratory measurements. These measurements are difficult to realize and time consuming in general. In addition, the results for a given material can vary widely for the many reasons described above. The SWCC can also be determined from empirical models (Arya and Paris 1981 and Aubertin et al. 2003) using the grain size distribution curve, the volumetric water content at saturation and the liquid limit for fine grain soils. Below is described the technique which is used in this study to experimentally calculate the SWCC of a fine sand. The experimental results are presented later in connection with the case study of Chapter 6.

Calculation of SWCC in the laboratory

Different types of apparatus can be used to predict the SWCC in practice. In this thesis, the *1400 Tempe Pressure Cell from the SoilMoisture Corp*. is used to calculate the moisture characteristics of the soils. This equipment provides a simple however time consuming, method to determine the moisture-retention curves of undisturbed soil in the 0-1 bar range (10^5 Pa). The total assemblage is shown in Figure 2-5 and a cross-sectional view of the cell is presented in Figure 2-6. This apparatus was assembled for the first time in the laboratory of the Norwegian Geotechnical Institute (NGI) by the author during the summer of 2004. Much time was needed to calibrate and test the apparatus.

A test is started by fully saturating the high air-entry disc with a vacuum desiccator and distilled water. The drain tube of the cell is connected to a levelling bulb and the water level is adjusted to the height of the bottom of the cell. Once the porous ceramic plate is saturated, it is reinstalled in the cell and the levelling bulb is raised to the top of the plate. No free water should be present on the filter. One should weigh the cell at this stage. The soil specimen is then placed on the air-entry disc by gently twisting the brass cylinder down passed the "O" ring. Good contact between the soil and the disc is important. The soil specimen is then saturated by raising the bulb to the same height as the top of the sample. This stage should be done gradually (1-2 days) to avoid disturbance and bubbling in the soil. Excess water should be removed from the specimen. Weighing the cell at this stage gives the weight of the cell and the saturated soil. The matric suction is thereafter set to the desired level. This can be done in two ways as described below.

The first method is to lower the levelling bulb connected to the cells. This will lower the water pressure (μ_w) while the air pressure (μ_a) is kept constant at the atmospheric value. An

increase in the suction term ($\mu_a - \mu_w$) will then follow. In this thesis, this method was used until a suction of 10 kPa (1m of water) was reached. With this method the suction can be controlled with high accuracy (0.1 kPa).

The second method to control the matric suction is to keep the pore-water pressure constant and increase the air pressure. As shown on Figure 2-5, air pressure is generated by connecting the cells to a constant flow of air. A low pressure air source was used from the NGI system. With the manometer on the Tempe Pressure Cell apparatus, the air pressure could be regulated with ca. 2 kPa accuracy.

By applying air pressure, water will start draining through the air-entry disc. Equilibrium is reached when the suction inside the sample is equal to the applied pressure. At a given equilibrium stage, water will stop flowing out of the specimen and the weigh of the cell will reach a constant value. One must weigh the cells each time equilibrium is reached. By repeating this process at higher pressure values, one can note the difference in weight from one soil suction to another.

After testing the specimen under the highest pressure, the water content corresponding to this pressure is measured by oven-drying the sample. Together with the earlier change in weigh, this water content is used to back-calculate the water contents corresponding to the previously applied suctions. The soil-moisture characteristic curve can then be determined by plotting the calculated matric suction as function of their related volumetric water content:

$$\theta_w = \frac{V_w}{V_{tot}} \qquad \textbf{Equation 2-2}$$

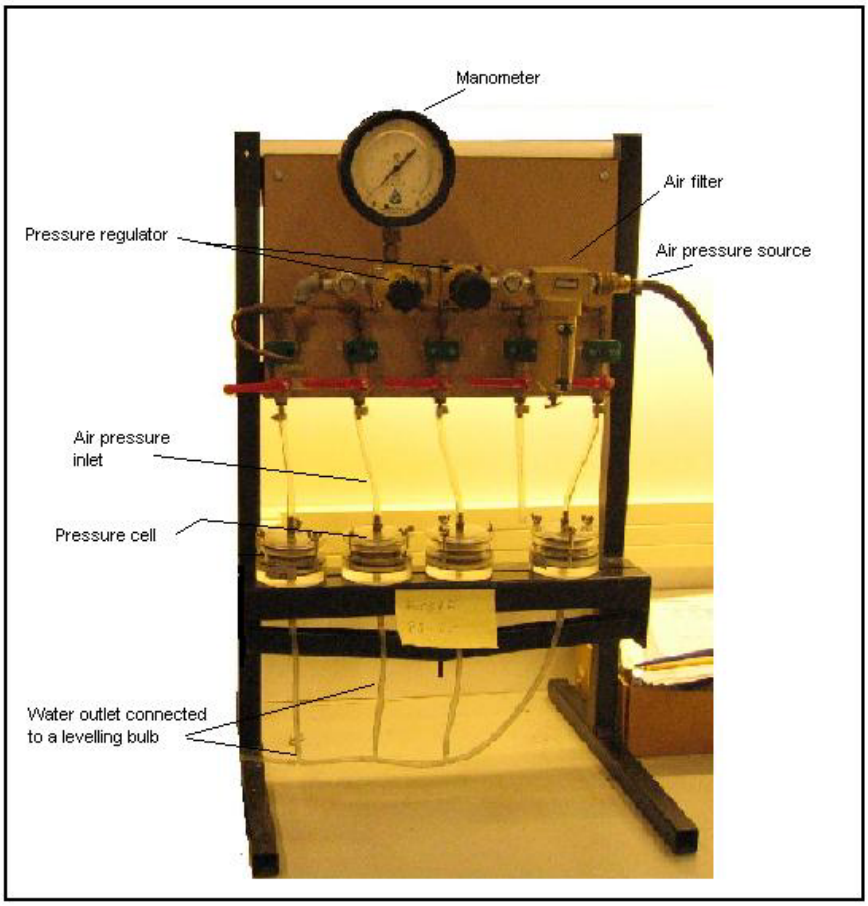

Figure 2-5 Tempe Pressure Cell assemblage.

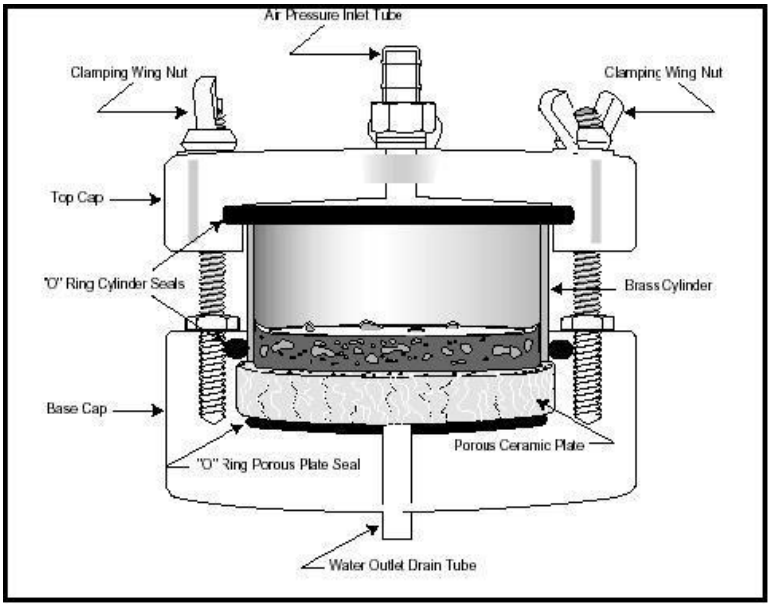

Figure 2-6: Cross-sectional view of Tempe cell with sample (Soil moisture equipment corp.)

Equation for SWCC

The soil-water characteristic curve is one of the most important hydraulic parameters for unsaturated soils. In fact, it is used as the basis for the prediction of other soil parameters, such as permeability and the shear strength function. It is therefore important to have a reasonably accurate characterization of the soil-water characteristic curve (Fredlund and Xing 1994). Numerous empirical equations have been proposed to describe the SWCC. However, the majority of these equations are only applying to a specific group of soils.

In 1994, Fredlund and Xing proposed an equation providing a good fit for sand, silt and clay soils over the entire suction range from 0 to 10^6 kPa. In their equation, the authors are assuming that the shape of the SWCC is dependent upon the pore-size distribution of the soil. Their equation, which gives a relationship between volumetric water content and soil matric suction, is presented hereby:

$$\theta_w = C(\psi)\frac{\theta_s}{\left\{\ln\left[e + (\psi / a)^n\right]\right\}^m} \qquad \textbf{Equation 2-3}$$

where:

C(ψ) = is a correction function defined as $C(\psi) = \dfrac{\ln(1 + \psi / \psi_r)}{\ln\left[1 + (1\,000\,000/\ \psi_r)\right]}$

ψ_r = is the suction corresponding to the residual water content (θ_r) and,

θ_s = the saturated volumetric water content.

The correction function C(ψ) is used in order to have an upper limit to Equation 2-3. This one forces the curve to go through zero when the suction reaches 10^6 kPa. As stated earlier, experimental data have shown that the suction of a soil reaches a maximum value of approximately 10^6 kPa at a volumetric water content approaching zero. In Equation 2-3 the parameters *a, m, n* are curve fitting parameters. The parameter *a* can be closely related to the air–entry value when *m* and *n* are fixed as seen on Figure 2-7 A. The parameter *m* controls the slope of the SWCC in the high suction range, when the soil enters the zone of residual saturation as seen in Figure 2-7 B. In addition, it can be seen on Figure 2-7 C that the parameter *n* controls the slope of the SWCC. High values of *n* produce a sharp corner near the air-entry value.

The *a, m* and *n* parameters are defined as follow for the Fredlund and Xing (1994) model:

$$a = \psi_i \qquad \textbf{Equation 2-4}$$

$$m = 3.67 \ln\left[\frac{\theta_s \cdot C(\psi_i)}{\theta_i}\right] \qquad \textbf{Equation 2-5}$$

$$n = \frac{1.31^{m+1}}{m \cdot \theta_s} 3.72 s \psi_i \qquad \textbf{Equation 2-6}$$

where:

ψ_i = is the suction value located at the inflection point of the SWCC, and

s = the slope of the tangent line on the semi log plot of the SWCC = $\frac{\theta_i}{\ln(\psi_p / \psi_i)}$.

It is important to understand that this model is only functional having knowledge of the *a, m* and *n* fitting parameters. These can be determined using a nonlinear regression procedure outlined by Fredlund and Xing (1994). This closed form equation model is not predicting the SWCC from the grain size distribution curve. It is rather giving a smooth function of the volumetric water content over the desired matric suction range. The model is based primarily on the pore size distribution of soils.

Typical values of the air-entry parameter *a*, the desaturation parameter *n* and the desaturation parameter *m* in the high suction range are given in Table 2-1. These are computed for clay, silt, sand and till materials. Typical values of these parameters for tropical soils are also given.

In order to build Table 2-1, the author studied over 40 SWCC from different sources (Fredlund and Rahardjo 1993, Fredlund and Xing 1994, Fredlund et al. 1995, Tami et al. 2004 and from the SEEP/W function library). The parameters were calculated directly from the experimental results in some cases, while they were explicitly given in other references. More detailed data for these parameters are given in Appendix A.

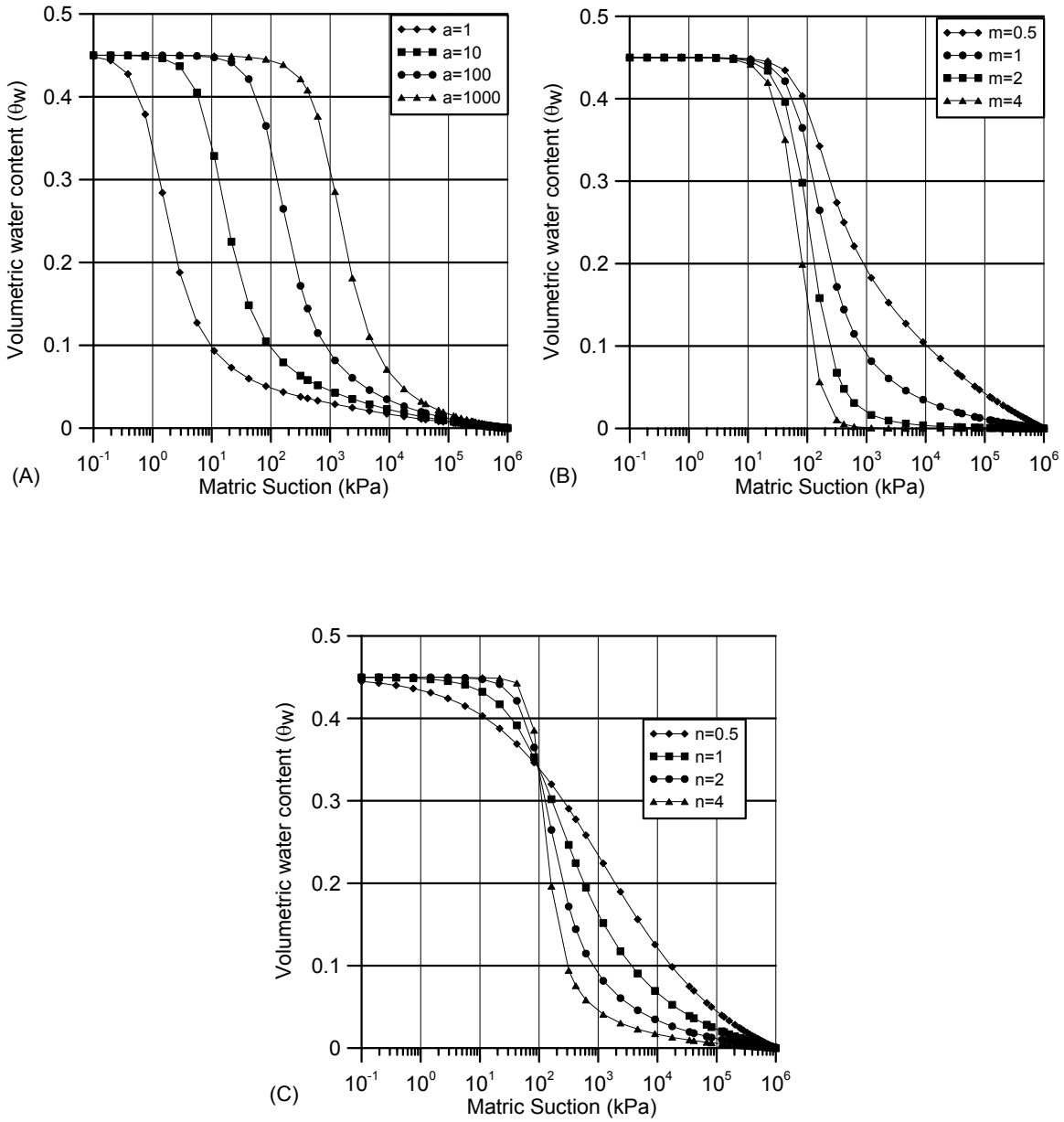

Figure 2-7 (A-B-C): Sample plots of Equation 1-3 to show the effect of the parameters a, m and n on the SWCC (after Fredlund and Xing 1994).

Table 2-1: Range of typical (a, m, n) parameter values for different soil types.

Soil	Parameter range					
	a_{min}	a_{max}	n_{min}	n_{max}	m_{min}	m_{max}
Clay	11	15150	0,04	5,5	0,3	1,14
Silt	2,7	248	1,4	8,1	0,45	1,74
Sand	0,95	148	0,50	12,1	0,32	2,0
Till	20	427	0,61	17,35	0,05	10,6
	a		**n**		**m**	
Gravelly Sand	0,18		4,44		1,13	
Decomposed Tuff (Hong Kong)	110		2		10	
Decomposed granite (Hong Kong)	3		2,4		0,35	
Colluvium (Hong Kong)	0,1		2,2		0,25	

2.1.2 Permeability of soils (k_w)

In the middle of the 18th century, H. Darcy performed his classical experiments studying the flow properties of water through a sand filter. Darcy showed that the flow rate of water (υ_w) passing through the soil was proportional to the hydraulic head gradient ($i = \frac{\partial h_w}{\partial y}$) and a constant known today as Darcy's coefficient of permeability or hydraulic conductivity (k_w). Is experiment led to the very well known Darcy's law:

$$\upsilon_w = k_w \frac{\partial h_w}{\partial y} \qquad \textbf{Equation 2-7}$$

The coefficient of permeability (k_w) is constant for a specific saturated soil and can also be written for the x- and z-directions. This property of the soil is mainly dependent on the size distribution of the soil particles, the properties of the pore fluid, the void ratio of the soil and the fabric of the soil. Water flow through unsaturated soils (defined later in Section 2.2) is also governed by the same physical law as mentioned above. The major difference is that the coefficient of permeability for unsaturated soils cannot be assumed as constant. This coefficient is predominantly a function of the water content or the capillary pressure.

Water in unsaturated soil can be visualized as only flowing through the pore space filled with water. Consequently, the air-filled pores are non-conductive channels to the flow of water. With an increase in matric suction, air replaces the water in the larger pores leading the flow of water to the smaller pores. This results in a higher tortuosity for the flow of water and leads to a decrease in permeability of the soil.

It can often be assumed that the properties of the pore fluid and the void ratio of a given soil are constant under a given flow pattern. In this case, the coefficient of permeability in the unsaturated soil is considered to be uniquely related to the volumetric water content (θ_w). This relationship exhibits no hysteresis (Fredlund and Rahardjo 1993). However, this is not the case for the relationship between the coefficient of permeability and the matric suction (μ_a-μ_w) of the soil. Since there is a hysteresis between the water content and the soil stress state (μ_a-μ_w), there will also be a hysteresis between the coefficient of permeability and matric suction.

Figure 2-8 presents a general trend of hydraulic conductivity curves for clayey and sandy soils. As illustrated, the saturated permeability of the sandy soil is typically greater than that of the clayey soil. However, the unsaturated permeability of the sandy material decreases faster with matric suction and eventually becomes lower than the clayey material. This fact can be attributed to the higher desaturation coefficient of sandy material in comparison to clayey material shown earlier in Figure 2-3.

The hydraulic conductivity is a particularly important parameter when attempting to obtain a reliable flow analysis of water in soils. It can be seen as a measure of its capacity to allow the flow of water through the pore spaces between the soil particles. Techniques to determine this parameter for saturated and unsaturated soils are defined in the subsequent sections.

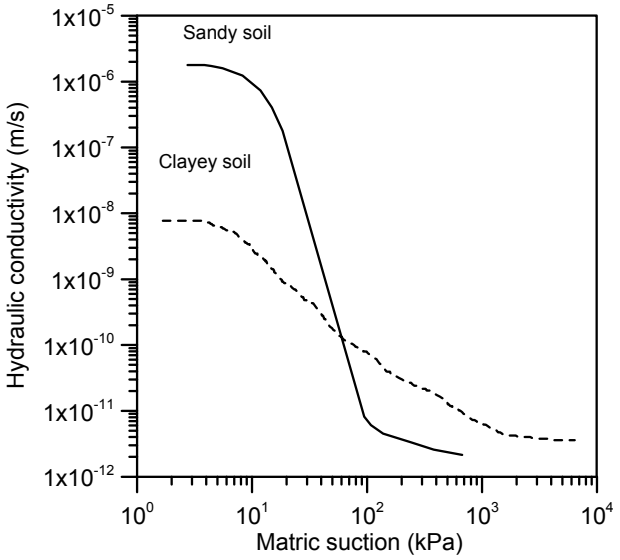

Figure 2-8: Relationship for water coefficient of permeability and matric suction for different types of soils (based on Hillel 1998).

Measurement of permeability in saturated soils

There are four laboratory methods generally used to measure the coefficient of permeability of saturated soils in the laboratory. These are known as: variable-head (falling-head) test, constant-head test, capillary method and back calculation from the consolidation test. The constant-head method is used in the case study of Chapter 6 to calculate the hydraulic conductivity of soils in saturated conditions. The procedure of the method is as follow (Figure 2-9):

1. The soil specimen is compacted to in-situ conditions and thereafter placed in the chamber on top of the base porous plate.
2. Calculate the height and area of the sample to calculate the volume of the sample.
3. Place the upper porous stone on the sample. The chamber cap is thereafter placed on top to close the chamber and some lubricant is used to seal the whole cell.
4. The constant-head reservoir is assembled and adjusted to the desired height above the outlet of the permeameter to create the desired head. Close the inlet valve to the permeameter. Fill the constant-head reservoir with de-aired water. De-air the lines connected to the inlet valve.
5. Open the outlet and inlet valves to saturate the sample and to remove the entrapped air in the soil (10-15 minutes).

6. When an equilibrium flow condition is established, place a graduated cylinder to receive the outflow and start a timer. When a sufficient quantity of water is obtained in the graduated cylinder, remove it and stop the timer. Record the quantity of water obtained and the time required obtaining it.
7. The saturated permeability of the soil is calculated by $k = \frac{\Delta V}{\Delta t} x \frac{h}{AxL}$ where ΔV is the volume of water in cm^3 calculated at time interval (Δt) in seconds, h is the head difference (cm), A is the area of the sample (cm^2), and L is the length of the sample in (cm). The permeability of the soil (k) is then calculated in cm/s.

Figure 2-9 shows a sketch of the apparatus used to calculate the saturated coefficient of permeability.

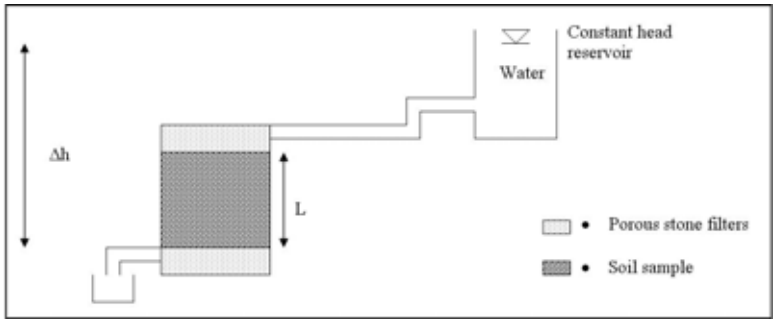

Figure 2-9: Sketch of the constant-head apparatus for permeability measurements.

Measurement of permeability in unsaturated soils

The water coefficient of permeability for unsaturated soils can be determined using either *direct* or *indirect* methods. The direct measurement method refers to permeability tests in the laboratory or in the field. Direct measurements of the water coefficient of permeability for an unsaturated soil are difficult to perform (Fredlund and Rahardjo 1993). However, indirect methods use the volume-mass properties of the soil and the soil-water characteristic curve as was defined in section 2.1.1. The saturated hydraulic conductivity of the soil is required in order to indirectly calculate the hydraulic conductivity function of the unsaturated soil. In the case study of Chapter 6, the hydraulic conductivity function of the soil is calculated indirectly by the author using the SWCC and the measured saturated hydraulic conductivity.

Many methods are proposed in the literature to describe the hydraulic conductivity function of a soil in the negative pressure range. The best known are the Fredlund and Xing (1994) method, the Green and Corey (1971) method and the Van Genuchten (1980) method. In the case study of Chapter 6, the closed form equation proposed by Van Genuchten (1980) is used. It is described by:

$$k_w = k_s \frac{\left[1-\left(a\psi^{(n-1)}\right)\left(1+\left(a\psi^{n}\right)^{-m}\right)\right]^2}{\left[\left((1+a\psi)^{n}\right)^{\frac{m}{2}}\right]} \qquad \textbf{Equation 2-8}$$

where:

k_s = saturated hydraulic conductivity,

a, n, m = curve fitting parameters,

n = 1/(1-*m*), and

ψ = required suction range.

The curve fitting parameters can be estimated graphically based on the SWCC like the one shown earlier in Figure 2-2. The slope of the function is calculated by:

$$S_p = \frac{1}{\theta_s - \theta_r}\left|\frac{d\theta_p}{d(\log\psi_p)}\right| \qquad \textbf{Equation 2-9}$$

where:

$\theta_{s,\,r}$ = the saturated and residual volumetric water content, respectively,

θ_p = the volumetric water content at the halfway point of the volumetric water content function, and

ψ_p = the matric suction at the halfway point of the volumetric water content function.

In order to estimate the parameters *m* and *a* from the SWCC and the calculation of S_p, Van Genuchten (1980) proposed the following formula:

$$m = 1-\exp(-0.8S_p) \qquad \text{for } 0 > S_p < 1; \qquad \textbf{Equation 2-10}$$

$$m = 1-\frac{0.5755}{S_p}+\frac{0.1}{S_p^{\,2}}+\frac{0.025}{S_p^{\,3}} \qquad \text{for } S_p > 1; \qquad \textbf{Equation 2-11}$$

$$a = \frac{1}{\psi}\left(2^{\frac{1}{m}}-1\right)^{(1-m)} \qquad \textbf{Equation 2-12}$$

2.2 Water Flow

In studying slope stability problems, it is essential to estimate the direction and quantity of flow together with the pore pressure magnitudes and distribution. The driving potential for flow of water in a soil is the hydraulic head gradient (H_w). This is equally true for saturated and unsaturated soils (Fredlund and Rahardjo 1993). The hydraulic head gradient is composed of both the elevation gradient (y) and the pressure gradient (μ_w / γ_w) (see Equation 2-13). The velocity gradient ($\upsilon^2{}_w / 2g$) is ignored in this equation because it most often is negligible in comparison to the elevation and pressure gradient.

$$H_w = y + \frac{\mu_w}{\gamma_w} \qquad \textbf{Equation 2-13}$$

where:
y = elevation of a given point above a defined datum, and
γ_w = unit weight of water.

The term seepage is used to describe a slow movement of water through a soil. Seepage analysis refers to the computation of the rate and direction of water flow and pore-water pressure distributions inside the flow regime. Seepage analyses can be conducted in a steady-state or transient manner. In steady-state conditions, there is no change in hydraulic head at any point with time while in transient conditions the hydraulic head changes as a function of time.

Water flow through unsaturated soils is governed by the same physics as for flow in saturated soils (i.e., Darcy's law). The difference lies in the calculation of the coefficient of permeability which is not a constant in unsaturated soils. Pore-water pressures generally have a negative gauge in unsaturated soil while it is positive in saturated soil (see Figure 2-10). This figure also presents how the negative pore-water profile changes due to surface flux (evaporation and/or infiltration). Figure 2-11 shows how the pore-water pressure gradient varies due to changes in surface flux in saturated and unsaturated soil. This gradient is important because it controls the form of the infiltration or wetting front. Left sloping gradients are referring to no-infiltration flux and no-evaporation while the right sloping

profiles are associated with increasing pore pressure gradients. This figure will be used to understand the mechanics of water flow through soils.

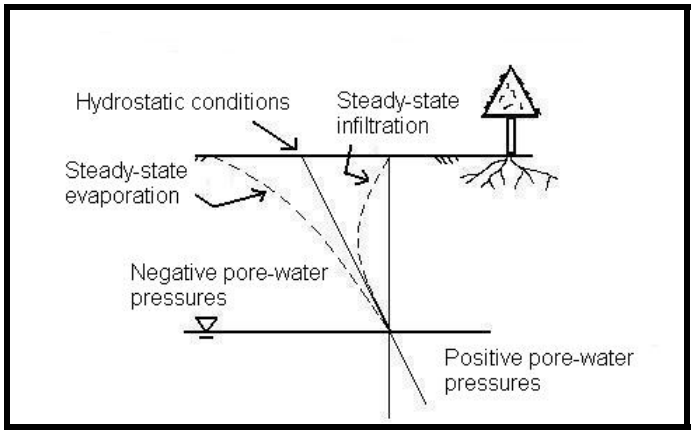

Figure 2-10: Typical pore-water pressures distribution in a soil (after Fredlund and Rahardjo 1993).

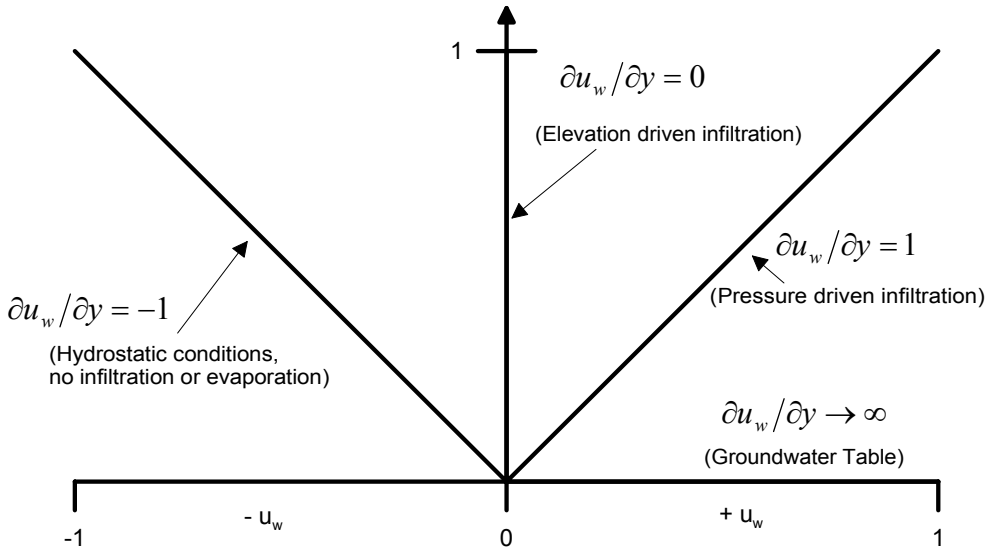

Figure 2-11: Effect of the pore-water pressure gradient on the infiltration in saturated and unsaturated regimes.

2.2.1 Partial differential flow equations

A two or three-dimensional equation for the flow of water is required when analysing slope problems. In many cases, water can be assumed to flow on the cross-sectional plane of the slope, and it is reasonable to assume that the flow perpendicular to that cross-sectional plane is small and negligible, i.e. two dimensional flow (2-D flow) The general governing equation for 2-D water flow in an unsaturated soil element may be represented by Richard's equation (1933):

$$\frac{\partial}{\partial x}\left(k_{wx}\frac{\partial H_w}{\partial x}\right)+\frac{\partial}{\partial y}\left(k_{wy}\frac{\partial H_w}{\partial y}\right)+Q=\frac{\partial \theta_w}{\partial t} \qquad \textbf{Equation 2-14}$$

where:

H_w = total head,

k_{wx} = hydraulic conductivity in the x-direction,

k_{wy} = hydraulic conductivity in the y-direction,

Q = applied boundary flux (infiltration, evaporation, etc.), and

t = time.

Equation 2-14 states that the computation of the rate of change of flow in the x- and y-directions plus an external boundary flux is equal to the rate of change of the volumetric water content with respect to time. This equation shows that the pore pressures in a transient infiltration system are governed by k_w, Q and a storage term ($\delta\theta/\delta t$). One must remember that the hydraulic conductivity in the x- and y-directions, in the above equation, is function of the water content or the capillary pressure in the soil.

If the volume of water entering the element is equal to the volume leaving the element at all time, steady-state condition is reached, and Equation 2-14 reduces to Equation 2-15. The pore-water pressure response of a steady-state infiltration system is primarily a function of (k_w) and (Q).

$$\frac{\partial}{\partial x}\left(k_{wx}\frac{\partial H_w}{\partial x}\right)+\frac{\partial}{\partial y}\left(k_{wy}\frac{\partial H_w}{\partial y}\right)+Q=0 \qquad \textbf{Equation 2-15}$$

The stress-state of an unsaturated soil can be described by the two stress-state variables (σ_n - μ_a) and (μ_a – μ_w) (see Section 2.3). Lam et al. (1987) showed that for an isotropic unsaturated soil element, the constitutive equation for the water phase can be written as:

$$\partial\theta w = m_a \partial(\sigma_n - \mu_a) + m_w \partial(\mu_a - \mu_w) \qquad \textbf{Equation 2-16}$$

where m_a and m_w are coefficients of volume change which can be regarded as constants for a particular time step during a transient process. For a natural slope and transient seepage conditions, it can be assumed that the total stress (σ_n) and the pore-air pressure (μ_a) in the soil mass remain constant and do not affect the water content of a soil. Changes in water content consequently depends on the (μ_a – μ_w) stress-state variable. In this case, one also assumes that the retention curve or SWCC does not present any hysteresis. Since the pore-air pressure is remaining constant, the changes in water content can be directly related to changes in pore-water pressure by the following:

$$\partial\theta w = m_w \partial\mu_w \qquad \textbf{Equation 2-17}$$

Substituting Equation 2-13 into Equation 2-17 leads to:

$$\partial\theta w = m_w \gamma_w \partial(H - y) \qquad \textbf{Equation 2-18}$$

Equation 2-18 can now be included in Equation 2-14 and leads to the following expression:

$$\frac{\partial}{\partial x}\left(k_{wx}\frac{\partial H_w}{\partial x}\right) + \frac{\partial}{\partial y}\left(k_{wy}\frac{\partial H_w}{\partial y}\right) + Q = m_w \gamma_w \frac{\partial(H_w - y)}{\partial t} \qquad \textbf{Equation 2-19}$$

It can be assumed that the elevation (y) is constant at a given point in a natural slope. The derivative of the elevation with respect to time will then lead to the governing differential equation for water flow in saturated/unsaturated soils:

$$\frac{\partial}{\partial x}\left(k_{wx}\frac{\partial H_w}{\partial x}\right) + \frac{\partial}{\partial y}\left(k_{wy}\frac{\partial H_w}{\partial y}\right) + Q = m_w \gamma_w \frac{\partial(H_w)}{\partial t} \qquad \textbf{Equation 2-20}$$

This equation describes the 2-D fluid flow through an unsaturated/saturated, homogenous and isotropic soil element. It should be recognized that this equation is highly non-linear given that the hydraulic head and the hydraulic conductivity of the soil are non-linear functions of

the volumetric water content. Numerical methods are then necessary in order to calculate the changes in pore-water pressure distribution with time.

2.2.2 Factors influencing water flow in unsaturated soils

Ng and Shi (1998) and Ng et al. (2001) performed numerical analyses showing the effects of rain infiltration on pore-water pressures and hence on the stability of a given slope. Ng and Shi (1998) used a 2-D finite element mesh for the calculations, while 3-D analyses were conducted in the investigation made by Ng et al. (2001). They considered the intensity of rainfall, duration of rainfall, return period of major rainfall, antecedent rainfall, the saturated permeability (k_s) and its anisotropy and the vegetation cover in their analysis. Their study showed that the suction in the soil and the groundwater table are mainly governed by the ratio of the infiltration flux and the saturated permeability (i.e., q_b/k_s) as well as the initial and boundary conditions. Moreover, the larger the antecedent infiltration rate, the lower the initial negative pore-water pressure will be. From their results, Ng and Shi (1998) also concluded that for a given slope, there exists a critical saturated permeability that may result in the greatest loss of negative pore-water pressure and thus to a lower safety factor.

Tsaparas et al. (2002) also used numerical analyses to study the effect of rainfall intensity, rainfall antecedent, different type of initial conditions and different permeability coefficient on the pore-water pressures in unsaturated slopes. They came to the conclusion that there exists a close interaction between the mentioned parameters and the pore-pressure distributions when performing transient analysis. Their study showed that highly permeable soil slopes ($k_s>10^{-4}$ m/s) were unlikely to be influenced by small amounts of antecedent rainfall as opposed to soil slopes composed of moderately permeable material (10^{-5} m/s). They therefore highlighted the importance of properly choosing these parameters before making any transient simulation.

Cai and Ugai (2004) with similar types of simulations also showed that the stability of a slope is influenced by its initial volumetric water content and the hydraulic properties of the soil as well as the pattern of the water pressure rise due to infiltration. By comparing numerical results with statistical and observational results they concluded that finite element analysis was a good method to evaluate the stability of slopes under rainfall.

Zhang et al. (2004) performed numerical analyses showing that under steady state conditions, the most important factor affecting the matric suction near the ground surface of a slope is the

surface flux (q_b) expressed as a percentage of the saturated coefficient of permeability (k_s). They also found that under transient seepage conditions the pore-water pressure profile was dependent on the magnitude of the rainfall flux, the saturated coefficient of permeability, and the water storage function. In addition, they numerically showed that the long term matric suction does not necessarily disappear under steady state rainfall fluxes that are two or more orders of magnitude less than (k_s).

Zhan and Ng (2004), from a 1-D analytical study, came to the conclusion that the effects of the desaturation coefficient (α) and the saturated permeability (k_s) on the pore-water pressure response were much more significant than that of the water storage capacity of the soil (θ_s-θ_r). They mentioned that the relative sensitivity of (k_s) and (α) depends on the range of negative pore-water pressure within the soil. In fact, they showed that during infiltration in a dry soil (early stage of a rainfall), the pore-water pressures are primarily affected by (α). They are controlled by the saturated permeability when the negative pore-water pressures dissipate with the duration of the rainfall. Their analysis showed that for steady state infiltration, the pore-water pressure response is more governed by ($q\alpha/k_s$). However, for the transient infiltration process, the pore-water pressure response depends not only on ($q\alpha/k_s$), but also on (k_s/α). The larger this latter ratio, the faster the wetting front advances downwards. Finally, these authors together with Ng and Shi (1998) showed that antecedent rainfall could be much more important than the subsequent as it controls the initial pore-water pressures and the initial coefficient of permeability (k_w).

Rahardjo et al. (2001) and Collins et al. (2004) have shown from field observations that rainfall intensity and antecedent rainfall can very often be directly related to slope failures. However, as stated by Tsaparas et al. (2002), the relation between climatic conditions and slope failures varies with geographical settings due to differences in porosity and permeability of soils. Also from field observations, Tsaparas et al. (2003) showed that the total rainfall and the initial pore-water pressures within a slope were the controlling parameters for the changes in pore-water pressures during infiltration.

Furthermore, the effects of the hysteresis in the SWCC on unsaturated flows were studied by Tami et al. (2004). They showed, from both experimental and numerical studies, that the hysteretic behaviour significantly affected the steady-state matric suctions within the slope profile. This effect was less important on the volumetric water content profile of the slope.

They however conclude with the fact that the appropriate hydraulic properties of the soils (i.e. drying or wetting) should be used in accordance with the actual process the slope is experiencing (i.e. desorption process or adsorption process) even if the slope is under a given steady-state rainfall condition.

Even though much work has been done in recent years, the effects of hydraulic parameters and rainfall patterns on the stability of unsaturated slopes are still difficult to predict and are not fully understood. The reason for this may be: (1) high non-linearity and variability of hydraulic parameters involved in the transient unsaturated flow system, and spatial and temporal variations in the initial and boundary conditions of the system (Zhan et al. 2004).

A recapitulation of the many factors influencing the flow of water through unsaturated soil is presented in Table 2-2.

Table 2-2: Principal factors influencing seepage in unsaturated soil slope.

Initial conditions of the slope	Intensity of the rainfall
Amount of water infiltrating the soil	Rainfall patterns
Surface evaporation	Antecedent of the rainfall
Type of vegetation cover	Water retention characteristics
Rate at which infiltration occurs	Coefficient of permeability

2.3 Shear Strength Theory

The shear strength of a soil is an essential parameter for numerous types of stability analyses. In this thesis, it must be defined in order to make predictions of the stability of a natural slope. The two commonly performed shear strength tests for unsaturated soil are the direct shear test and the triaxial test. One should refer to Fredlund and Rahardjo 1993 for a detailed discussion of these test procedures for unsaturated soils.

2.3.1 Stress state variables

The shear strength can be related to the stress state of the soil. In a saturated soil, the stress-state variable is called the effective stress and is often represented by the following:

$$\sigma' = \sigma - u_w \qquad \textbf{Equation 2-21}$$

where:
σ' = the effective normal stress,
σ = total normal stress, and
μ_w = pore-water pressure.

The effective stress concept is the basis of saturated soil mechanics. The mechanical aspects of saturated soils are governed by this stress state variable. Changes in effective stress can modify the equilibrium condition of a saturated soil. Volume change and shear strength are in that sense controlled by the effective stress. The shear strength of a saturated soil is most often expressed using the Mohr-Coulomb failure criteria and the effective stress concept:

$$\tau_{ff} = c' + (\sigma_n - \mu_w)_f \tan\varphi' \qquad \textbf{Equation 2-22}$$

where:
τ_{ff} = shear stress on the failure plane at failure,
c' = effective apparent cohesion,
$(\sigma_n - \mu_w)_f$, = effective normal stress on the failure plane at failure, and
φ' = angle of internal friction of the soil.

2.3.2 Strength of unsaturated soil

Unlike saturated soils, the shear strength of unsaturated soils cannot be described by a single stress-state variable. Many authors have attempted to develop a strength concept for unsaturated soils. Fredlund et al. (1978) justified the need for two independent stress state variables known as the net normal stress (σ-μ_a) and the matric suction (μ_a-μ_w). They proposed that the shear strength of an unsaturated soil could be expressed as

$$\tau_{ff} = c' + (\sigma_n - \mu_a)_f \tan\varphi' + (\mu_a - \mu_w)_f \tan\varphi^b \qquad \textbf{Equation 2-23}$$

where:
$(\sigma_n$-$\mu_a)_f$ = net normal stress on the failure plane at failure,
$(\mu_a$-$\mu_w)_f$ = matric suction on the failure plane at failure, and
φ^b = angle indicating the increase in shear strength relative to the matric suction, $(\mu_a$-$\mu_w)_f$.

An unsaturated soil tends to give a shear strength larger than that of the same saturated soil. Equation 2-23 says that an unsaturated soil gets its strength from three components: cohesion, frictional strength and suction strength. The shear strength equation for an unsaturated soil exhibits a smooth transition to the shear strength equation for a saturated soil (Fredlund and Rahardjo 1993).

For an unsaturated soil, the parameter φ^b is determined experimentally, and is normally found to be somewhere between φ' and φ'/2 (Fredlund and Rahardjo 1993). This φ^b-angle describes the increase of shear strength due to an increase in matric suction, while the friction angle (φ') describes an increase in shear strength caused by an increase in net normal stress.

From Equation 2-23, when the soil approaches 100% saturation, the pore-water pressure term approaches the pore-air pressure term and the matric suction tends to zero. Equation 2-23 can then be reverted to Equation 2-22 for a saturated soil.

According to Fredlund et al. (1996) the shear strength of unsaturated soils can also be computed using the SWCC and the saturated shear strength parameters of the soil. The strength of an unsaturated soil can then be written as:

$$\tau_{ff} = c' + (\sigma_n - \mu_a)\tan\varphi' + (\mu_a - \mu_w)\Theta^{\kappa}\tan\varphi' \qquad \textbf{Equation 2-24}$$

where Θ is the normalized volumetric water content equal to $\left(\frac{\theta-\theta_r}{\theta_s-\theta_r}\right)$, and κ is a soil parameter dependent upon soil type. According to Fredlund et al. (1996) the κ parameter is close to the value of 1 in sandy soils and increases with the plasticity of a soil. This last equation clearly shows that $\varphi'=\varphi^b$ at matric suction lower than the air entry value. In addition, taking κ = 1, one can imagine a possible decrease in the shear strength of the soil in excess of a given suction value when the volumetric water content tends towards zero (see Figure 2-12).

For shallow landslides, the pore-air pressure can be assumed to remain atmospheric during rainfall precipitation/infiltration, and only the pore-water pressure is increased (Chen et al. 2004). Equation 2-24 can then be written as:

$$\tau_{ff} = c'+(\sigma_n)\tan\varphi'-(\mu_w)\Theta^{\kappa}\tan\varphi' \qquad \textbf{Equation 2-25}$$

As seen from Equations 2-23 to2-25 above, the reduction of suction or changes in the volumetric water content affect a significant component of the shear strength. This in turn influences the overall slope stability. It is therefore of importance to correctly estimate the relation between the volumetric water content of a soil and its related matric suction (i.e. the SWCC).

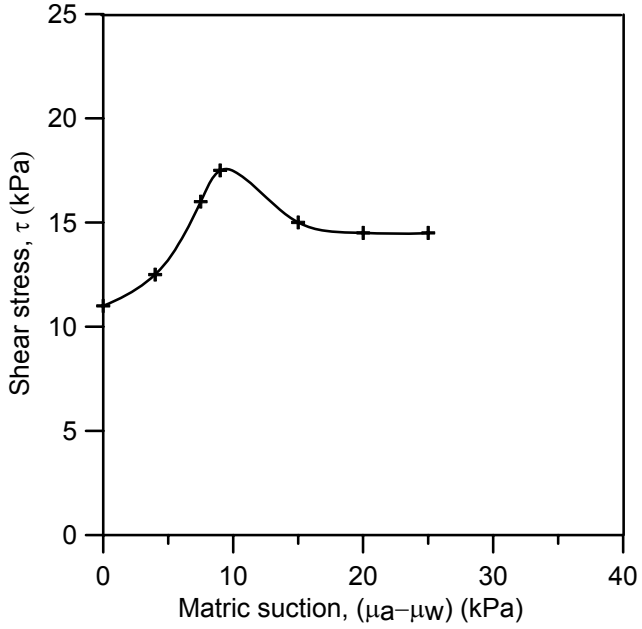

Figure 2-12: Results of direct shear tests on the medium Frankston sand under low matric suction (Donald 1956, from Fredlund et al. 1996).

CHAPTER 3 Parametric Study

Parametric studies of both seepage and slope stability analyses are presented in this chapter. The seepage analyses are conducted with SEEP/W 2-D finite element software (GEO-SLOPE, 1991-2004) version 5.19. This software is a 32 bit, graphical program which permits both simple and complex seepage analyses through saturated and unsaturated soils. The seepage analyses are used to investigate how the different hydraulic parameters, described in Chapter 2, are affecting the pore pressure distribution during and after rainfall events. The slope stability analyses are used to study the effects of these hydraulic parameters, on the safety factor of a given slope subjected to rainfall. For these stability analyses, the computer software SLOPE/W (GEO-SLOPE, 1991-2004) is used. SLOPE/W is a software which uses limit equilibrium theory to compute the safety factor of a slope.

This numerical study is divided into three parts. In the first part, the parameters which will be investigated are the saturated coefficient of permeability with respect to water (k_s), the effect of antecedent rainfall (q_a), the air-entry value parameter (*a),* and the desaturation coefficient (*n).* In this first series of simulations, the groundwater level is held constant. This helps illustrating the effect of the different parameters more clearly on the resultant pore-water pressures during rainfall events.

In natural conditions, the groundwater table may rise in a slope subjected to a prolonged rainfall. Therefore, the second type of seepage analysis implies a free groundwater level. In this series of simulation, the differences between pore pressure response in a fine and coarse grain soil are investigated. The effects of the geometry of the slope are also studied.

The effect of the air-entry value and of the φ^b parameter on the stability of a slope subjected to infiltration is studied in the third part. The differences in stability response of a fine and coarse soil are also investigated.

Presentation and discussion of the computed results for the different analyses are presented in Chapter 4 and discussed in Chapter 5.

3.1 Description of Seepage Analyses

3.1.1 Geometry and boundary conditions

The finite element mesh for the first series of simulations (i.e. constant groundwater level) is shown on Figure 3-1 together with the boundary conditions. The steady state and transient numerical analyses are performed on a 20 meter high slope inclined at 30°. In order to simplify the problem, it is assumed that the slope is composed of a homogenous, isotropic material. Along the left and right vertical boundaries, a zero flux was applied above the groundwater level. As mentioned previously, the groundwater table is fixed. This is done by applying a constant pressure head equal to zero along the segment CF in Figure 3-1. The groundwater table lies at 20m depth at the left side of the model while it is at 10m depth at the right side. It is also assumed that the horizontal base of the finite element mesh is impermeable. For the second type of simulations (i.e. free groundwater level) the finite element mesh and geometry are shown in Figure 3-2. The boundary conditions are also presented on this figure. The conditions along the left and right vertical boundaries in this case, are given as total head. A total head of 20 m of water is applied on the left AD boundary while it is set to 15 m on the right BC boundary. The horizontal base of the finite element mesh is also considered as being impermeable.

Rainfall infiltration is modelled as a moisture flux boundary, q_b (m/s), applied along the soil surface. In applying a top boundary condition to simulate the infiltration of rainfall, it is important to realize that an influx boundary condition greater than the saturated hydraulic conductivity, will lead to hydraulic gradients greater than unity and consequently positive pore pressure will develop at the surface (Collins and Znirdacic, 2004). As mentioned by these authors, positive pressure heads at the surface soil is analogous to having ponding of water. Since this ponded water would obviously run off the inclined slope in nature, the maximum water infiltration rate is given by a rainfall which maintains the pressure head at the slope surface equal to zero. For this, the maximum infiltration rate into the soil will be given by a boundary condition at the surface specifying a pressure head equal to zero (h_p=0). This type of boundary condition is thus representing a rainfall flux greater or equal to the saturated permeability of the soil with the non-infiltrating water taken as a runoff. On the other hand, for conditions where the infiltration flux is smaller than the saturated hydraulic conductivity, a flux boundary condition will be more appropriate to use.

Two major limitations are imposed when using the SEEP/W software for analysis of seepage through unsaturated soil. The first important limitation is assuming that the soil hysteresis between the wetting and drying process, as shown in the SWCC, is not significant. The second important limitation is that the soil is not subjected to any evaporation or evapotranspiration during the drying periods. However, since the purpose of this work is to study the changes in pore-water pressures during rainfall events, this last limitation should not affect the results and discussions.

3.1.2 Finite element mesh and numerical issues

Numerical instabilities in transient analyses are related to the non-linearity of the water flow equation through unsaturated soil (Equation 2-20) and to the steep water content and conductivity functions. The meshes presented in Figure 3-1 and Figure 3-2 are designed to prevail over convergence problems regarding transient seepage solutions. The areas of instabilities are found to be along the surface slope where the pore-water pressure changes rapidly during the rainfall. To overcome these convergence problems, mesh refinement was required along the slope surface. However, this fine mesh cannot be used over the entire problem geometry because it would take too much computer time. The presented finite element meshes were found to give stable and acceptable results in addition to permit solving the transient problems in a reasonable time.

As mentioned, the solutions to unsaturated seepage problems can be highly non-linear due to the variability in conductivity and in the rate at which water is released or retained during a transient process. The degree of non-linearity is dependent on the steepness of the conductivity function and the SWCC. Difficulties with convergence can be encountered when either of these material property functions becomes relatively steep. In order to obtain a satisfactory solution, the convergence parameters were tested to find the best combination prior to doing any simulations.

To solve the seepage equation, the direct equation solver is selected. The tolerance of computed norm of the head vectors is set to 0.001% between two consecutive iterations. The software continues the iteration procedure until this constraint is met. The maximum change in hydraulic conductivity between iterations is set to 1 order of magnitude while the minimum change is set to 10^{-3} orders of magnitude. For each simulation case, the oscillation of the iteration procedure was checked and found to be stable. The maximum number of iteration

was set to 200, but rarely the software required more than 20 to fully converge. The average number of iterations needed by the software to converge was 6. In addition to these convergence parameters, an adaptive time stepping routine was used in the iteration process. This routine inserts extra time steps between the user's specified time steps so that the head value changes are less than the user-specified percentage. The minimum applied increment size was set to 0.01 seconds. To monitor the allowable change in nodal heads, the individual nodal head comparison was chosen. The effects of these convergence parameters are discussed later in Chapter 4.

3.1.3 Phases of analysis

Each analysis is divided into two phases. The first phase consists of achieving steady state conditions in the slope. At the end of this stage, the initial conditions, as seen on Figure 3-1 and Figure 3-2, are reached. In the normal initial condition case, it is assumed that the antecedent rainfall flux is null (q_a=0m/s). This leads to an initial hydrostatic suction distribution within the slope. This is a reasonable estimate of in-situ conditions prior to rainfall in many cases (Collins and Znidarcic, 2004). In the second phase of the simulation, a transient analysis is used to simulate water infiltration in the slope. The infiltration flux is constant during the whole simulation time. During this stage, the pore pressure distribution within the soil slope can be studied at any time step during the infiltration process.

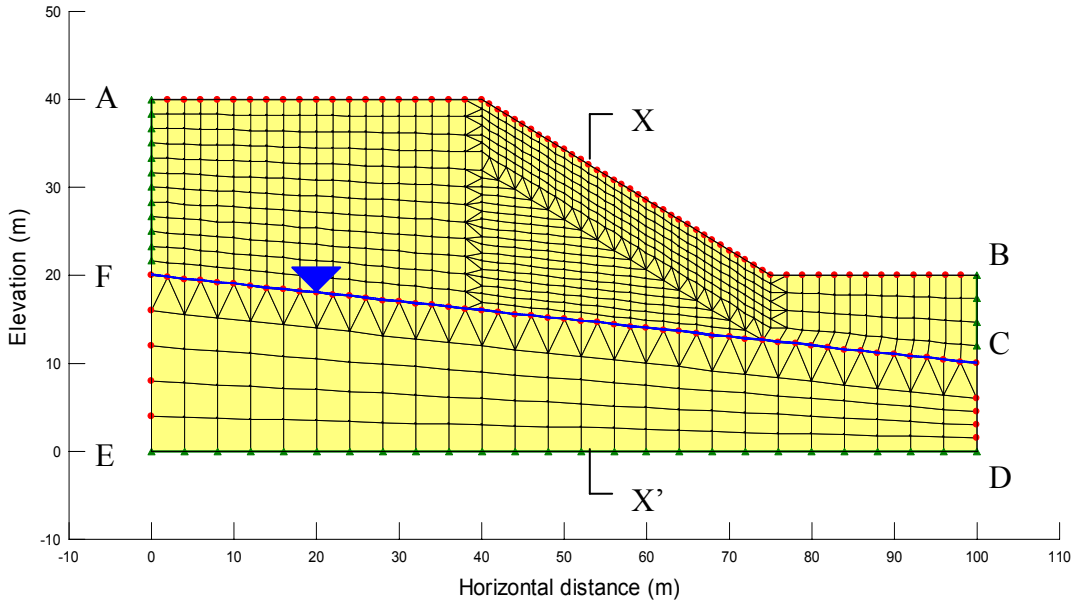

Figure 3-1: Geometry of the finite element mesh used for simulations under constant groundwater level.

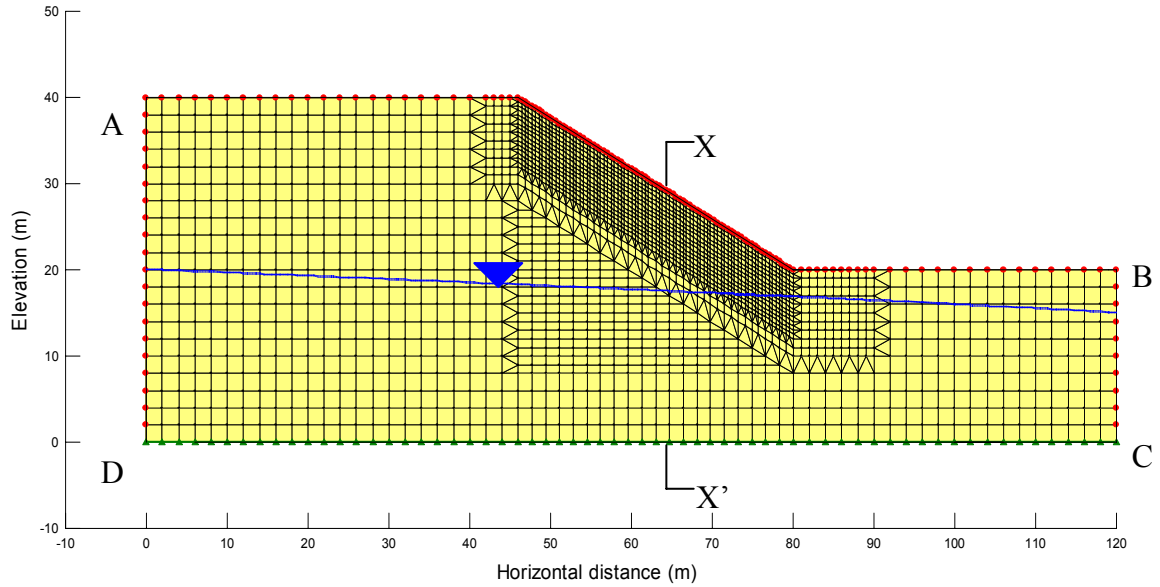

Figure 3-2: Geometry of the finite element mesh used for simulations under free groundwater level.

3.2 Variables in the Seepage Analysis

3.2.1 Constant groundwater level analysis

The first type of simulation assumes that the groundwater level is not affected by the rainfall. A total of 5 different studies are performed. The variable parameters in the analysis are the ratio of the infiltration flux to saturated coefficient of permeability (q_b/k_s), the saturated coefficient of permeability (k_s), the air-entry parameter (a), the desaturation coefficient (n) and the antecedent rainfall (q_a). Antecedent rainfalls are studied under both the steady-state and transient analyses. A description of the different study cases is given in Table 3-1.

The permeability functions used in the different study cases are presented in Figure 3-3. This figure presents the effect of the air-entry value (a) and the desaturation coefficient (n) on the permeability functions in the negative pressure range. In this figure, the saturated coefficient of permeability is set to $1x10^{-5}$m/s.

Table 3-1: Description of the different analyses assuming that the groundwater table is held constant.

Case	Study of	a	m	n	k_s (m/s)	q_a (m/s)	q_b (m/s)
1	q_b/k_s	10-200	1	2	$1x10^{-5}$	0	$1x10^{-5}$ $1x10^{-6}$ $1x10^{-7}$
2	Effect of k_s	10 50	1	2	$1x10^{-4}$ $5x10^{-5}$ $1x10^{-5}$ $1x10^{-6}$	0	$1x10^{-4}$ $5x10^{-5}$ $1x10^{-5}$ $1x10^{-6}$
3	Effect of "*a*"	1-100	1	2	$1x10^{-5}$	0	$1x10^{-5}$
4	Effect of "*n*"	10	1	1-3	$1x10^{-5}$	0	$1x10^{-5}$
5	Effect of q_a	1-100	1	2	$1x10^{-5}$	$1x10^{-6}$ $1x10^{-7}$ 0	$1x10^{-5}$

where: a = air-entry value; n = desaturation coefficient; m = residual desaturation coefficient; k_s = saturated coefficient of permeability; q_a = antecedent rainfall; q_b = rainfall event.

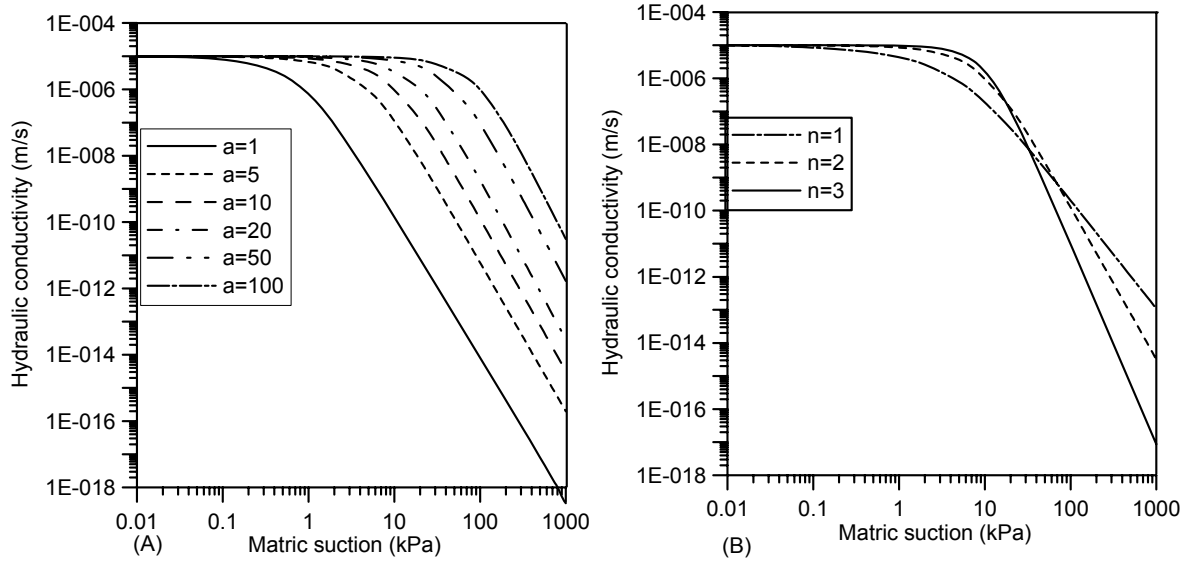

Figure 3-3: Hydraulic conductivity functions for soils with changing (A) air-entry values (n=2 and m=1) and (B) desaturation coefficient (a=10 and m=1).

3.2.2 Free groundwater level analysis

In the analyses where the groundwater level is not constant, the simulations are varying the type of soil. The study is carried out for a slope composed of a fine grain soil and for a coarse grain soil. Both slopes have an angle of 30 degrees, and the finite element mesh for these soil slopes is presented Figure 3-2. The soil-water characteristic curves and conductivity functions for the fine and coarse grain soils are presented in Figure 3-4 A and B respectively.

The saturated permeability of the coarse soil is $5x10^{-4}$m/s while a value of $1x10^{-5}$m/s is specified for the fine grain soil. There is then a saturated permeability difference of 50 times between both soils. In the SWCC, the air-entry value and the saturated volumetric water content are greater for the fine soil. The desaturation coefficient is steeper for the coarse grain soil. It can be seen that the permeability functions are crossing at a suction value of 10 kPa. For a higher suction value than this, the permeability of the coarse soil is smaller than for the fine soil.

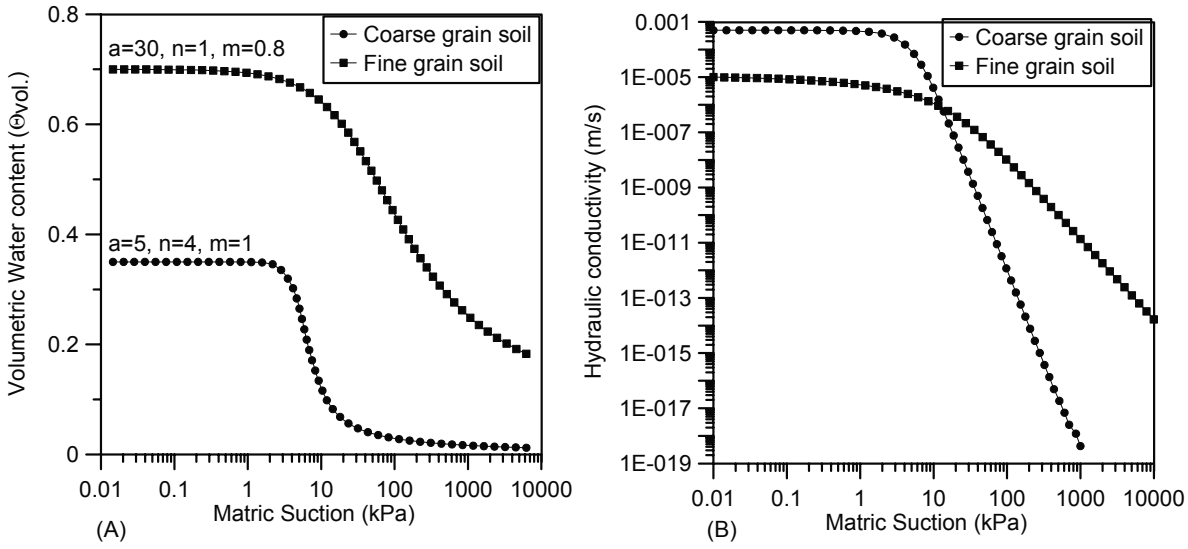

Figure 3-4: (A) SWCC for a coarse and fine grain soil. (B) Hydraulic conductivity functions for the corresponding coarse and fine grain soil.

3.3 Description of Slope Stability Analysis

Slope stability analyses are performed with the SLOPE/W software (GEO-SLOPE, 1991-2004). This uses limit equilibrium theory to compute the safety factor for a given slope. For the stability analysis, the simplified Bishop's method of slices satisfying moment equilibrium is used. The pore-water pressures determined at given time steps in the seepage analysis are incorporated in SLOPE/W as input conditions. The slip surfaces are prescribed in the model. They are presented on Figure 3-5. The first slip surface is shallow (2.5m), while the second as a deeper failure surface (6m). The third slip surface is focusing on instabilities at the toe of the slope (6m deep).

The stability analyses in this work are mainly focusing on the effect of the φ^b-angle and the hydraulic parameters of a soil. The stability analyses are carried out for the fine and coarse grain soil. The unit weight of these two is set constant to 19 kN/m^3. It is assumed that cohesion does not contribute to the shear strength of the soils (c'=0 kPa). The effective friction angle (φ') for both soils is set to 30°.

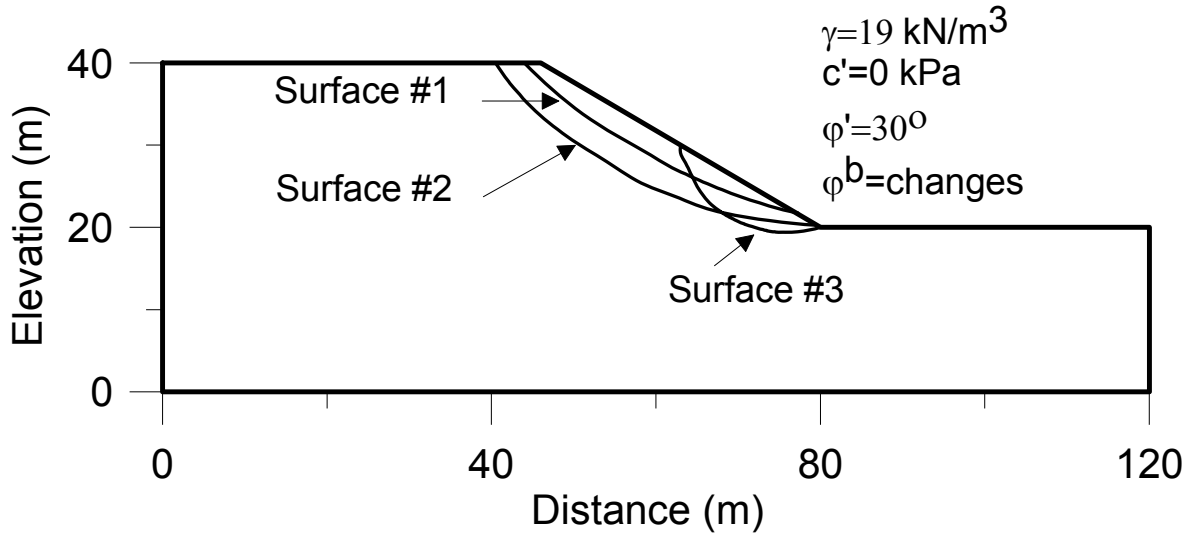

Figure 3-5: Different slip surfaces defined on the 30 degree slope model for stability calculations.

CHAPTER 4 Results of Analyses

4.1 Simulations under constant groundwater level

The results presented in this section are taken at cross section X-X' in Figure 3-1.

4.1.1 Case 1: Effect of the q_b/k_s ratio

The simulations are performed with a constant coefficient of permeability (k_s=1x10^{-5} m/s) while the infiltration flux varied (i.e. q_b=10^{-5}-10^{-7} m/s). Figure 4-1 shows the effect of the q_b/k_s on the pore-water pressure magnitude and distribution. This effect is given for different air-entry value parameters (a=10-200).

As illustrated by the results, the greatest loss of suction arises when the ratio q_b/k_s tends to a value of one, and the rate of matric suction loss increases with the air-entry parameter. In fact, with q_b/k_s=1 it took 6 days to lose matric suction when a=10, while it only took 10 hours when a=200. Finally, it can be seen that the effect of q_b/k_s is more important when the air-entry value parameter increases.

4.1.2 Case 2: Effect of the saturated coefficient of permeability

In these simulations, the ratio q_b/k_s is assumed to be equal to one. At the same time, the value of k_s varies between 1x10^{-4} and 1x10^{-6}m/s. The simulations are performed for both an air-entry value parameter of 10 and 50. The results are presented in Figure 4-2.

It can be observed that the coefficient of permeability affects the pore-water pressures even if the q_b/k_s ratio stays equal to 1 during transient analysis. For both cases, the greater the magnitude of k_s, the deeper the wetting front is in the middle of the slope. In addition, it takes more time to dissipate the negative pore-water pressures when the saturated coefficient of permeability is smaller. The shapes of the wetting fronts are similar, but the rates of downward movement are specific for each air-entry value coefficient since the latter controls the permeability of the soil. Therefore, the behaviour of rainfall infiltration under transient seepage conditions should be related to the absolute intensity of the rainfall and the soil properties (Zhang et al. 2004).

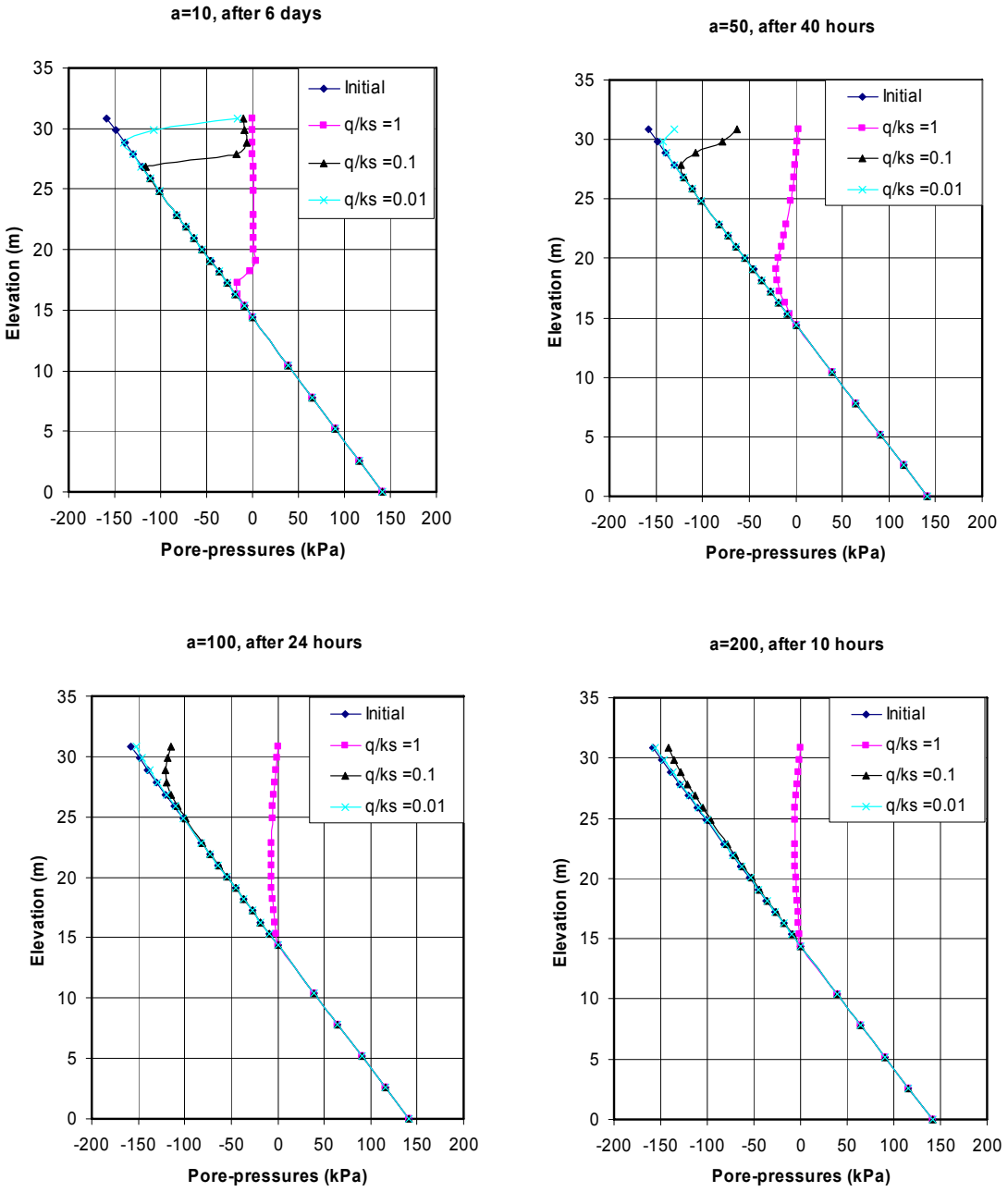

Figure 4-1: Effect of the q/k_s on the pore-water pressure distributions of soils with different air-entry value parameter "a". The profiles are taken at the middle of the slope.

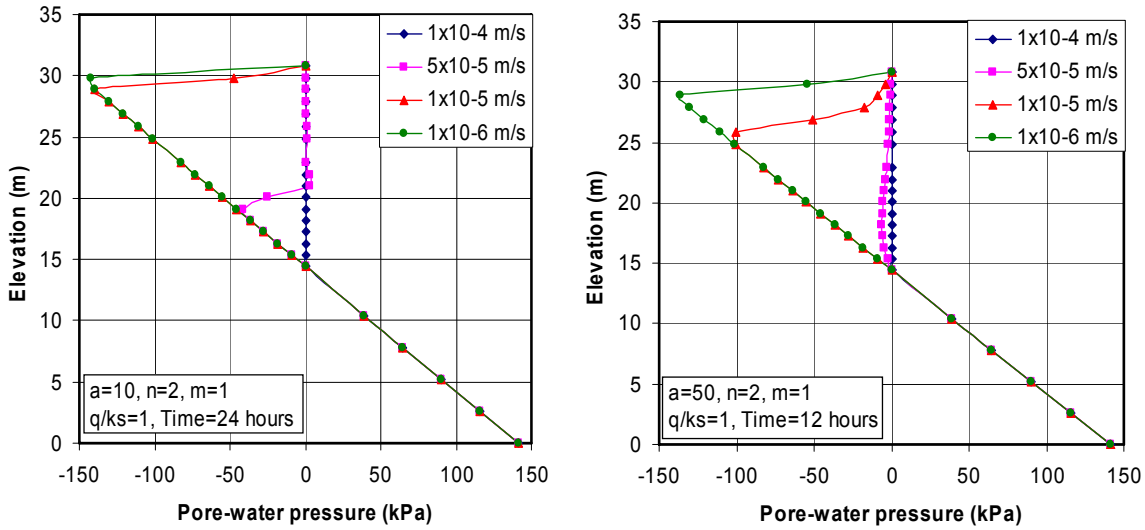

Figure 4-2: Influence of the saturated coefficient of permeability on pore-water pressures for different air-entry values. The profiles are taken at the middle of the slope.

4.1.3 Case 3: Effect of the air-entry value

In this third case, importance is given to the air-entry parameter. Its effect is studied given that the ratio $q_b/k_s=1$ and the value of k_s is constant throughout the simulations at a value of $1x10^{-5}$ m/s.

Figure 4-3 A and B are presenting the evolution of pore-water pressures with time for soils having air-entry values of 10 and 100 respectively. It is possible to observe the different positions of the wetting front with time. The soil having an air-entry value of 10 loses its matric suction after approximately 6 days of constant infiltration. For the soil having air-entry value of 100, this time is approximately one day. The soil with the low air-entry value presents a much more distinct infiltration front than the soil with a=100.

Figure 4-4 shows some results when a soil-slope with different air-entry values (1-100) is subjected to a constant infiltration during a period of 24 hours. As illustrated by this figure, the higher the value of "*a*", the faster the loss of matric suction. Another interesting observation is that the transition between the infiltration zone and the unaffected zone is distinct for air-entry values smaller than 30. Below the infiltration front, the suction profile remains essentially constant. This fact was also observed by (Zhang et al. 2004).

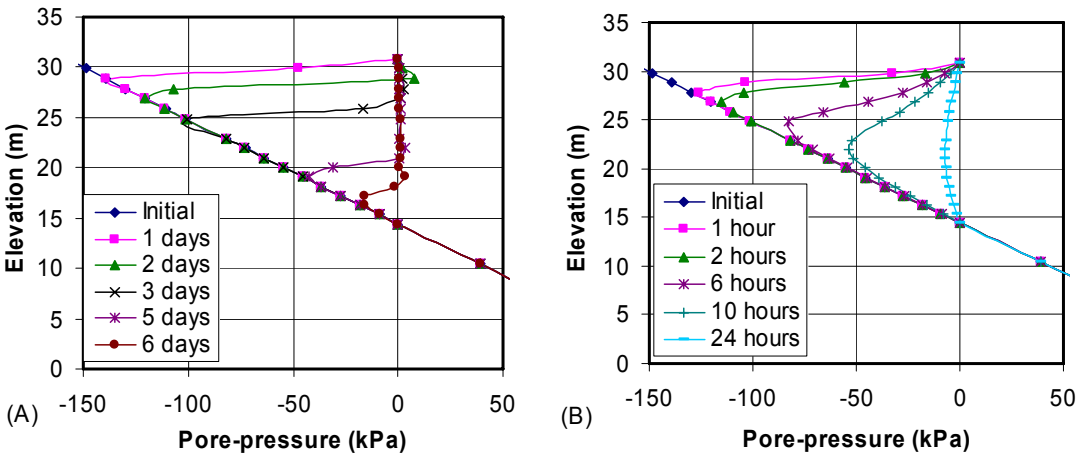

Figure 4-3: Pore-water pressure distribution with time for air-entry values of (A) 10 and (B) 100. The profiles are taken at the middle of the slope.

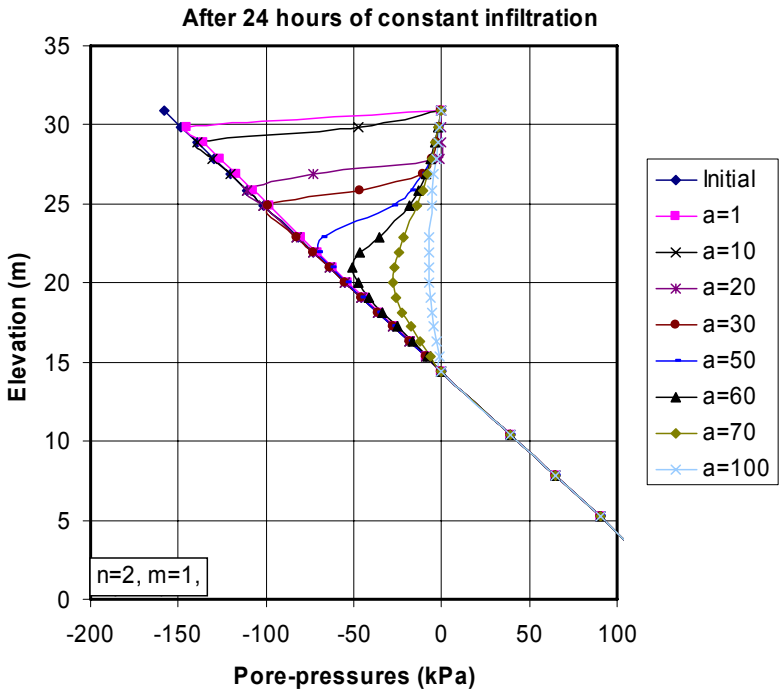

Figure 4-4: Effect of the air entry value on the pore-water pressure distribution after 24 hours of constant infiltration. The profiles are taken at the middle of the slope.

4.1.4 Case 4: Effect of the desaturation coefficient n.

As shown in Figure 3-3 B, the coefficient of hydraulic conductivity of a soil is affected by its desaturation coefficient "*n*". At low suction values, the soil with lowest "*n*" value (assuming constant values of a, m, θ_s and k_s) presents the lowest hydraulic conductivity. However, at higher suction values the soil with highest desaturation rate presents the lowest hydraulic conductivity. This fact is important since it controls the seepage pattern through the unsaturated soil as observed in this section.

Figure 4-5 presents the results of pore pressure distribution when varying the value of the desaturation coefficient for a given soil. The profiles are taken in the middle section of the slope after 1 day (A) and 4 days (B) of constant infiltration ($q_b=k_s$). On both profiles, the initial pore-water pressures prior to rainfall are presented. After 4 days, the soil with the desaturation coefficient *n*=3 presents the deepest infiltration front. However after a shorter infiltration period (1 day), soils with *n*=2 and *n*=3 present nearly the same infiltration depth. The soil with the desaturation coefficient *n*=1 presents the shallowest infiltration front.

These differences in the pore-water pressures at different times (1 and 4 days) can be explained by the following: Initially, the soil with the greatest desaturation coefficient will present the lowest coefficient of permeability. This is true, given that the initial matric suction at the top of the profile is nearly 160 kPa. During the first moments of transient infiltration, the infiltration rate for the soil showing the lowest "*n*" will be greater. However, as the suction disappears, the infiltration front for the soil with the highest "*n*" value will move faster due to its coefficient of permeability. As a result of this, the pore-water pressure profiles can present the same trend at a given time but thereafter be different.

Figure 4-5 A and B are showing that the initial matric suction profile, and hence the initial volumetric water content of the soil, affects the pore-pressure distribution in addition to the desaturation coefficient.

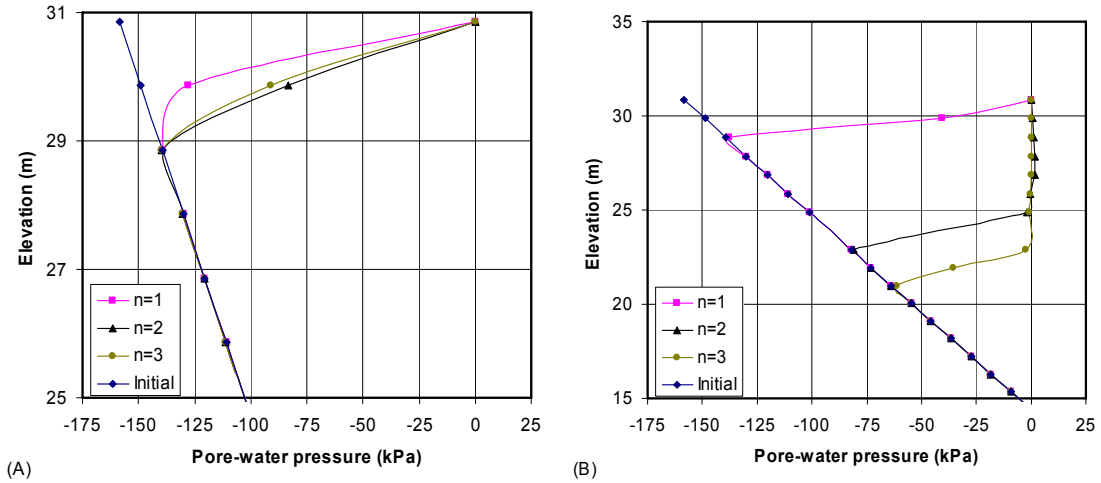

Figure 4-5: Effect of the desaturation rate parameter "n" on the pore-pressure distribution under transient seepage with $q/k_s=1$ after (A) 1 day and (B) 4 days.

4.1.5 Case 5: Effect of the antecedent infiltration

Up to now, the rainfall simulation on the model slope took into account that the initial suction profile was hydrostatic. This will not be so if a period of rain preceded the extreme rainfall. The suction profile in a slope is a function of the soil type and the net infiltration rate, which is itself a function of rainfall, evaporation and transpiration. The profile may also be affected by upwards seepage from suction caused by vegetative cover. The present case helps understanding the effect of antecedent rainfall and soil type on the pore-pressure distribution profile of a slope.

A steady-state analysis is firstly realized to show how the soil properties are influencing the initial pore-pressure distributions on a long term basis. In this case, the rate of antecedent rainfall is one order of magnitude smaller than the soil saturated permeability (i.e. $q_a/k_s=0.1$).

The results in Figure 4-6 A are showing how the air-entry value controls the pore-water pressures in the soil for steady-state antecedent rainfall. Once again, a higher air-entry value leads to higher matric suction.

The suction profiles shown in Figure 4-6 consist of a section of constant suction, a transition section and a section of hydrostatic condition. This fact was also shown by Zhang et al. (2004) in their analysis. They also showed that the matric suction in a given soil-slope will only be eliminated if the infiltration rate is higher or equal to the saturated coefficient of

permeability. In the present case, one can observe that the suction is not completely disappearing because $q_a<k_s$.

It was shown in Equation 2-15 that for steady-state conditions, the pore-water pressure responses is a function of q/k_s. The matric suction values at the top of the soil in Figure 4-6 A can thus be verified by looking at the permeability function. This is done by associating the steady state rainfall flux q_a to its given matric suction (see Figure 4-6 B). This observation shows that the soil properties, in addition to the ratio q_a/k_s, are controlling the steady-state pore pressure distribution for a given soil slope.

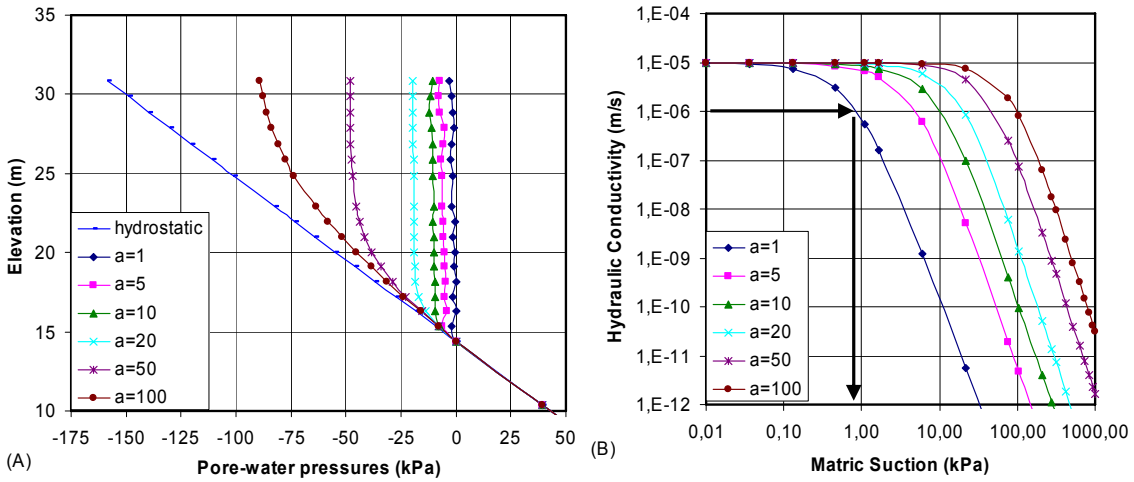

Figure 4-6: A) Steady-state pore-water pressure distributions for soils with different air-entry values and an infiltration rate equal to q_a=1e-06 m/s. B) Determination of the matric suction for a soil subjected to a steady state rainfall.

The previous steady-state analysis showed that antecedent rainfall leads to various pore pressure distributions in a slope. These steady-state conditions are now taken as initial conditions prior to a major rainfall. In order to show the effect of q_a on the transient pore pressure distributions, different magnitudes of antecedent rainfall (q_a=0, 10^{-6}, 10^{-7} m/s) are simulated on the 30 degree slope. After achieving steady state conditions, the model is subjected to a rainfall of intensity ($q_b=k_s=1x10^{-5}$m/s). The initial suction profile results are shown in Figure 4-7 together with the profiles after 10 hours of constant infiltration.

As the antecedent rainfall increases in magnitude, the soil tends to lower the initial matric suction. After the transient rainfall, the lowest matric suction profiles are found for soil-slopes

which were previously subjected to the greatest antecedent rainfall. Moreover, the soil-slopes which had lost less suction due to lower antecedent rainfall are presenting the greatest matric suction loss during the transient rainfall.

With these results, it is possible to observe that different antecedent rainfall are leading to different pore-water pressure distributions for soil-slopes subjected to the same transient rainfall. The depth of the infiltration front is controlled by the antecedent rainfall flux. For a greater antecedent rainfall, a deeper infiltration front will be observed.

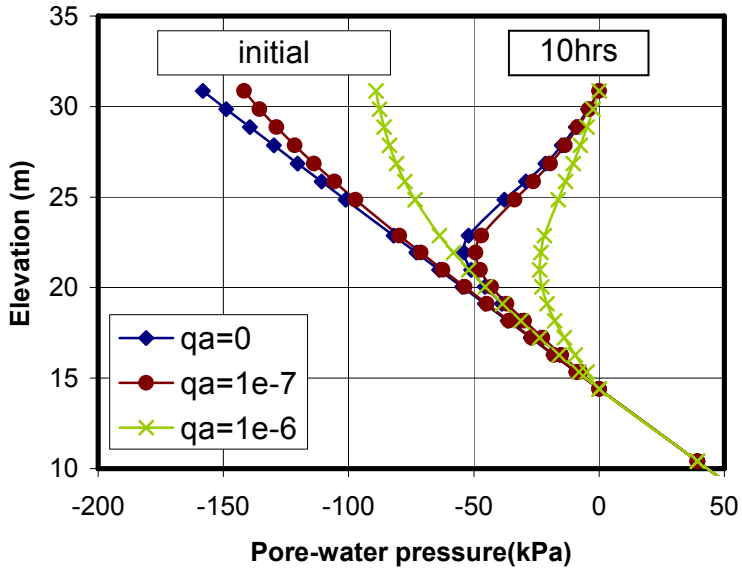

Figure 4-7: Effect of antecedent rainfall on the pore-water distribution on a soil subjected to an extreme rain event with $q_b=k_s=1x10^{-5}$ m/s (rainfall time = 10 hrs, air-entry value = 100).

4.2 Simulations with free groundwater table

4.2.1 Fine soil vs. coarse soil

Numerical simulations are carried out to show the difference in the pore pressure response between a fine and coarse grain soil subjected to rainfall. Collins and Znidarcic (2004) showed, with the help of numerical simulations for an infinite slope model, that the differences in hydraulic characteristics of the soil could lead to different flow pattern. Their results are showing that positive water pressure could develop in coarse soils above the infiltration front due to their hydraulic characteristics. As they mentioned, this is analogous to the establishment of a perched water table in the upper part of the soil layer. In contrast, they explain that since a fine grain soil conducts water more freely through its channel network, the resistance to flow is minimized and pore-pressure in excess of steady-state do not arise. Positive pore pressures behind the wetting front were also observed by Tsaparas et al. (2002) by numerical flow simulation. However they did not discuss these results.

Major hydraulic differences are to be found between a fine and coarse soil, the first one being the saturated coefficient of permeability (see Figure 3-4). Coarse soils are normally showing a k_s value which is orders of magnitude greater than for a fine soil. The air-entry value for a fine soil is generally greater than for a coarse soil. The desaturation coefficient is usually smaller for a fine soil. Since a fine soil can retain more water within its pores, its saturated water content is generally higher.

Infiltration analyses are carried out on the finite element mesh and slope geometry presented in Figure 3-2. The analyses are made with the coarse and fine grain soil presented in Figure 3-4. Pore pressure profiles are taken in the middle of the slope during the transient process and are presented in Figure 4-8.

Due to rainfall infiltration, both soils are showing a loss of matric suction with time. As illustrated in these results, the infiltration takes place much faster into the coarse grain material. This is a result of the higher saturated hydraulic conductivity of the coarse grain soil. However, for a short infiltration time and at initially high matric suction in the soil, a fine grain soil would conduct water more rapidly through its pores, and infiltration would take place faster than in a coarse grain soil.

The profiles for the fine grain soil are shown at intervals of 0.5 day while the intervals are 0.25 hour for the coarser soil. It can be observed that infiltration occurs at the same rate in the fine soil since the distance between the infiltration fronts is constant. On the other hand, the infiltration rate is initially low and then increases to reach a constant rate in the coarse soil.

The wetting fronts for the coarse soil are very distinct and more horizontal than those for the fine soil. This difference would be even clearer if a greater air-entry value was used in defining the fine soil hydraulic functions (see analyses in Section 4.1.3).

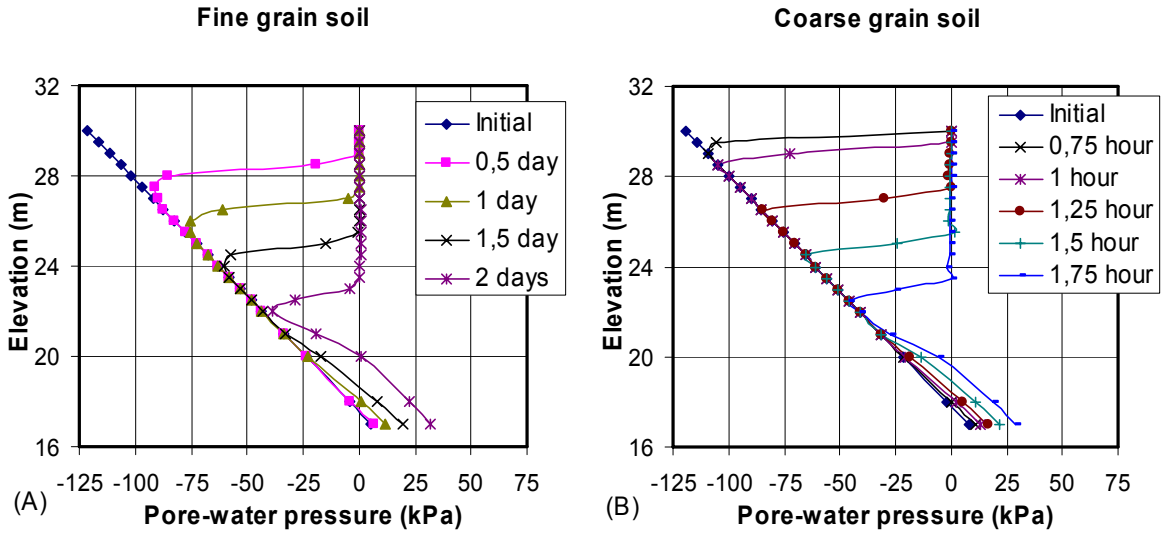

Figure 4-8: Pore-water pressure profiles taken at cross-section X-X' during the infiltration for (A) a fine grain soil and (B) a coarse grain soil.

Figure 4-9 compares the loss of matric suction with time at different locations along the slope for the two soils. The results are shown at a depth of 2m at location: 10m in back of slope, top, middle, toe and 10m in front of the slope. Figure 4-9 A shows the pore-pressure decrease in time for a coarse soil while B is for a fine grain soil. It can be observed that the soils are responding in a very different manner to the infiltration. For the coarse grain soil, the matric suction disappears very fast at the toe and in front of the slope in comparison to the top of the slope. After less than 0.5 hour, positive pore pressures develop at the toe of the slope. In contrast, no suction is lost at the top of the slope after more than 2.5 hours. For the fine soil slope, positive pore pressure also develops first at and in front of the slope. The reduction of matric suction at the toe and in the middle of the slope presents the same pattern as for the

coarse soil considering the difference in time scale. However, the slope composed of fine soil presents a reduction in matric suction at the top of the slope at the same time as positive pore-water pressure develops at the toe of the slope. In comparison with the fine soil, it is more difficult for the coarse material to lose suction at higher locations in the slope.

Flow velocity (υ_w) in a soil is defined in Equation 2-7 as the hydraulic gradient times the coefficient of permeability of the soil. Flow velocity profiles for the coarse and fine soil slopes are presented in Figure 4-10 A and B, respectively. Again, these profiles are taken at 2m under the soil surface at various locations along the slope. The flow velocities in the coarse soil model differ greatly from toe to top in the slope. The velocity is much larger at the bottom of the slope. The flow velocity in the fine soil is also initially higher at the bottom of the slope. However, after less than one day, the velocity at the middle and top of the slope gets higher than at the bottom.

Flow nets are presented for the coarse and fine grain soils in Figure 4-11 and Figure 4-12, respectively. It is possible to observe major differences in the infiltration pattern for the two soil types. In the coarse soil, the zero pressure contour moves from the toe to the top of the slope. The zero pressure contour is a little diffuse along the slope. This is due to the steep permeability function and consequently highly non-linear seepage solution.

In the fine grain soil, the zero pressure contour moves from the toe and upwards, but also inside the slope. This explains the differences observed in the pore-water pressure response and the results for flow velocities. The infiltration in the fine material is fairly constant along the slope while it moves gradually upwards in the coarse type soil.

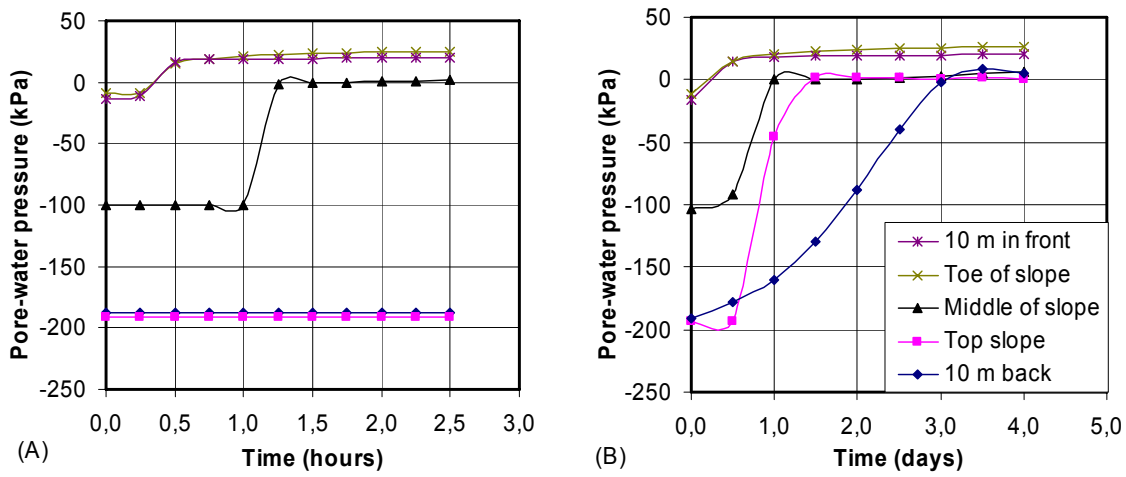

Figure 4-9: Pore-water pressure versus time taken at different emplacement at 2m depth along the model for (A) coarse and (B) fine grain soil.

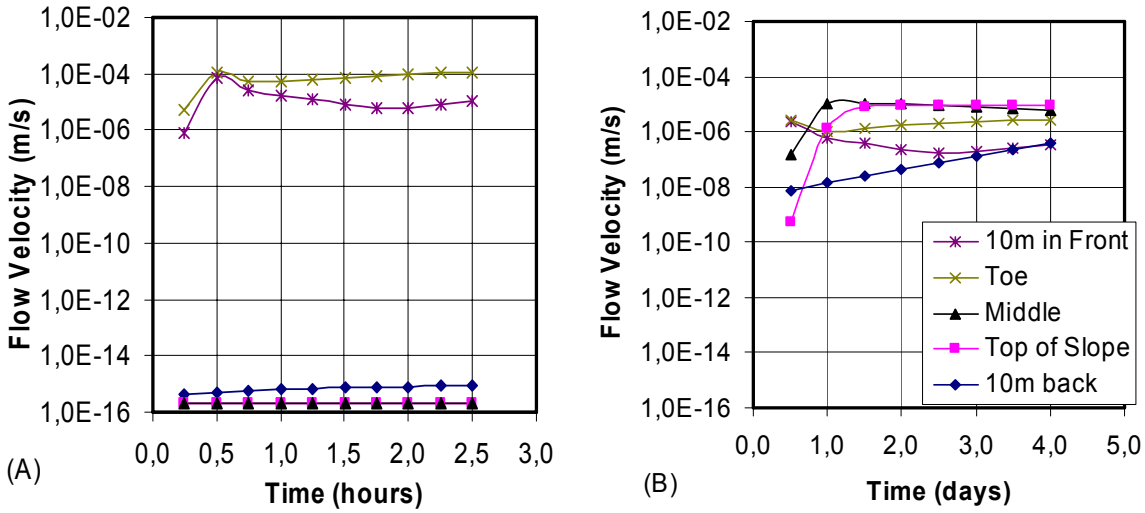

Figure 4-10: Flow velocity versus time taken at different emplacement at 2m depth along the model for (A) a coarse and (B) a fine soil grain soil.

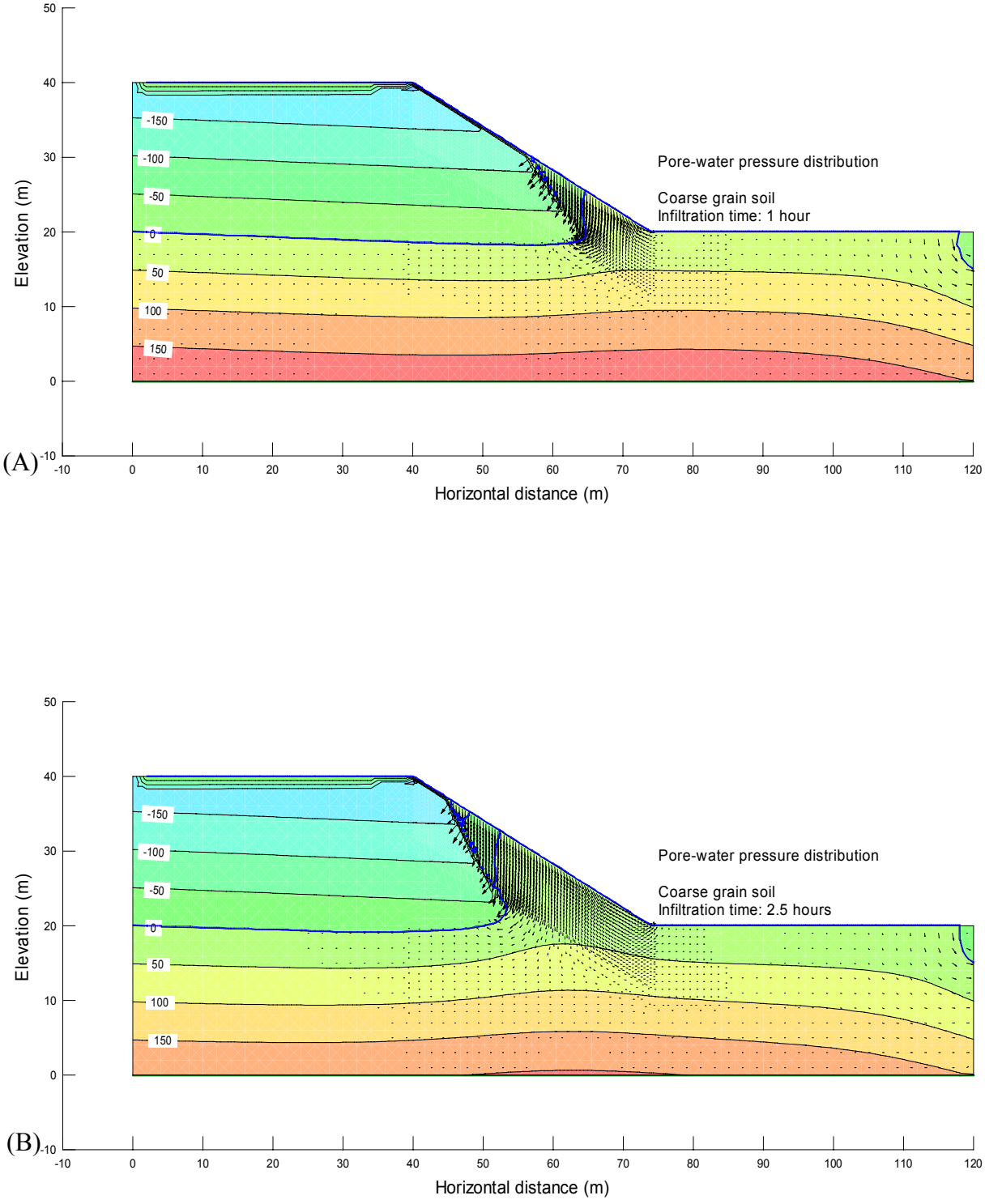

Figure 4-11: Flow net showing pore-water pressure (kPa) during the infiltration process for a coarse soil after (A) 1 hour and (B) 2.5 hours of infiltration.

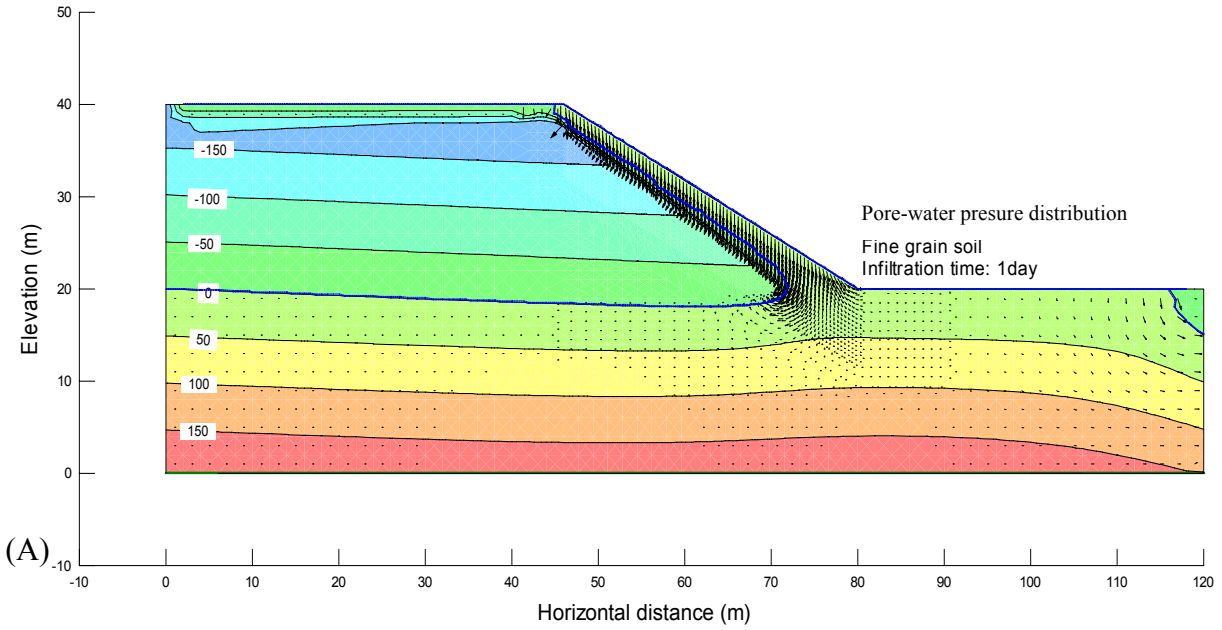

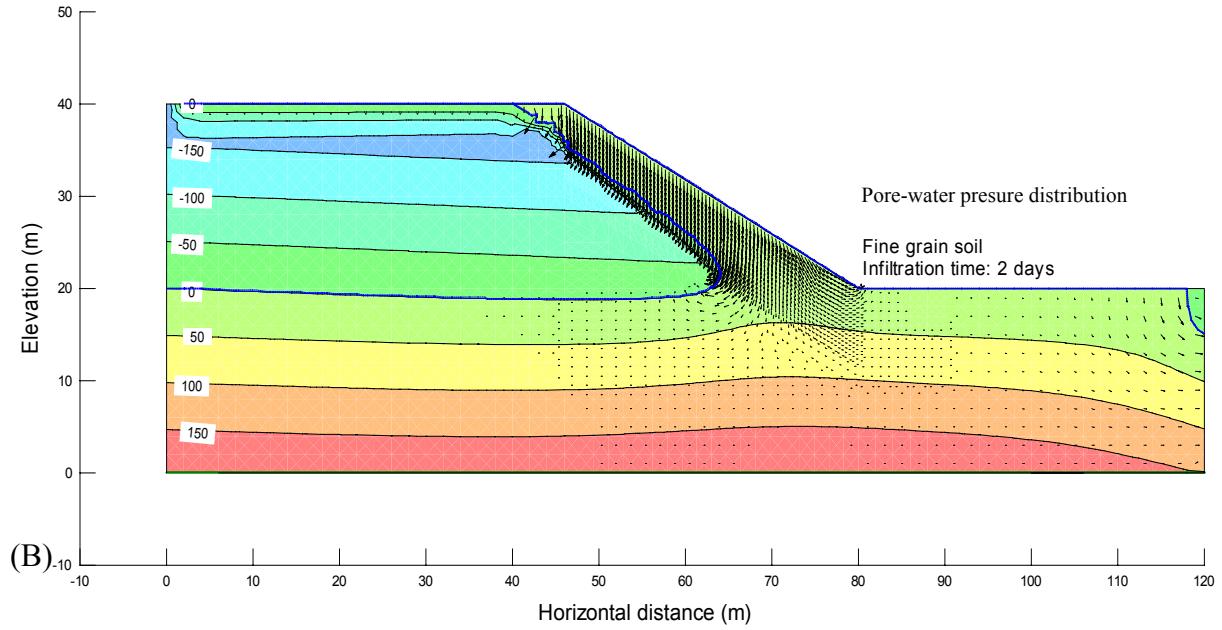

Figure 4-12: Flow net showing pore-water pressure (kPa) during the infiltration process in a fine soil after (A) 1 day and (B) 2 days of infiltration.

4.2.2 Effect of slope geometry

What effect could changes in slope geometry have on the pore pressure conditions within a slope? This question is rather important when considering the design of a slope or the analysis of a natural slope subjected to environmental changes. In order to study this aspect, numerical simulations of infiltration are conducted on slopes having inclinations ranging from 20 to 45 degrees. The simulations are conducted for both fine and coarse grain soils presented earlier in Figure 3-4. The finite element meshes for the 20, 26, 30 and 45 degree slopes are presented in Appendix B. The boundary conditions for the different slope geometry are the same as presented earlier in Figure 3-2. The toe of slope, for all geometries, is positioned at x=80m and y=20m. The height of the slopes is the same (20m) while the position of the crest is changing. Since the boundary conditions are the same, the initial groundwater level is 3 m under the toe for every slope.

Pore water pressure profiles are recorded at the middle of each slope during the transient rainfall. These are presented in Figure 4-13 A and B for a fine and coarse grain soil, respectively. As illustrated by these two figures, the geometry of the slope influences the pore water pressure response during the infiltration. The infiltration front, for both soils, is deeper for the steepest slope (45 degrees) and lowest for the more gentle slope (20 degrees).

To better explain these results, the governing equation for water flow in soil (Eq. 1-20) is rewritten in Equation 4-1 in terms of pore-water pressures.

$$\frac{\partial}{\partial x}\left(k_{wx}\frac{\partial H_w}{\partial x}\right)+\frac{\partial}{\partial y}\left(k_{wy}\frac{\partial H_w}{\partial y}\right)+Q=m_w\frac{\partial u_w}{\partial t} \qquad \textbf{Equation 4-1}$$

In this governing flow equation, the rate of increase in pore-water pressure is proportional to the permeability (k_w) of the soil in x- y-directions and the applied boundary flux (Q). For a given soil, these two parameters are taken to be equal and constant. However, by increasing the slope angle, the groundwater flow through the soil is subjected to higher hydraulic gradient. The changes in pore-water pressure with time are therefore faster for steeper slopes geometries.

From the results of Figure 4-13, the effect of the geometry is much larger in the coarse grain soil than in the fine soil. Why is it so? As mentioned above, the pore-water pressure time response is proportional to the hydraulic conductivity of the soil and the applied boundary

flux in the governing water flow equation. Since the desaturation coefficient for a coarse soil is greater than that for a fine soil, the same change in matric suction will lead to a greater increase in the coefficient of permeability for a coarse soil. In addition, in this simulation the k_s for the coarse grain soil is 50 times greater than that for the fine soil. The changes in hydraulic gradient for different slope geometries multiplied with the higher infiltration rate in the coarse soil, are then leading to higher geometry effect on the coarse soil slope.

There are also two other important facts to consider. The first is that the top boundary conditions lead to more water infiltration in the coarse soil. Would the results be different if having an infiltration flux equal for both types of soils? The second is that the results are time dependent. In this case, the results are shown after 1 day and 1.5 hour of infiltration for the fine and coarse soil, respectively. The comparison may be different if made after a longer time.

However, the results are still showing that differences in hydraulic properties of a soil can influence the effect slope geometry has on the pore-water pressures. Therefore, the pore pressure response cannot only be characterized by the geometry of a slope, but must also be related to the hydraulic characteristics of the soil slope.

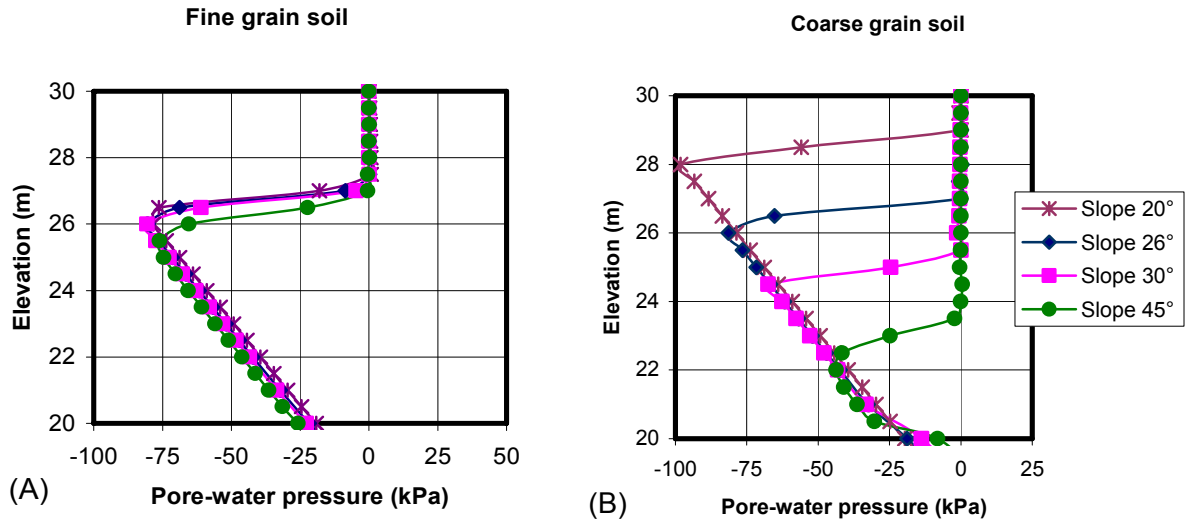

Figure 4-13: Pore water pressure profiles for different slope angles for (A) a fine grain soil after 1 day and (B) coarse grain soil after 1.5 hour of rainfall.

4.2.3 Adaptive time stepping routine: Nodal Heads vs. Vector Norms

As mentioned in Chapter 3, prior to any simulation, the selection of the convergence parameter in the numerical analysis is of great importance since it controls the final seepage solution. The aim of this section is to show how the different convergence scheme, in the adaptive time step routine, can influence the final seepage solution in the analysis

In all simulation results presented earlier, the adaptive time stepping routine is used as described in the GEOSLOPE software. This routine inserts extra time steps between the user specified time steps so that the head value changes are smaller than the user-specified percentage. In this routine, there are two schemes that can be used to monitor the allowable change in nodal heads. The first option, called nodal heads, scans every node individually in the mesh to see if the allowable percent head change is upheld. The second option, called vector norm, will scan every nodes simultaneously. This approach is faster for larger mesh problems. This is also the default option in the adaptive time step routine.

For a comparison of the two different schemes, the model slope of Figure 3-2 is again subjected to a transient water infiltration. This time, the vector norm scheme is selected in the adaptive time stepping routine. As earlier, the maximum percentage change in head per time step is specified to 2.5. Infiltration is carried out on the fine and coarse grain soil.

The results with the nodal heads option were presented earlier in Figure 4-8 while the results with the vector norm option are presented here in Figure 4-14. By comparing these two figures, it is possible to observe that the infiltration of water is faster when the nodal head option is selected. With this option selected, the infiltration front in the fine soil lies at the elevation 23m after 2 days while it takes 1.75 hour for the coarse soil to reach nearly the same elevation. With the vector norm option, the infiltration front lies at 24m after 4.5 days for the fine soil and at the same position after 5 hours for the coarse soil. Using the vector norm option, the pore pressure profiles are actually showing positive values behind the infiltration front. These positive values could cause the slower movement of the infiltration front. The differences in results from the two options seem fairly significant, and this should be noted when evaluating results presented by different authors and computer software.

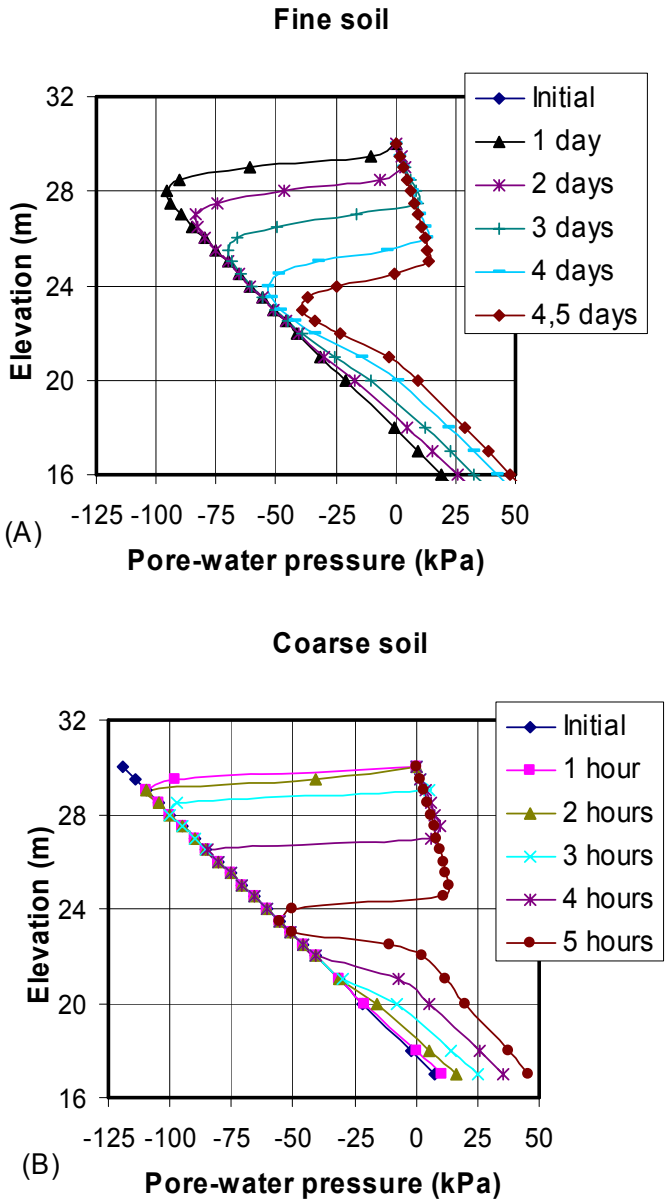

Figure 4-14: Pore-water pressure results for coarse and fine soil-slope subjected to intense infiltration (using vector norm).

4.3 Stability Analysis Results

Slope stability analyses are conducted on the fine and coarse grain 30 degree soil slope of Figure 3-2. The method used to perform stability analysis is discussed in Section 3.3. The investigated slip surfaces are presented in Figure 3-5. The purpose of the stability analyses is to study how the safety factor changes during an extreme rainfall event. Emphasis is given to the effect of the φ^b-angle, the air-entry parameter, and soil type (fine vs. coarse).

4.3.1 Effect of the φ^b-angle

In this first section, the simulations are carried out on the fine grain soil slope subjected to a two day rainfall event. The pore pressure changes during the rainfall are presented on Figure 4-9 B. Results from stability calculations are given in Figure 4-15 A and B for slip surface #1 (shallow) and slip surface #2 (deep) respectively (see Figure 3-5 for slip surface location).

For both surfaces, there is a reduction in the factor of safety with time. This is due to a gradual loss of matric suction during the rainfall event. The slope becomes less stable when increasing the rainfall duration. On these two figures, the effect of the ratio φ^b/φ' (0, 1/2, 3/4, 1) is illustrated. At a given time, a higher value of φ^b will lead to a higher safety factor. This is consistent with Equation 2-23 presented earlier. It is also observed that the rate of loss in stability with time is fastest for higher φ^b.

The lowest safety factor is obtained when the suction is completely ignored (i.e. $\varphi^b=0$) for both slip surfaces. In this case, the shallow surface presents a safety factor equal to one. The deepest surface presents a factor of safety of 1.2. This difference is due to the different steepness and geometry of the slip surfaces. The shallow slip surface is nearly parallel to the slope. When the cohesion and suction strength are null, the soil slope can only rely on the frictional strength. In the present case, the angle of friction ($\varphi'=30°$) is equal to the slope angle ($\alpha=30°$). Therefore, a slip surface lying parallel to the slope will show a safety factor close to one.

When studying the stability of an unsaturated slope subjected to rainfall, the choice of the slip surface is of great importance. Initially, in the simulation, the shallow slip surface shows a factor of safety nearly twice as large as for the deep one. However, the shallow slip surface is more vulnerable to environmental changes at the surface of the soil. After 1.5 days, the deeper

circle has only lost a fraction of its stability. However, along the shallow slip surface, the safety factor after 1.5 days is equal to one for every φ^b/φ' ratio. To explain this, one needs to look at Figure 4-9 B which shows the pore-water pressure in the soil slope at a depth of 2 m at different locations. On this figure, it can be observed that the infiltration front reaches the depth of the shallow slip surface after 1.5 days. After this time, the soil is fully saturated and the matric suction goes to zero (μ_a-μ_w) at every point along the shallow slip surface. The suction strength ((μ_a-μ_w)tan φ^b) in Equation 2-23 goes also to zero and the φ^b angle has no longer any effect on the stability calculation.

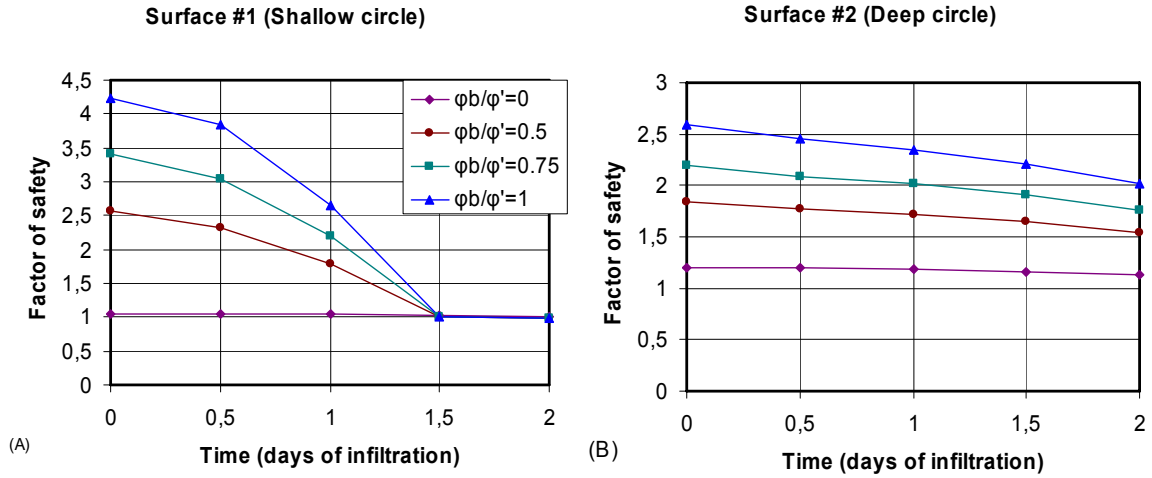

Figure 4-15: Changes in the safety factor with time for different ratios of φ^b/φ' (0, 1/2, 3/4, 1) on a (A) shallow and (B) deep slip surface.

4.3.2 Effect of the air-entry value on the stability

It is shown in Section 3.1 that the air-entry value affects the hydraulic conductivity function of a soil and consequently its time response to infiltration. The results showed that significant differences in the pore pressure profiles are induced by a change in the air-entry value. The question now is how big an error would be induced in the calculation of the safety factor if misjudging the air-entry value of a given soil? To answer this question, a 2 day rainfall simulation is carried out on the fine grain soil presented in Figure 3-4. The simulations are assuming that the air-entry value lies between 10 and 50. A value of 30 was previously used. Every other parameter is kept constant and the same as in the previous simulations. The stability calculations are conducted on slip surface #2 (deepest) of Figure 3-5.

Figure 4-16 A presents stability results as function of infiltration time for the fine soil. The results are given for the different air-entry values. In this calculation, the ratio $\varphi^b/\varphi'=1$. As shown, the differences among the safety factors increase with time for the different "*a*" values. As mentioned earlier, the lower the "*a*" value of a soil, the lower the hydraulic conductivity at a given matric suction. Consequently, the lower the infiltration rate, the lower the loss of matric suction with time. This leads to a lower loss of suction strength with time. Following this, the factor of safety will decrease at a slower rate for a soil having a low "*a*" value, as shown in Figure 4-16 A.

In Figure 4-16 B, results are presented after 2 days of infiltration and the safety factor is given as function of the air-entry value for different values of φ^b/φ'. Again, one observes that with an increasing φ^b/φ' ratio, the safety factor increases significantly. Moreover, it is evident from this figure that the air-entry value affects the stability of a slope subjected to infiltration. The factor of safety for the soil presenting an air-entry value of 10 is much larger than for higher air-entry values. The lowest factor of safety is obtained for the soil presenting an air-entry value of 50. For this one, the infiltration rate is higher and consequently the loss of matric suction is much faster. Therefore, this soil slope is nearly at rupture.

Let us assume that the real or correct air-entry value for the fine soil is 30. What will be the error introduced to the safety factor, if this air-entry value is not correctly approximated in a simulation? Figure 4-17 shows the percentage error in the factor of safety due to an error in approximating this air-entry value. The lines are showing a tendency to flatten with increasing negative error of the air-entry parameter. In the worst case, one would set the air-entry value close to zero. This would lead to a very low coefficient of permeability at a given suction range. Consequently little water would infiltrate the soil and the safety factor would not be affected by the simulated rainfall. The safety factor is then overestimated.

In the case were one would overestimate the air-entry value of a soil, the error on the safety factor calculation would continually increase. By overestimating the air-entry value in an extreme manner, the hydraulic conductivity of the soil would be near to its saturated value for almost every possible range of natural matric suction. The infiltration in the soil would therefore happen rapidly and the soil would get saturated. This would lead to larger and larger underestimation of the safety factor. As observed from Figure 4-17, an error in the air-entry value estimate will lead to small errors in the calculation of the safety factor even if the

suction strength is assumed to be zero ($(\mu_a-\mu_w)\tan \varphi^b=0$). This is because the air-entry value affects the rate of infiltration in the soil and consequently the rate of positive pore pressure build-up.

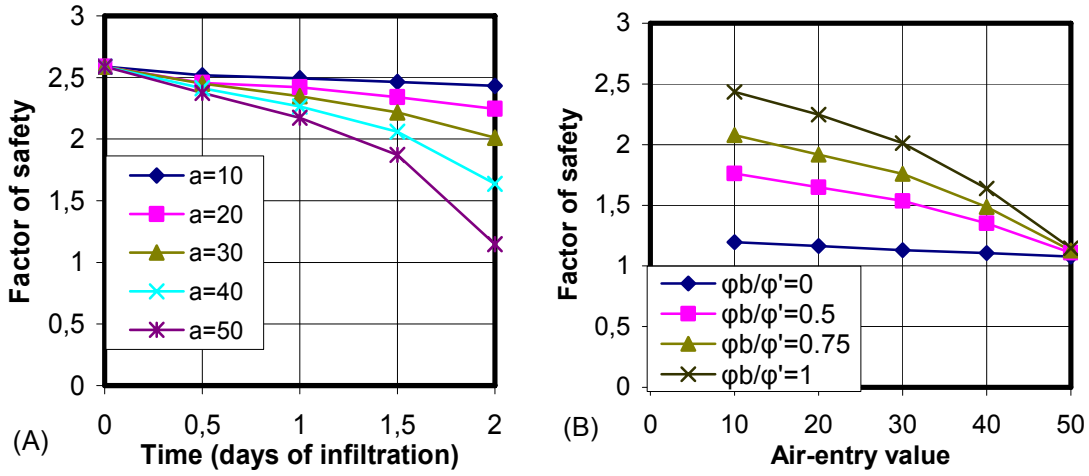

Figure 4-16: (A) Factor of safety versus infiltration time for a fine soil using different air-entry values (φ^b/φ'=1). (B) Factor of safety versus the air-entry value of a fine soil (t=2 days infiltration).

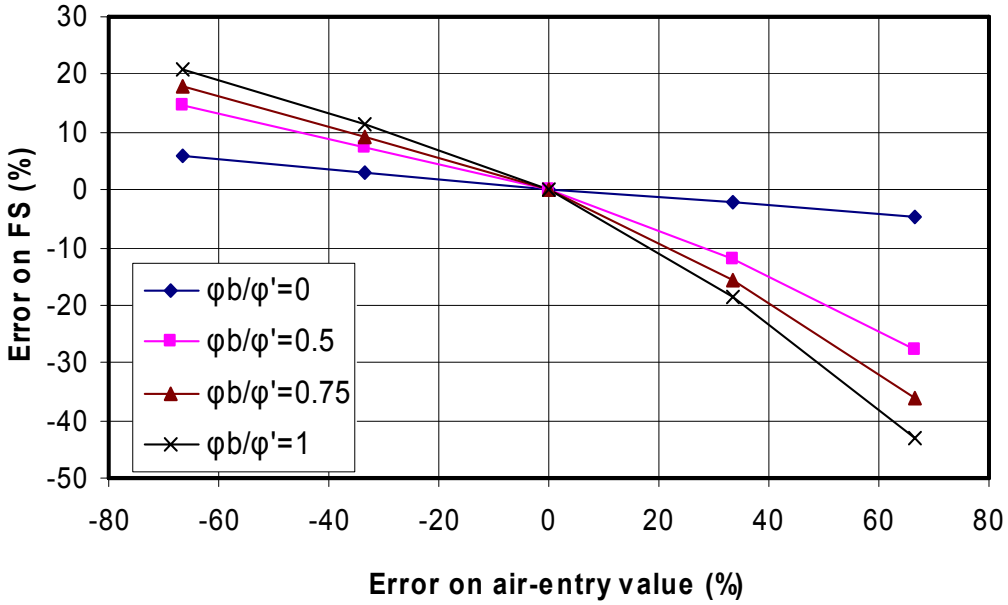

Figure 4-17: Effect of an error in assessing the air-entry value on the factor of safety.

4.3.3 Coarse versus fine grain soil

As observed in the flow nets of Figure 4-11 and 4-12, the infiltration pattern in a coarse and a fine grain soil slope are different. The objective of this section is to study which type of failure may first occur in these different types of soils. The pore-water pressures from the simulations of Section 4.2.1 are taken as input in the stability calculations. The strength parameters are equal for both types of soils, as described in Section 3.3. The stability calculations are performed on slip surface #1(shallow) and #3(toe) of Figure 3-5.

Figure 4-18 A and B present the results of the stability calculations for the coarse and fine grain soil, respectively. Initially (time=0), both soil slopes are showing the same safety factor on the given slip surfaces. Both soils are showing a reduction of the safety factor with increasing infiltration time. Since the saturated permeability of a coarse soil is higher than that of a fine soil, infiltration occurs faster. Consequently, the safety factor decreases more rapidly in the coarse soil, and failure occurs along slip surface #3 (toe) after 1.75 hours. For the fine grain soil, failure occurs first along slip surface #2 (shallow) after 1.5 days. At the same time, the safety factor along slip surface #3 is only slightly higher than 1.

These results are showing that the model slope is responding in a different manner for the coarse and fine soil. The coarse grain slope model presents the first signs of instability at the bottom of the slope. However, the fine grain soil slope fails along a shallow slip surface along the entire slope.

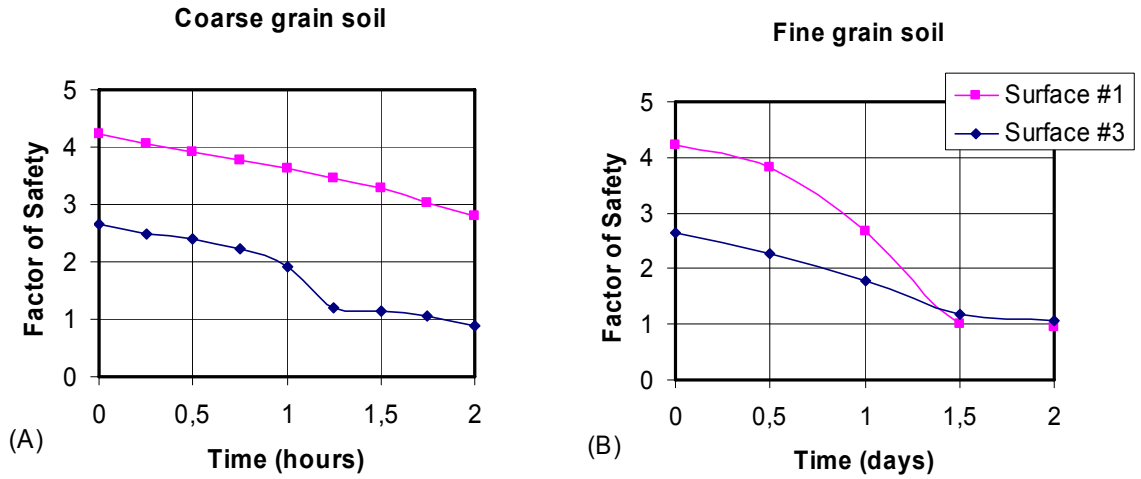

Figure 4-18: Stability calculations on slip surfaces #1 and #3 for (A) coarse grain soil and (B) fine grain soil.

CHAPTER 5 Discussion of Results

Many different parameters were investigated in the numerical analyses. The aim of the present chapter is to discuss, how and why, the different parameters are affecting the pore pressure distribution in an unsaturated soil slope. Emphasis is given to the hydraulic differences between a fine and coarse grain soil.

5.1 Loss of Suction in Unsaturated Slopes

As shown in Chapter 4, the suction present in an unsaturated soil slope model tends to diminish or to completely disappear when subjected to water infiltration. The negative pore pressures in the slope are likely to dissipate at the toe and in the lower part of the slope in the initial stages. The pore pressure increase thereafter moves upwards. Edgers and Nadim (2003) suggested that this occurs because the change in slope angle at the toe of the slope concentrates the flow lines and increases the hydraulic resistance to lateral flow. However, base on the findings in this thesis, it seems that the infiltration pattern in the slope is more affected by the soil hydraulic properties and the initial suction profile in the slope.

From the simulations in Section 4.2, it can be concluded that the difference in suction between the bottom and the top of the slope is equal for the fine and coarse grain soil models. This is due to the assumed same initial groundwater conditions and the use of a hydrostatic suction profile. Compared to a fine soil, the coarse soil presents a much bigger difference in permeability from the bottom to the top of the slope for an equal suction difference. If the permeability function is very steep, the hydraulic conductivity at the bottom of the slope may be many orders of magnitude greater than that at the top of the slope. Initially infiltration will therefore occur at the toe of the slope. The flow velocities will then be much higher at the bottom of the slope. Very low permeability at the top of the slope will lead to low flow velocity in this coarse material.

Due to its gentler permeability function, the fine soil will present a more even infiltration pattern along the slope. Flow velocities in this soil are also showing much more similar values at the top, middle and bottom of the slope. In this case, since the permeability is nearly the same everywhere in the slope, the hydraulic gradient controls the flow velocity. The velocity

will be higher in the middle and top of the slope where the hydraulic gradient is higher as is illustrated in Figure 4-10 B.

These differences may be important for the assessment of the stability of slopes. For the same infiltration flux, a soil slope could fail via different mechanisms. In the case of a coarse soil, rupture may initiate at the foot of the slope due to a rapid build-up of pore pressures. On the other hand, a fine soil slope is prone to loss of matric suction along the entire slope. In this case, the infiltration pattern may lead to shallow translational type of sliding.

The initial groundwater conditions also affect the infiltration pattern in a slope. A shallower groundwater table would lead to lower suction values and consequently higher permeability values. The infiltration rate at the top and the bottom of the slope would hence be even closer for a fine grain soil. This could also be caused by antecedent rainfall on a slope. It is shown in the simulations that antecedent rainfall may reduce negative pore pressures within the soil. In this case, the coefficient of permeability would be distributed more evenly after the antecedent rainfall. Higher hydraulic gradients in the slope may thereafter produce higher flow velocities and infiltration rates at the top and middle of the slope than at the foot.

5.2 Effect of hydraulic parameters on pore pressure response during rainfall

Results of numerical simulations in Section 4.1 are showing that the magnitude of the saturated coefficient of permeability affects the pore-water pressure time response in a slope. For a constant infiltration flux to saturated coefficient of permeability ratio, the higher the value of k_s, the faster the infiltration will be. In each simulated case, a q_b/k_s ratio close to one, gave the fastest decrease in matric suction.

For a steady-state infiltration flux lower than the saturated coefficient of permeability, suction in a soil does not completely disappear, because the infiltration leads to a volumetric water content value lower than the saturated one. Suction is therefore maintained in the soil. In the analysis of soil slopes subjected to infiltration, importance must therefore be given to the q_b/k_s ratio and consequently the rate of rainfall. In addition, the hydraulic characteristics of the soil which define the permeability function are of great importance.

5.2.1 Air-entry value

In Chapter 4, it is observed that the infiltration fronts for a fine soil are more diffuse than for a coarse soil. This is due to the differences in hydraulic characteristics between the two soils and, more precisely, their different air-entry values. Kish (1959) derived an equation for one-dimensional steady flow in a soil subjected to a constant infiltration at the ground surface:

$$\frac{\partial u_w / \rho_w g}{\partial y} = (q/k - 1) \qquad \textbf{Equation 5-1}$$

In this equation, when the infiltration flux (q) approaches the coefficient of permeability (k), $\partial(u_w / \rho_w g)/\partial y$ tends to zero and the pressure head $(u_w / \rho_w g)/y$ tends to be constant. As shown in this work, at initially high matric suction, a coarse soil will present a hydraulic conductivity lower than that for a fine soil. In the simulated case of Section 4.2, the initial hydraulic conductivity for the coarse soil is much lower than the one for fine soil in the middle of the slope. Given that the infiltration flux is constant and equal to the saturated coefficient of permeability, for both cases, the ratio $q/k_{unsaturated}$ will be much greater for the coarse soil. Consequently, the gradient of pore-water pressure is higher for a coarse soil.

As shown, in the diagram of Figure 2-11, a high pore-water pressure gradient in a soil leads to a nearly horizontal infiltration front. This effect would be amplified if the difference in the air-entry value would be higher between the fine and coarse soil and is shown by the results of Figure 4-4. In the light of these results, it seems possible to tell if a material is highly or little prone to the development of a perched water table when subjected to infiltration. This could be achieved by carefully studying the hydraulic characteristics of a soil and the infiltration conditions.

Finally, the air-entry value affects the stability of a given slope since it controls the infiltration rate in a soil. Stability analyses neglecting the suction strength must also pay attention to the air-entry value and other hydraulic characteristics of the unsaturated soil. This is because the hydraulic characteristics of the unsaturated soil are controlling the flow of water above the groundwater table and consequently the building-up of positive pore-water pressures in the slope.

5.2.2 Desaturation coefficient, *n*

From the results of Section 4.1.4, one may see that the desaturation coefficient is also important. The magnitude of this coefficient affects the pore-water pressure response of a slope subjected to infiltration. By looking at Equation 2-20 for the water flow for saturated and unsaturated soils one may observe that the magnitude of the desaturation coefficient affects the coefficient of permeability. In this same equation, the coefficient of volumetric volume change (m_w) is the arithmetic slope of the soil-water characteristic curve, and changes also with the desaturation coefficient.

As shown by Zhan and Ng (2004), it seems that the sensitivity of the desaturation coefficient depends on the range of negative pore-water pressure within the soil. As illustrated in Section 4.1.1, the sensitivity of this coefficient also changes during the infiltration process.

5.3 Numerical Issues

Numerical analyses are being more and more popular within the field of geotechnics. Software and computers are developing at an increasing rate. Joined with powerful techniques, like the finite element method, analytical methods are moving from research tools to engineering application tools. The fact that this technique is very powerful does not mean the solution to a given problem will always be correct. Obtaining useful results from these tools depends on the guidance provided by the user. The users understanding of the input, convergence parameters and interpretation of the results is essential.

In Section 4.2.3 it was shown that differences in convergence parameters/criteria are leading to different computed results. Using the vector norm method in the adaptive time stepping scheme leads to development of positive pore-water pressure above the infiltration front, while the nodal head method leads to zero pore pressure values above the infiltration front. The vector norm option saves time in the calculation process but the results seem questionable. One should therefore be very careful when using default options in software, without critically evaluating the outcome of the analyses.

It was shown by Collins and Znidarcic (2004) that positive pore-water could develop above the infiltration front. The present discussion is neither aimed at criticizing their results nor saying that these were induced by numerical divergence problems in the calculations. There

are in fact many other input parameters which could lead to the difference in results obtained by Collins and Znidarcic (2004) and the author of this thesis. For example, Collins and Znidarcic (2004) used an infinite slope analysis. In addition, they only considered vertical flow in their model. In this thesis, a 2-D model slope was used, and these differences may lead to different infiltration patterns.

CHAPTER 6 Case Study – The Åmot Slope Failure

6.1 Site Description

In the fall of 2000, abnormally intense rainfall fell on the south-eastern part of Norway. The extreme weather conditions led to numerous slope failures. The small town of Åmot in the district of Modum was particularly affected (see Figure 6-1). A major slope failure happened on November 22, 2000 after an extremely wet fall. This failure endangered 24 houses and threatened their residents. Eleven houses were immediately evacuated. The Meteorological Survey of Norway calculated the total amount of rainfall to be 4 times the normal in the south-eastern part of the country during the fall of 2000.

Following these slope instabilities, investigation work was immediately carried by the Norwegian Geotechnical Institute (NGI). Information from boreholes and cone penetration testing was collected on the 38 degree slope and the plateau above. This information is available in NGI Report No. 20001533-5. The upper 20 m of the slope are composed of fine brown sand with some silt/clay interlayers. The shallow slope failure took place in this sandy material. The underlying 40 m are composed of silt and clayey material. This clayey material is described as sensitive, but not “quick” in the NGI Report.

In 2002 it was concluded by the authorities and the NGI, that these shallow instabilities were creating a potential threat to triggering bigger slides involving the underlying clay formation. A slide involving the clay could be catastrophic for the region. The surrounding residents were at risk. The sliding mass could also run down and block the Drammen River. This could have a disastrous impact on the community downstream of the river (the city of Drammen for example) in addition to the many power plants along this river. The Railway system which runs along the river would also be affected by such a slide. Mitigation work was therefore immediately carried out in 2003. It was chosen to reduce the slope angle and install some surface drainage. The vegetation cover (mature trees) was also reduced and some younger trees were planted after the work was finished. Houses at risk were expropriated. The terrain at this location has after the mitigation work an average slope of 2H:1V. Conditions of the slope during the mitigation work are presented in Figure 6-2. It can be observed, from the different tones of grey, that the water level is high in the slope. The uppermost blue line

represents were the water table emerges on the face of the slope. The present slope conditions are illustrated in Figure 6-3.

With the help of geophysical instruments, own by the Department of Geosciences at the University of Oslo, some additional field work was carried out by the author at this site during July 2004. The results are presented in Section 6.2. The goal of this work was to get some more information about the soil type, water content and boundary conditions. In addition, the author carried out laboratory experiments to calculate the SWCC of the Åmot sand. The results of these are presented in Section 6.3. The geophysical and laboratory results are then used in Section 6.4 to numerically back-calculate the slope failure. Could this failure in November 2000 have been predicted? Was this failure due to a rapid increase in the groundwater level, or is it due to a loss of matric suction of the soil?

Figure 6-1: Location of the study field in the community of Åmot, county of Modum (Map 1714 I, UTM reference 32V NM 507 398)

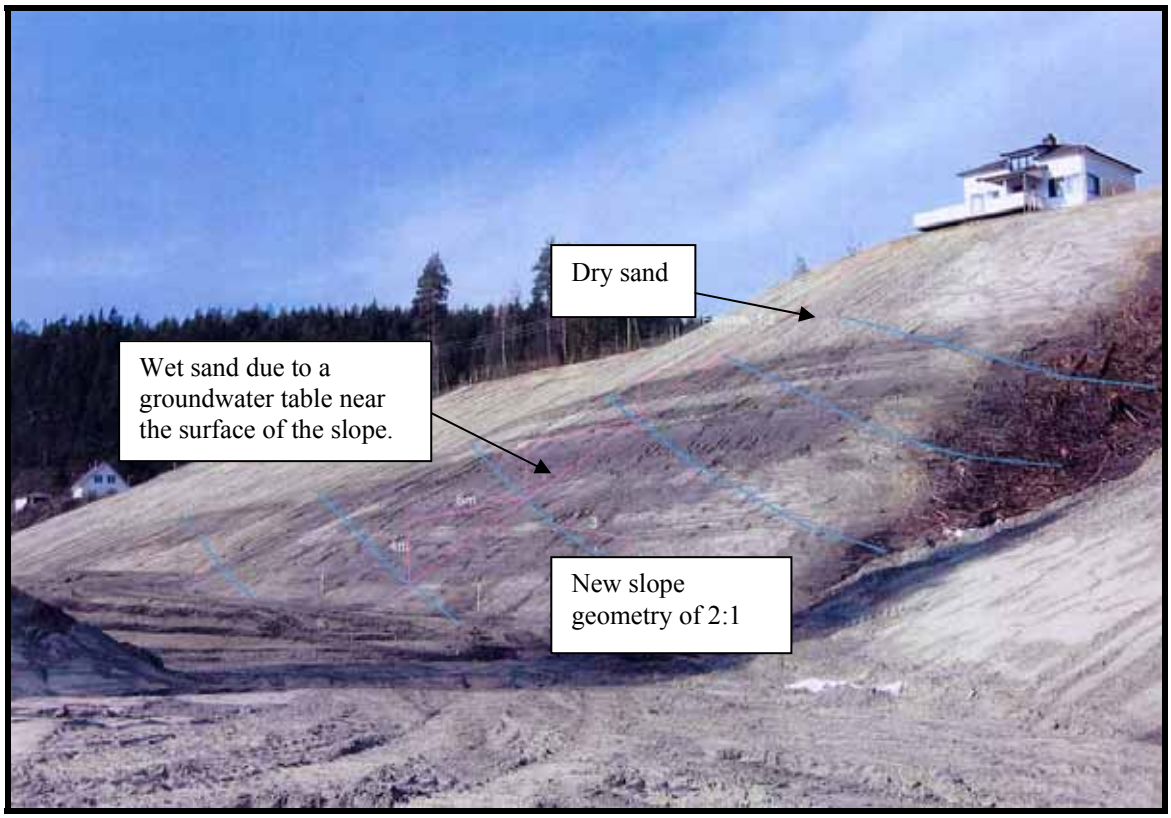

Figure 6-2: Conditions on the Åmot slope during the mitigation work in 2003 (Photo courtesy of NGI)

Figure 6-3: Location of field study and present slope conditions in Åmot near Kongfossen.

6.2 Results from the Field Investigations

The field investigation was carried out during the last week of July 2004. The weather conditions at the time were sunny. The specific position of the survey profiles was chosen below the house shown in Figure 6-2. The detail survey locations are given in Figure C-1 (Appendix C). The surveys are located at the same level where the sliding occurred in 2000. The investigated slope is nearly 48 m long and the slope is 2H:1V.

Prior to conducting any geophysical work, a site walkover survey was undertaken. This helped getting familiar with the study site and to anticipate problems which could arise during the geophysical investigation.

On the profile grid presented in Figure C-1 (Appendix C), small observation holes were made and samples were taken for laboratory analyses. In-situ water contents were determined and the results are shown in the grid of Figure C-1, at the positions where the samples were taken. The results are showing that the top 24 m of the slope is fairly dry with in-situ water content in the order 2-3%. From the middle of the slope and downwards the water content increases up to values of 28%. This demarcation can also be observed from the different vegetation tints on the surface of the slope (i.e. brown and green). Figure 6-2 shows also that the water content in the slope is high at nearly the same position with the different tones of grey. Pictures A, B and C in Figure C-2 (Appendix C) are taken along the profile (x=0m) of the grid in Figure C-1. These pictures illustrate the soil conditions along the survey profile (3m, 24m and 32m from the top of the slope) and the images are taken from between 0.4 and 1m depth. In picture A the dry crust at the top of the slope is seen. Picture B presents the fine sand with interlayed silt and Picture C illustrates the high water content at the bottom of the slope.

With the help of geophysical methods, one attempts to get a better overview of the soil stratigraphy. However experience shows that the measurements are often difficult to interpret. Measurements of the moisture content in the soil slope were also made, and the groundwater level and the boundary conditions surrounding the slope were determined. Another purpose of this work in this thesis was to explore the applicability and reliability of the methods for such purposes. Two main geophysical methods were used to get a better knowledge of the soil slope sub-surface, the electromagnetic method using the ground penetrating radar and the electrical method using the so-called ohm-mapper.

6.2.1 Ground penetrating radar results and interpretation

Ground penetrating radar (GPR) measurements were conducted using a RAMAC acquisition system. The data were processed by the author using the REFLEX/W software. The processing steps included a static correction, substration of the mean dewow, a background removal and finally a quasi-linear gain in depth was applied. Two types of surveying profiles were conducted on the slope, common mid-point (CMP) and reflexion. A 100 MHz unshielded antennae was used to collect CMP profiles and a 250 MHz shielded antennae was used in the reflexion surveying mode. A detailed description of the GPR instrument and theory is given in Appendix D.

CMP Profile Results

A common mid-point profile was collected at the bottom of the slope, where the ground was bare of vegetation. This type of surveying is necessary to get an estimation of the wave propagation velocity.

Results are shown in Figure E-1 in Appendix E. A velocity value of 0.105 m/ns can firstly be calculated from the direct wave in Figure E-1. The value is nearly the one for dry sand in Table 6-1. The value of 0.105 m/ns may represent the dry crust on the soil surface. Moreover, wave propagation velocities are also calculated from the reflected waves of the same profile. For deeper reflectors, the velocity seems to be lying around the value of 0.055-0.061 m/ns. This velocity value defines a wet sandy material in Table 6-1.

From these velocity calculations, one can calculate the relative permittivity (ε_r) of the soil:

$$\varepsilon_r = \left(c/V\right)^2 \qquad \textbf{Equation 6-1}$$

In Equation 6-1, c is the electromagnetic wave velocity in the air equal to 0.3 m/ns and V is the wave propagation velocity in the soil.

The relative permittivity (ε_r) is defined as the ability of the material to get electrically polarized. It is found to be $\varepsilon_r = 8.16$ in the dry crust and $\varepsilon_r = 25$ below, from the velocity results and Equation 6-1. These calculated permittivity values can now be inserted in Topp's (1980) equation:

$$\varepsilon_r = 3.03 + 9.3\theta_v + 146\theta^2{}_v - 76.6\theta^3{}_v \qquad \textbf{Equation 6-2}$$

In Equation 6-2, θ_v is the volumetric water content of the soil. With the help of this equation, the volumetric water content at the bottom of the slope is found to be nearly θ_w = 0.165 in the dry crust and θ_w = 0.35 below. As will be shown by the laboratory results of Section 6.3.1, the saturated value of volumetric water content (θ_s) for the fine sand is nearly the same as the one calculated below the dry material.

The objective was to collect many CMPs results in order to get a better knowledge of the moisture condition along the slope. Unfortunately, no other good CMP profile was obtained. Problem occurred with the unshielded antennae. The wave front seemed to be attenuated by the thick layer of dry grass in the slope (see Figure C-2). Profiles were taken parallel and perpendicular to the slope without success. On the road above the slope, the radar energy was scattered due to the presence of fences and other metallic objects in the ground.

Table 6-1: Electrical properties of some common materials

Material type	Relative permittivity	V (m/ns)	Electric Resistivity (ohm-m)
Air	1	0.30	Infinite
Fresh water	80	0.033	0.5-300
Dry sand	3-5	0.15	800-5000
Saturated sand	20-30	0.055-0.06	10-800
Silt	5-30	0.07	-
Clay	5-40	0.05-0.17	1-100

Reflexion Profiles Results

Reflexion profiles were conducted on the plateau above the slope. The resulting radargram is presented in Figure E-2 in Appendix F. The profile taken on the plateau is not straight due to the many trees. The length of this profile is nearly 50 m and the end is at ca. 100 m from the crest of the slope. A wave velocity of (V=0.06 m/ns) is used to calculate the depth axis on the radargram of Figure E-2.

As illustrated by the results of this profile, there seems to be a dip in the soil beddings from north-east to the south-west. However, the dipping is greatly exaggerated by the scale effect on the radargram. This profile presents a good resolution up to a depth of 2 m. The wave propagation is much attenuated near a depth of 2 m. This is due to a sudden rise in the water content of the soil. This attenuation continues until a depth of 3.2 m. Beyond this depth the wave propagation is almost totally attenuated. From the radargram results, it is not possible to clearly define a groundwater table. The reason for this may be that the ratio of the thickness of the capillary zone to the wavelength of the incident radiowaves is too high. This is important in order to provide a sufficient contrast in relative dielectric constant between the unsaturated and saturated material to reflect a significant proportion of the energy.

A reflexion profile was also taken along the slope at position x = 0m of Figure C-1. The radargram is presented in Figure E-3. Topographic corrections were made on this profile. At the top of the slope, the wave penetration is nearly 4 m but decreases between 0 and 20 m. This is due to the high water content at the bottom of the slope as presented earlier in Figure C-1. It is again possible to observe some stratification in the sand. These are probably due to the silty layers present in the sand mass. One can easily see the surface drainage in the middle of the slope at position 19m. This surface drainage can be observed on the profile grid of Figure C-1. The boulders are producing scattering of the radiowave and multiples can be observed at this location.

It can be observed that the silt interlayers, on the last radargram profile, are dipping at the top of the slope while they are nearly horizontal at the bottom. In reality, they may all be horizontal. The same wave velocity (V =0.06m/ns) is used to calculate the depth values on the radargram. This is accurate for the bottom material which is wet, but incorrect for the top layers of sand. The depth of the dryer reflectors at the top of the slope should be calculated with a greater velocity. However as mentioned earlier, no velocity could be calculated at the top of the slope.

6.2.2 Resistivity Results and Interpretations

Electrical resistivity measurements of earth materials involve the introduction of an electric current into the ground and the measurement of the material resistance to the induced current. A complete description of the resistivity theory and the Ohm Mapper instrument is given in Appendix F.

2-D electrical profiles were acquired with the Ohm Mapper instrument along the multiple parallel of Figure C-1 and on the plateau of the slope. The purpose of these multiple lines was to study lateral variations of resistivity profiles in the slopes at this specific location. Data were thereafter inversed by the author with help of the RES2DINV software from GEOTOMO.

To inverse the resistivity results, the least-square inversion method was used for 2-D surveys. This method was used together with the finest mesh refinement and 4 nodes integration. The first resistivity profile was conducted on the plateau and the inversion results are shown in Figure G-1 (Appendix G). This profile was conducted at the same location as the georadar profile, on the plateau of the slope. The results give a wide range of electric resistivity values up to a depth of 6 m. The lowest values are approximately 240 ohm-m while the highest are nearly 6500 ohm-m on the surface. These values are typical for sandy soil (Table 6-1).

The high values of resistivity are due to a very dry sandy soil at the surface. The rapid drop of resistivity value is due to the increase in water content with depth. It is difficult to exactly position the groundwater table in Figure G-1. It seems to be lying at a depth of ca.5 m. However, the boundary is not distinct. There is a gradual change in resistivity from 1.5 to 5 m depth. This is due to a gradual rise of the water content in the soil until it reaches saturation at the groundwater table level. Beyond this 5 m point the resistivity values are constant. These results therefore suggest that past the depth of 5 m, the soil is in a saturated state. A volumetric water content profile is presented in Figure G-1 B to illustrate this fact. This volumetric water content profile is calculated from the normal infiltration flux in the region and the SWCC together with the SEEP/W software. This is presented later in Section 6.4.1. The saturated volumetric water content ($\theta_{sat.}$) on Figure G-7 B was calculated in the laboratory and is described in Section 6.3.1. It can be observed that the value of ($\theta_{sat.}$) is the same as that calculated with the georadar and the CMP method for reflectors under the dry crust. The volumetric water content in the dry crust, simulated in this profile, is however a little lower than the one measured with the CMP method.

Resistivity measurements were also conducted along the slope, in front of the house as illustrated in Figure C-1. Data where acquired on the slope at line intervals of 2 m. Due to the presence of a surface drain in the centre of this slope, much noise was recorded with the electrical method. The best 2-D inversion profile obtained at this location is presented in

Figure G-2 (Appendix G). This profile is taken along the slope on the x = 0 m line. Data were acquired to a depth of 6 m along the slope. The results are showing a clear demarcation at 20 m from the bottom of the slope. The resistivity values above this location are mainly above 100 ohm-m. From 0 to 20 m the values of resistivity tend to be under 100 ohm-m.

As seen in Table 6-1 the electrical resistivity for a clayey soil lies in the range 1-100 ohm-m. In addition, resistivity values for very wet sand can also lie in that range. Therefore, the bottom 20 m can be classified as being a mixture of clay and sand. The upper 20 m gives typical resistivity values for a sandy soil which is dryer. This is in agreement with the fieldwork results obtained by the NGI in 2002. In the NGI Report No. 20001533-5, the NGI proposes that the clay interface lies below position 0.0 of this last profile.

It can be seen that the values of resistivity of the sandy soil are lower than those presented earlier in Figure G-1. This is due to higher water content in the face of the slope as illustrated in the picture diagram of Figure 6-2 and C-1. A resistivity structure can be observed between 22 and 24 m on the profile. This structure presents a depth of ~3.5 m. By looking again at Figure C-1, one can observe that a surface drain with heavy boulders is located at this position on the slope. It is not known if these penetrate as deep as 3.5 m. The structure could be exaggerated on the resistivity profile due to an abrupt change in the soil properties. The low value of resistivity illustrates that the drain catches water.

6.2.3 Critics and comparison of the geophysical methods

The ground penetrating radar is a very useful and rapid method of determining structures in the subsurface soil. Compared to the OhmMapper resistivity method, the GPR is easy to pull up and down the slope. The OhmMapper is difficult to utilize on a short slope due to the length of its configuration. Connection problems have been experienced between the transmitter and receiver dipole and the console during the fieldwork. This seems to be due to the heavy load on the cable connections when a long array is used (over 20m of length). Further work also proved that field investigations with the instrument under humid weather conditions were difficult. This again is due to problems of data transmission from the receiver to the console.

The wave penetration of the GPR transmitting antenna was attenuated by the presence of water in the soil slope. This is due to the high relative permittivity of this matter. The GPR results on the plateau of the slope are showing good results, but the wave penetration is shallow compared to those with the resistivity method. A lower frequency transmitting antenna should have been used for the purpose of this work. The frequency should have been in the order of 50-100 MHz.

The unshielded antenna used for the CMP profiling did not work as expected. It seems that the energy was much attenuated by the thick grass lying on the slope. Due to the lack of CMPs profiles, no water content determination could be performed along the slope with this method.

Overall, the results obtained with the OhmMapper are much better than those obtained with the GPR. The OhmMapper results helped determining the position of the groundwater level on the plateau of the slope. In addition, they are showing how the stratigraphy and water content gradually change along the slope. The depth penetration is nearly twice that with the GPR method.

6.3 Results of Laboratory Experiments

6.3.1 Soil-water storage function

Laboratory experiments to study the moisture characteristic of the fine sand from Åmot were performed during the fall of 2004. The Tempe Pressure Cell apparatus and testing procedure, described in Chapter 2, was set up and used by the author for this purpose. A total of 3 series of experiments were performed to define the water retention characteristics for this soil. Each series was conducted with four cells. All experiments lasted a period of nearly two months to assure that equilibrium was reached at every level. In order to classify the soil, grain size distribution curves were determined and the results are presented in Figure H-1 (appendix H). These were determined by using the dry sieving method. From this Figure H-1, the soil can be classified as fine sand with approximately 20% of silt-clay fraction.

The results of SWCC are compiled and shown in Figure 6-4. Detailed results of each series are given in Appendix H (Figure H2 to H4). The results of Figure 6-4 are presented with the Fredlund and Xing (1994) model curves described earlier in Chapter 2. This model is using the *a, m* and *n* parameters. The results from the experiments are clearly representative for fine sand. The air-entry values (6.6-10) are typical for this type of soil (see Table 1-1). The desaturation coefficient parameter (*n*) is lying around a value of 6. This is a rather high value, which tells us that the soil loses water rapidly when increasing the suction. The soil-water characteristic curve is therefore steep. The desaturation coefficient (*m*) in the high suction range lies between values of 0.4 to 0.8.

The Arya and Paris (1981) model curve is also shown together with the results of Figure 6-4. This model uses a physico-empirical approach to predict the water content changes in a soil as function of the matric suction based on the particle size distribution data and bulk density.

As illustrated in Figure 6-4, the Arya and Paris model represents well the Åmot laboratory data. The air-entry value calculated from this model is well defined by a value of 11 kPa. This is close to the experimental values. There is however a difference between this model and the experimental curves for the desaturation coefficient in both the low and high suction range (*n* and *m*). The desaturation coefficient (*n*) calculated with the Arya and Paris (1981) method is lower than the experimental data while in the high suction range, *m* is higher.

On the graph of Figure 6-4, it can be observed that the saturated volumetric water content changes from 0.275 to 0.35. This difference is due to a laboratory error during the third experimental series. In the first stage of the experiment, it takes time to fully saturate the soil. This stage was underestimated in the 3rd test series. Therefore lower saturated volumetric water content is obtained for this series. The subsequent analyses will assume that the saturated volumetric water content of the sand in Åmot is 0.35. This value was also calculated from the ground penetrating radar and the CMP method.

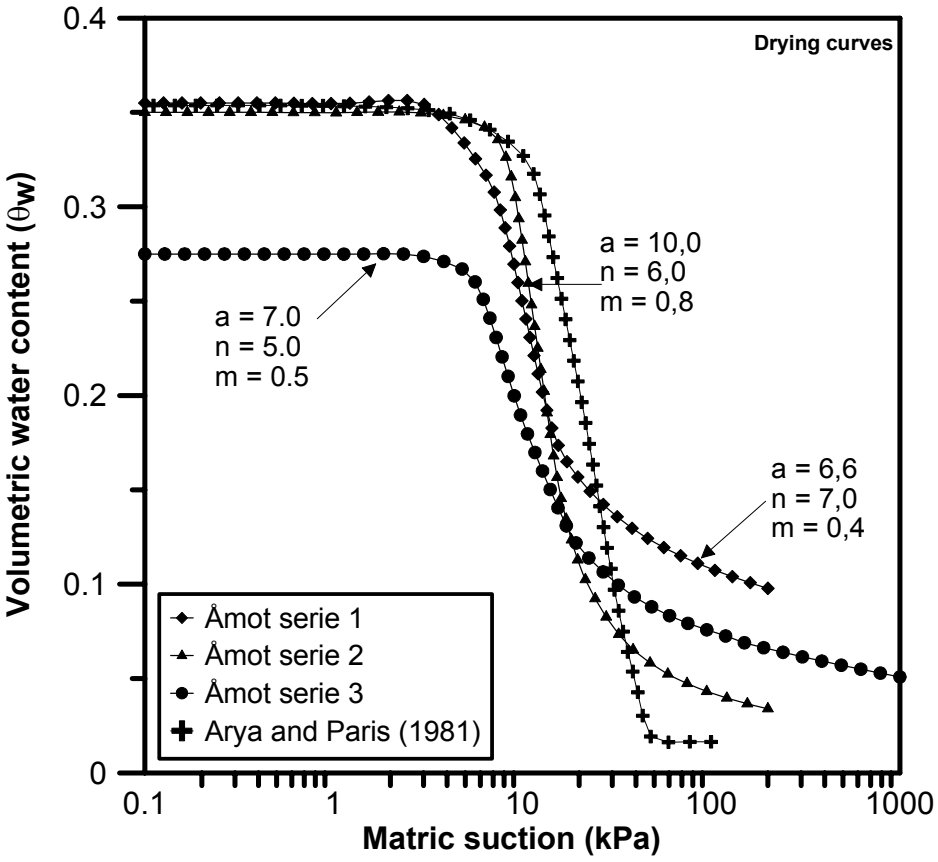

Figure 6-4: Results of SWCC for 3 series conducted on the fine sand from Åmot.

6.3.2 Hydraulic conductivity results

The constant-head method described in Section 2.1.2 was used in the laboratory by the author to calculate the saturated coefficient of hydraulic conductivity (k_s). This method was conducted on three different samples of the Åmot sand in order to get a good approximation of the k_s. The results obtained from these experiments gave a range of saturated permeabilities lying between 2.6 x 10^{-7} and 4.7 x 10^{-8} m/s. A complete overview of the permeability experiment results and calculations can be seen for series 1, 2 and 3 in Tables H-1, H-2 and H-3 respectively (see Appendix H).The first sample had a dry density (ρ_d) of 1.63 g/cm^3 while it was 1.65 g/cm^3 for the second and third samples. There was some minor washing out of fine particles during the second test. This could be why the value of saturated conductivity is a little higher for this sample.

Adding these results to the measured SWCC, it is possible to indirectly determine the soil conductivity function in the negative pressure range using the Van Genuchten method described in Section 2.1.2. In this calculation, the saturated permeability obtained from the third test series is utilized, k_s = 1.6x10^{-7} m/s (see Table H-3). The SWCC from the second series in Figure 6-4 is also chosen for the calculation. Figure 6-5 A shows the results for the hydraulic conductivity as function of the matric suction and the volumetric water content. As shown, the hydraulic conductivity of the soil decreases sharply with an increase in matric suction.

In addition, the hydraulic conductivity for this fine sand can be plotted against its volumetric water content in Figure 6-5 B using the Green and Corey (1971) equation. In this equation, it is assumed that the soil has a random distribution of pores of various sizes and an incompressible soil structure. In addition, the pores are assumed to be interconnected. A complete overview of this function is given by Fredlund and Rahardjo (1993). From the plot of Figure 6-5 B, one may observe that the hydraulic conductivity decreases sharply with a decrease in volumetric water content.

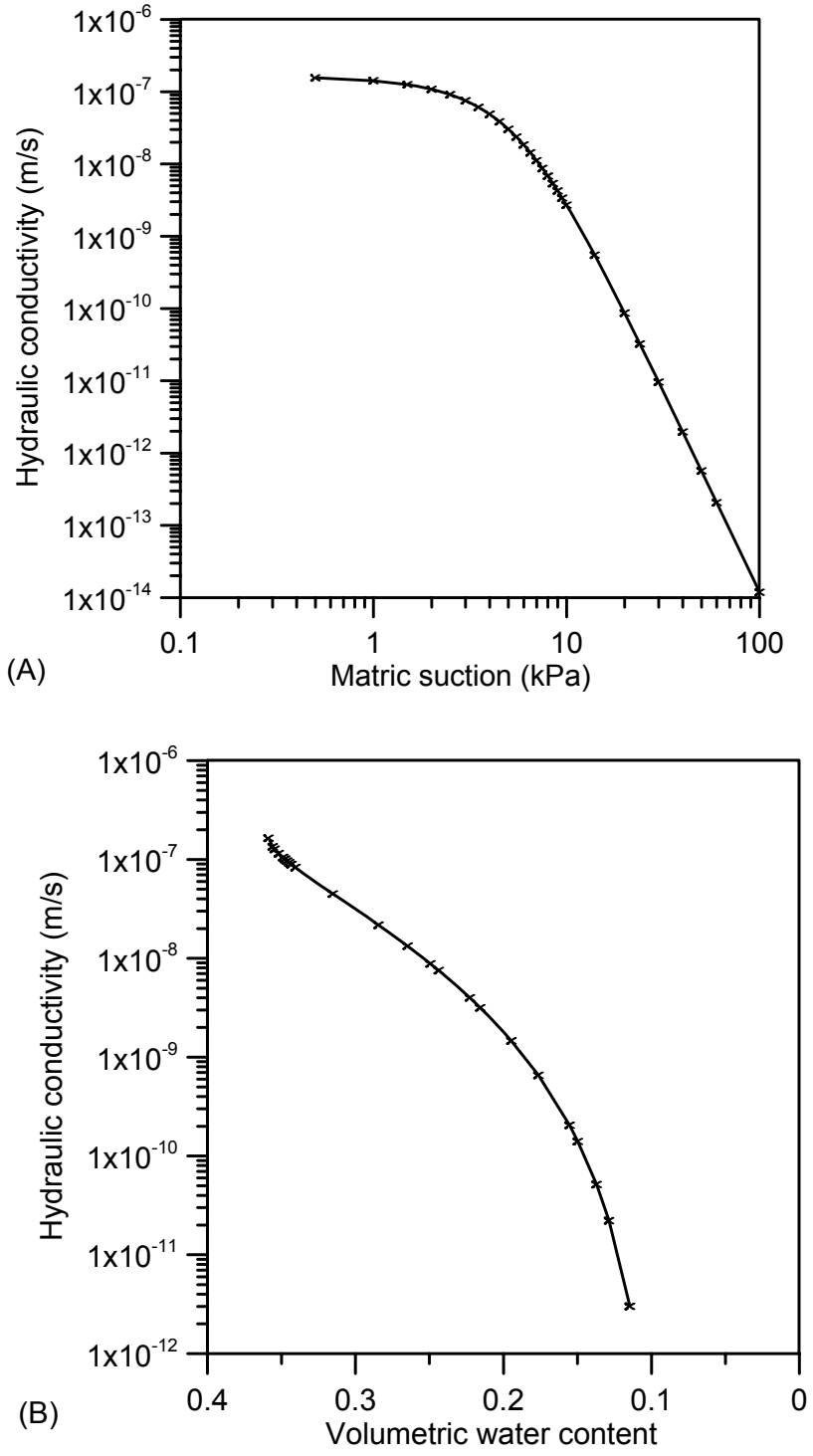

Figure 6-5: (A) Results for hydraulic conductivity versus matric suction and (B) results for hydraulic conductivity versus volumetric water content.

6.4 Back Calculation of the Failure in Åmot

Since no external loads were applied on the slope prior to failure, it will be assumed that the triggering mechanism is entirely related to an increase in pore-water pressure and/or to loss of matric suction due to the rainfall. In order to understand how the failure of this slope was triggered, a seepage analysis was conducted with the SEEP/W software from GEOSLOPE described in Chapter 3. This will help studying how the pore pressure distribution changed in the Åmot slope during the fall of 2000, using the results from the site and laboratory investigations. With the help of the SLOPE/W software, the changes in the stability (safety factor) of the slope can be investigated for this time period.

6.4.1 Slope seepage modelling

The Norwegian Meteorological Institute runs a meteorological station in the community of Fossum ca. 8 km north-west of Åmot. At this station, monthly normal and extreme rainfalls are calculated. It will be assumed in this analysis that the rainfall pattern in Fossum is the same as in Åmot. The monthly normal quantities of rainfall are shown on Figure 6-6 together with the rainfall from the extreme year of 2000 and the monthly temperature values. It can be seen on this figure that the rainfall pattern in 2000 followed the normal conditions from January to August. The month of September was particularly dry in 2000 and was followed by an extremely wet period from October to the end of November. In the year 2000, the month of October presented a total rainfall of nearly 195 mm and the month of November 275 mm. These values are between 2.5 and 4.5 times the normal values. Annually, the normal total of rainfall for this site is in the order of 705 mm. During the year 2000, the amount of rainfall was more than 975 mm.

Geometry and soil properties

The geometry of the Åmot slope is presented in Figure 6-7 together with the finite element mesh. The modelled profile is 220m long. This includes nearly 100m of the sand terrace lying behind to the slope crest and 50m beyond the foot of the slope to the Drammen River. The slope angle is 38 degrees. The hydraulic characteristics of the top sandy material are presented in Section 6.3. The hydraulic conductivity is shown in Figure 6-5, and the SWCC results from the second laboratory series, shown in Figure 6-4, are assumed for this soil. In addition, the

underlying clay material is assumed to have a saturated volumetric water content of 0.8 and a saturated water coefficient of hydraulic conductivity in the order of 10^{-9}m/s.

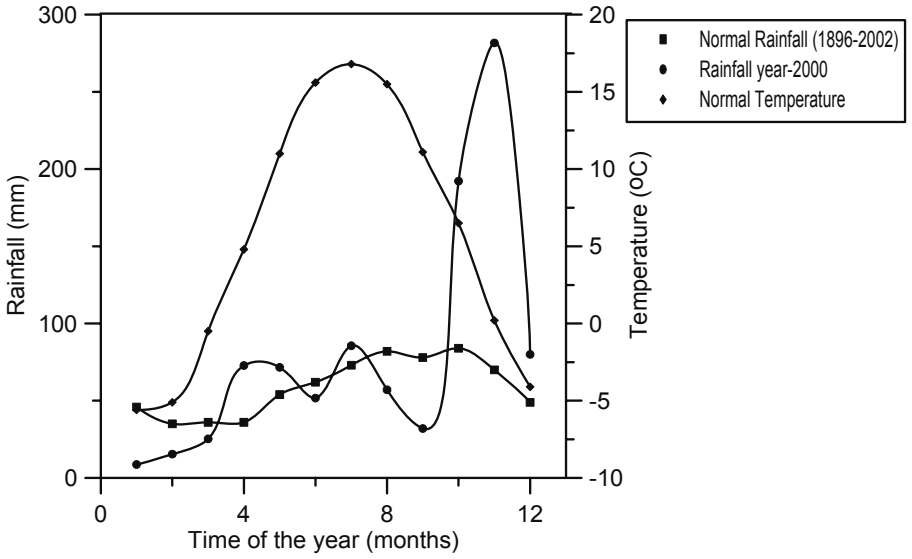

Figure 6-6: Rainfall values in Åmot during the year 2000 compared to normal values (Courtesy of the Meteorological Institute of Norway).

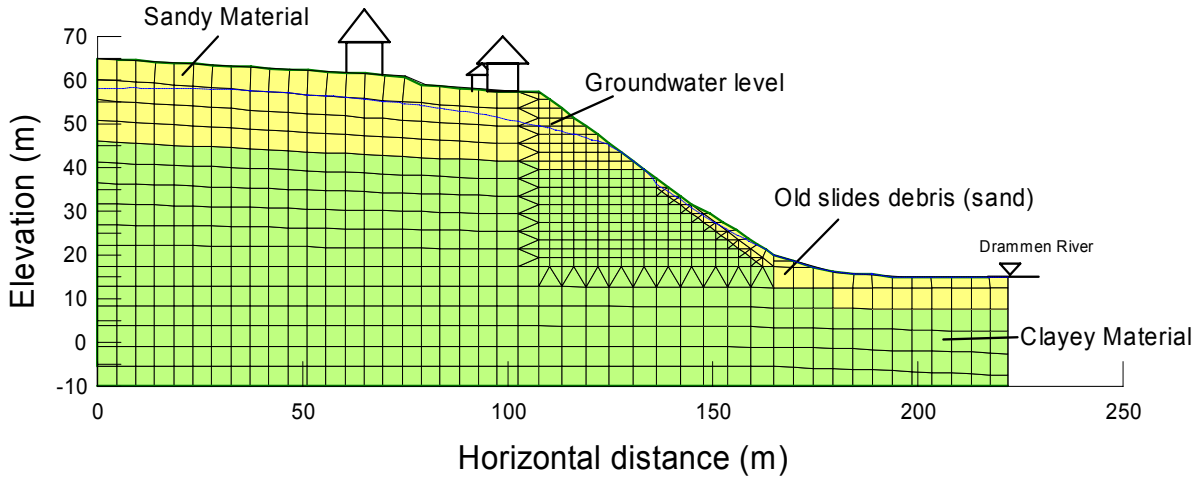

Figure 6-7: Finite element mesh model for the Åmot slope showing boundary and initial conditions.

Steady-state and normal conditions

Many parameters are affecting the establishment of steady-state or normal groundwater conditions in a slope. The infiltration in a soil is dependent upon the amount of rainfall, runoff, evaporation due to solar radiation and transpiration due to plants as illustrated in Figure 6-8. It is difficult to correctly estimate every one of these parameters. On a normal basis, evapotranspiration in the lowlands of Norway is in the order of 300-400 mm/year (Høydal 2003). This value depends largely on the infiltration capacity of the soil.

The Norwegian Water Resources and Energy Directorate (NVE) estimates the specific runoff for the Modum area to be in the order of 8 l/s/km^2. This corresponds to approximately 260 mm/year of runoff and represents nearly 37% of the rainfall. In this case study, it will be assumed that 40% of the rainfall goes to runoff. This amount of infiltration will be reduced by 10% on the steep slope.

For normal conditions, it will be assumed that no infiltration takes places during the months having a negative air temperature due to frozen ground. To calculate the normal yearly infiltration, a value of 300 mm of evapotranspiration will be assumed for the whole period with positive air temperature. This is a rough assumption taking into account that not much evaporation, due to solar radiation, takes place in the dark winter months in Norway. The normal yearly infiltration can then be calculated by:

$$\text{Infiltration} = R - E - RF$$

where:
I = infiltration
R = rainfall during the months having positive air temperature
E = evapotranspiration (300 mm for the whole period having positive air temperature)
RF= runoff calculated as 40% of available water for infiltration.

To calculate the annual normal groundwater profile in the slope, a steady state analysis is performed. The annual average infiltration, as calculated above, will be taken as the boundary flux in this system. An infiltration flux of 143 mm/year was calculated for the plateau of the slope and a flux of 129 mm/year is used along the slope. The left vertical boundary of the model is considered as a no-flux boundary in Figure 6-7. This means that no water flow is allowed across this line. This is a good estimate for the Åmot slope since there seems to be a

drainage divide in the middle of the sand terrace. From the middle of the sand terrace, the water seems to be flowing towards a little river some 300-400 m northwest of the crest of the slope. This river is small and therefore difficult to see on Figure 6-1. The bottom horizontal boundary of the model is considered to be impermeable. The depth of the Drammen River at the right vertical boundary of the model is nearly 15m. This is taken as a head boundary condition.

Numerical analyses using the estimated annual infiltration fluxes led to the normal groundwater conditions presented in Figure 6-7. The groundwater level in the model lies approximately 5 m under the surface plateau. Under the crest of the slope, the phreatic surface plunges to meet the sand-clay boundary (x=130, y=45). Bellow this point the slope is mainly saturated and the phreatic line follows the slope until it reaches the Drammen River.

These steady-state normal groundwater conditions are in agreement with the geophysical results and the pore-water pressure measurements made by the NGI. The depth of the groundwater level on the plateau is nearly the same as that observed with the resistivity measurements. The computed groundwater level is high in the slope which agrees with the fact that the soil is so wet at the surface of the slope (Figure 6-2). This is also in agreement with the high water content measured in-situ along the slope as illustrated in Figure C-1 (Appendix C).

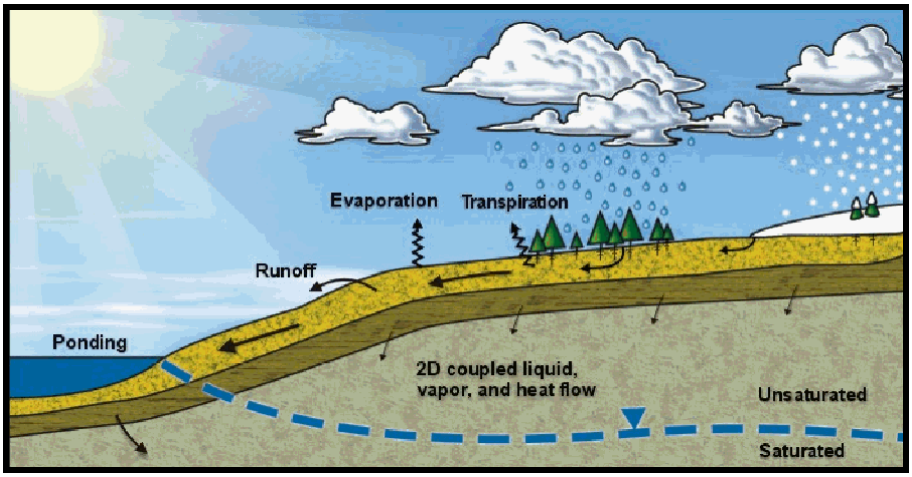

Figure 6-8: Physical processes related to seepage in a slope (from GeoSlope Inc.).

Fall of 2000

During the fall of 2000, the long lasting and high intensity rainfall led to failure of the slope in Åmot. To calculate how the pore pressure and the suction distribution were affected within the slope during this extreme rainfall, transient analyses are used. The normal groundwater condition is taken as an input, or initial condition, in this transient calculation. The calculation starts at the beginning of September and runs until the end of November. In order to calculate the amount of infiltration into the slope, it will be assumed that no evapotranspiration takes place during the rainfall event. This assumption is acceptable during a rainy period. The amount of runoff is assumed to be 40% of the rainfall. Again, the infiltration flux is considered 10% smaller along the steep slope due to runoff.

The variation in the groundwater level during the fall of a normal year and the fall of 2000 is presented in Figure 6-9 and Figure 6-10, respectively. The changes in the groundwater level are difficult to see on these figures due to the scale. Pore-water pressure profiles are taken at locations “A” and “B” during the rainfall simulations. The pore pressure changes at position “A” during the fall of a normal year and the fall of 2000 are presented in Figure 6-11 while the pore pressure at position “B” are presented in Figure 6-12.

From Figure 6-11 and 6-12 it is observed that the variations in pore pressures are more important during the fall of 2000. Results in Figure 6-11 suggest that the suction at the top of the slope varies from -16 to -10 kPa during the fall of a normal year. At the same location, the changes in negative pore pressures in the fall of 2000 are twice as large (from -16 to -5 kPa). However, the top of the slope is not fully saturated after the extreme rainfall of November 2000. At location “A”, the groundwater level rises 1 m from the beginning of September to the end of the fall 2000. This is approximately twice as in the normal year. This is observed by looking at the zero matric suction point on the profiles of Figure 6-11.

The changes in negative pore pressures are more important at position B where the clay/sand boundary is located. At this location, as illustrated in Figure 6-12, the matric suction changes from -13 to -6 kPa at the surface of the soil for the normal conditions. In the fall of 2000, the suction changes from -13 to 0 kPa. At position “B”, the groundwater level rises 1.5 m from September to the end of November 2000. This is 1 m more than for a normal year.

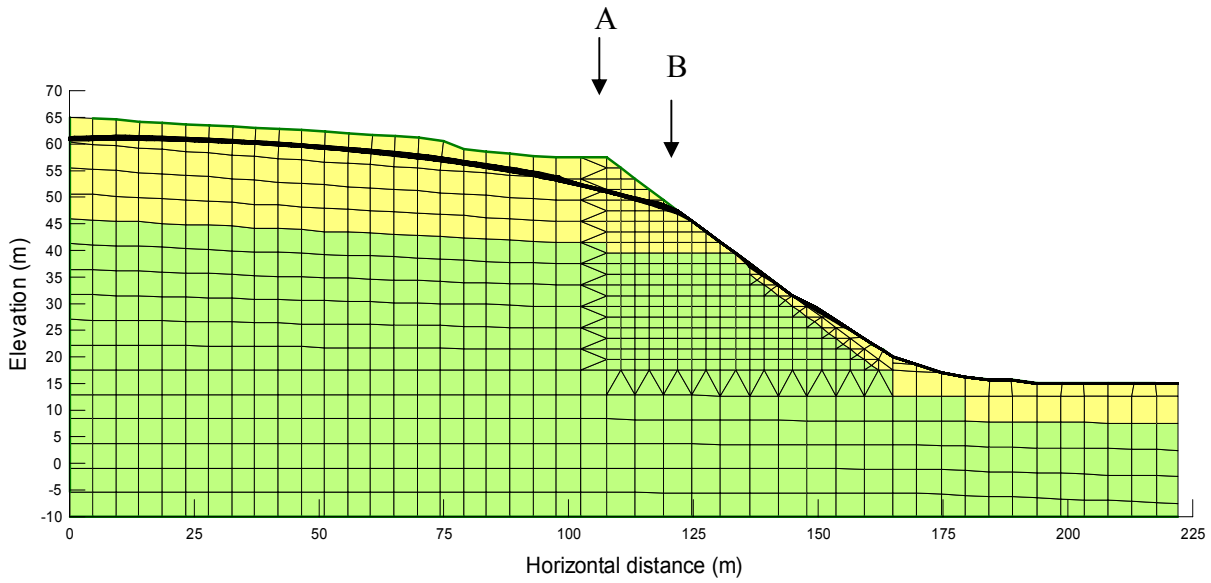

Figure 6-9: Variation in the groundwater level during the fall of a normal year.

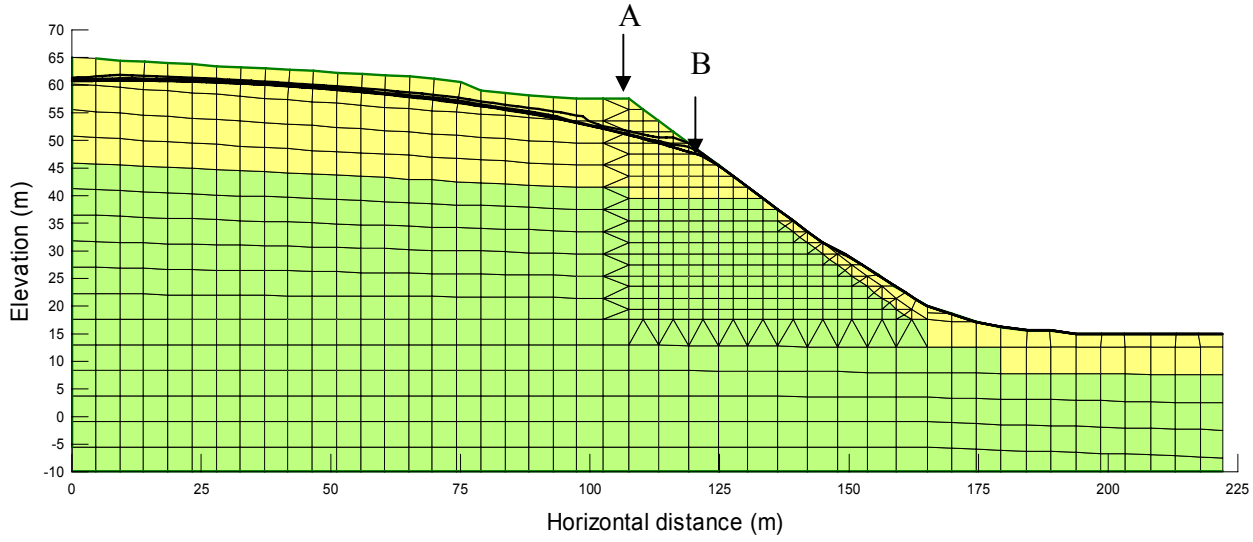

Figure 6-10: Variation in the groundwater level during the fall of year 2000.

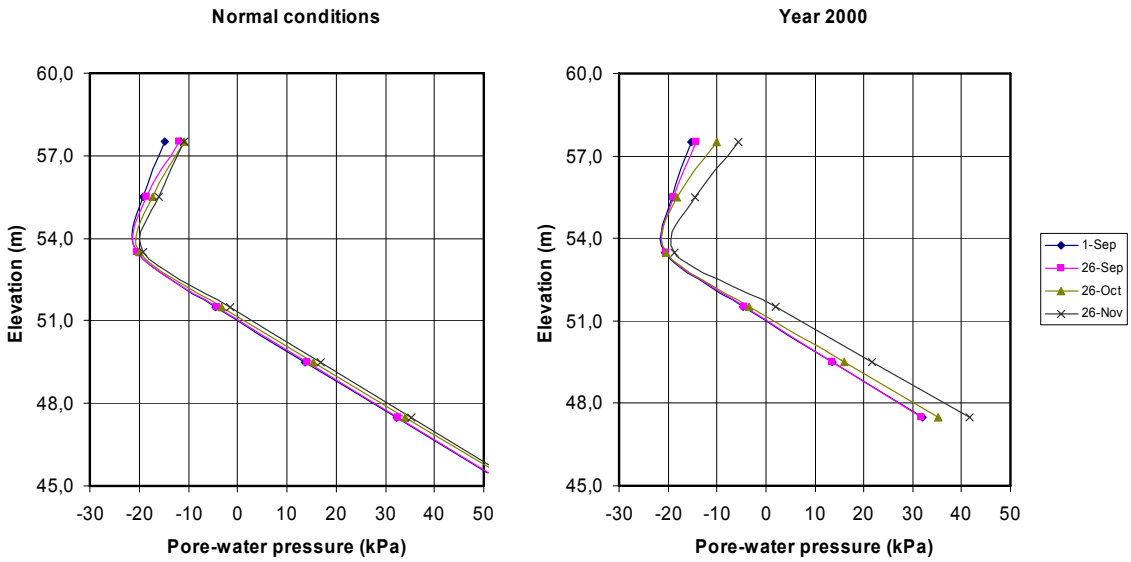

Figure 6-11: Pore pressure profiles at cross section A for normal conditions and for the fall of 2000.

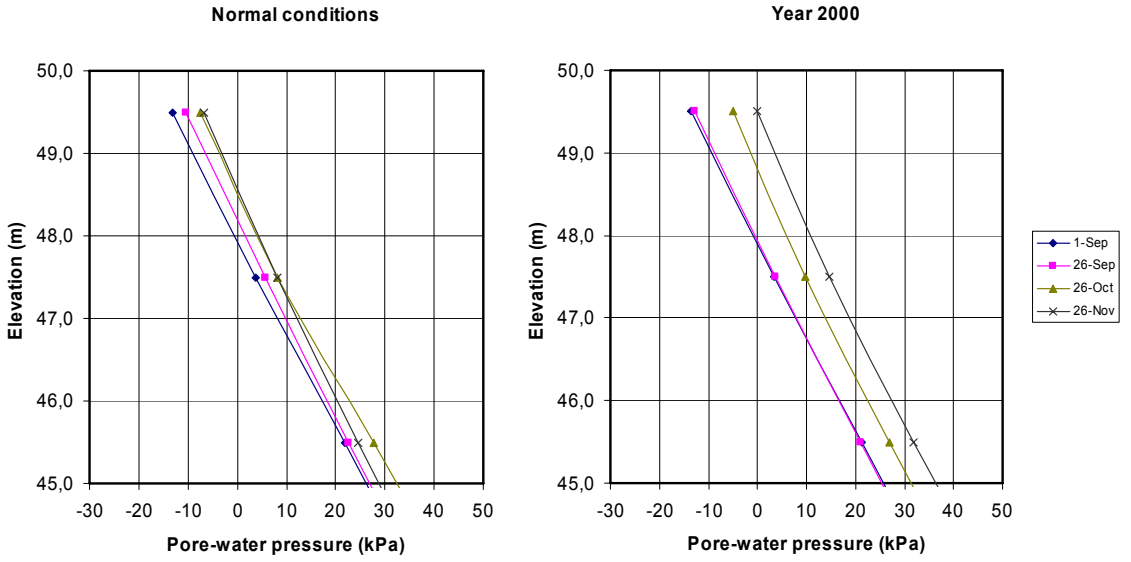

Figure 6-12: Pore pressure profiles at cross section B for normal conditions and for the fall of 2000.

6.4.2 Slope stability analysis

The changes in pore pressure within the Åmot slope, during the fall of 2000 (Section 6.4.1), are taken as input at their respective times steps to study the variation in stability through the fall months of 2000. The results will be compared to the changes in stability during a normal year. The shear strength parameters for the sand in the calculation are taken from the NGI Report No. 20001533-5. In this report, the effective friction angle for the sand is taken as $\varphi'= 35°$, the effective cohesion $c'=7$ kPa and the unit weight of the sand is $\gamma=19$ kN/m^3. For the present simulations, it will be assumed that the value of the φ^b angle lies between φ' and $\varphi'/2$ (see Equation 2-23).

Bishop's modified method of slices is utilised to calculate the change in the factor of safety with time. This method assumes a circular slip surface and satisfies vertical and overall moment equilibrium. The failure which took place in late November 2000 was mainly a shallow one. The depth to the slip surface is approximately 5 m. Having these indications, a fully specified slip surface is defined in the stability calculation. It is assumed that the failure took place entirely in the sandy material. The failure surface is presented in Figure 6-13. That failure surface gives a calculated factor of safety of 0.98 on the 20th of November 2000, calculated with $\varphi^b/\varphi'=1$. This indicates instability since the safety factor is below unity.

The changes in factor of safety with time are presented in Figure 6-14 for a normal year and year 2000 conditions. As seen from this figure, during normal rainfall conditions, the factor of safety changes with time due to the rainfall pattern from 1.12 to 1.06 for $\varphi^b/\varphi'=1$ and from 1.07 to 1.02 for $\varphi^b/\varphi'=1/2$. For normal conditions, the safety factor of the slope is the lowest at the end of October. This is consistent with the amount of rainfall which is normally higher in the month of October (Figure 6-6).

During the fall of 2000, the safety factor of the slope is higher than in the normal year until the 15th of October. This is due to a drier than normal month of September in 2000. After the middle of October, the rainfall intensity increases. This results in lower suction and a higher groundwater level in the soil. From the 15th of October 2000, the factor of safety decreases gradually and, goes below 1 on the 1st of November for $\varphi^b/\varphi'=1/2$ and on the 20th of November for $\varphi^b/\varphi'=1$.

As seen on Figure 6-15, the failure of the slope can be related to a loss of frictional strength and suction strength (refer to Equation 2-23). The loss of frictional strength is due to an

increase in positive pore-water pressures at the bottom of the slip surface. The loss of suction strength is due to loss of the negative pore-water pressures at the top of the sand mass. These changes are relatively small but are still sufficient to trigger a landslide. Even under normal rainfall conditions, the safety factor was close to a value of 1. It was therefore a matter of time before an intense rainfall would perturb the equilibrium of this sandy slope.

The real failure in Åmot occurred on the 22nd of November 2000. By using a ratio $\varphi^b/\varphi'=1$ in the stability model, it is seen that failure occurs on the 20th of November. This is good agreement. However, one must consider the important assumptions in the analyses:

- The vegetation cover of the soil is ignored (both for seepage and stability analyses).
- The two types of soils are considered as homogenous.
- No hysteresis between drying and wetting of the soil.
- The runoff is approximated to 40% of the total rainfall.
- No evapotranspiration during the rainfall event.
- A no-flux boundary is assumed on the left side of the model slope.
- The monthly rainfall data are distributed on a daily basis.

The failure of the Åmot slope is a consequence of both intense and prolonged rainfall during the fall of 2000. By studying the rainfall pattern and the soil properties of the slope, one could have predicted the event of 2000 by using the methodology described in this thesis.

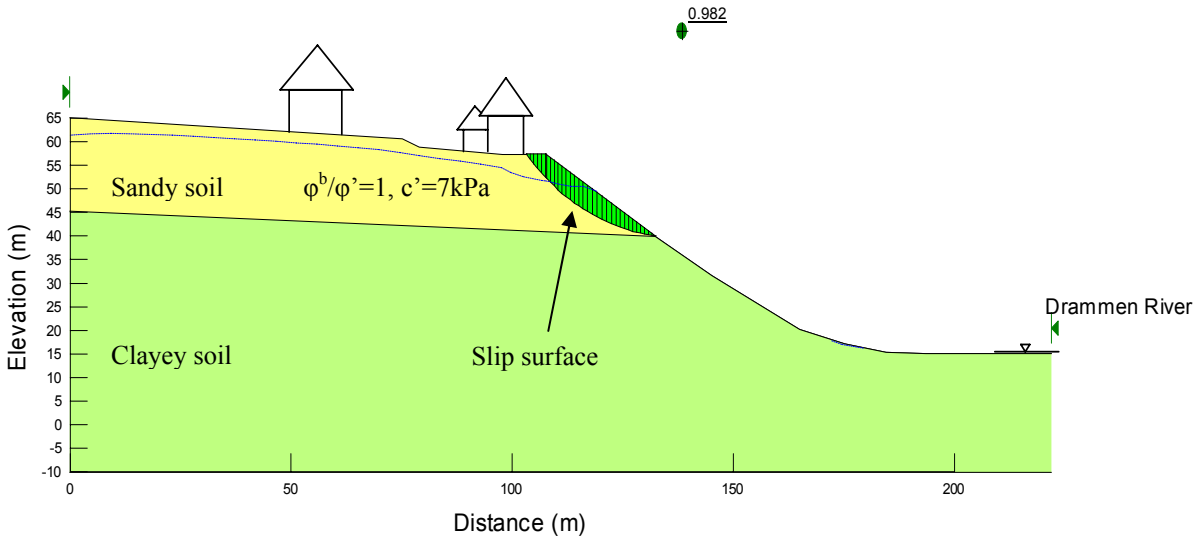

Figure 6-13: Computed factor of safety on the 20th of November 2000.

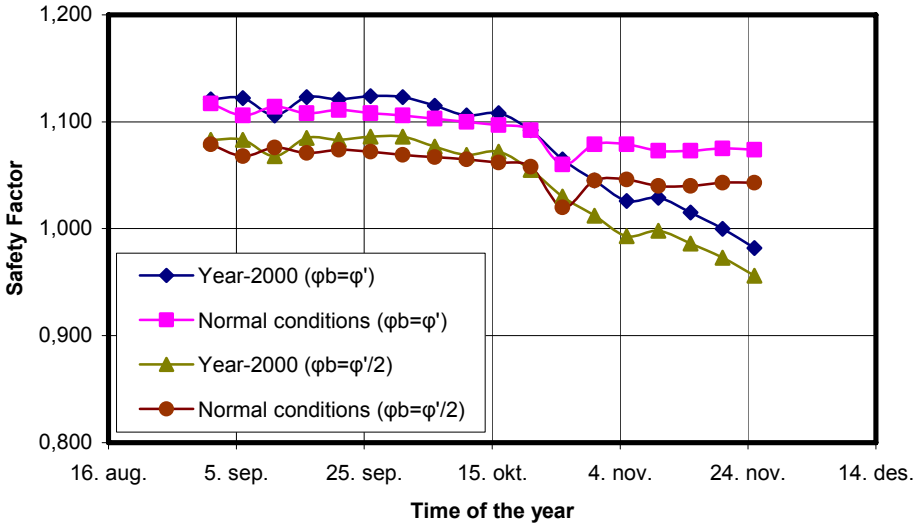

Figure 6-14: Changes in the factor of safety with time for the fall of 2000 and the normal fall conditions.

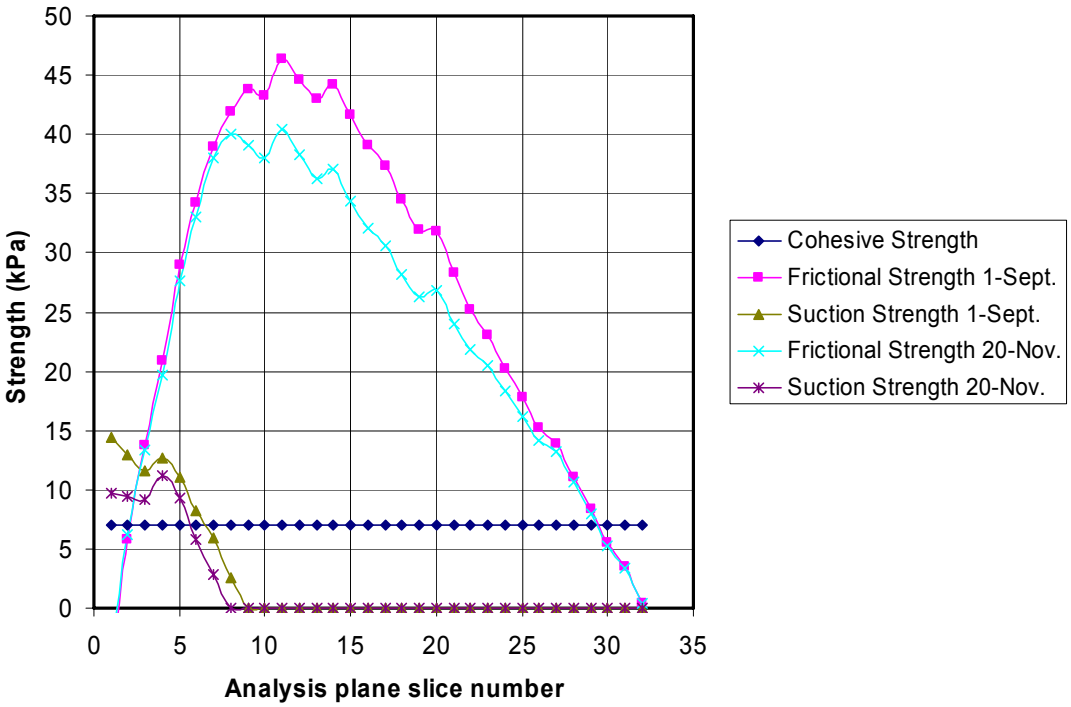

Figure 6-15: Change in suction, cohesion and frictional strength versus slice number for normal and year-2000 conditions (refer to Equation 2-23). Slice no. 1 is at top of slide, slice no. 32 at toe.

CHAPTER 7 Summary and Conclusion

Rain infiltration in an unsaturated slope causes reduction of suction and lowers the suction strength present in the soil. Many factors are influencing the stability of an unsaturated slope subjected to water infiltration. These can be external (climatic conditions, rainfall intensity, rainfall duration and rainfall pattern) or intrinsic (coefficient of permeability, water retention characteristics and strength properties).

2-D steady-state and transient parametric studies are performed in this thesis. The results are showing that the closer to unity the ratio of rate of infiltration to saturated permeability (q/k_s), the higher will be the rate of matric suction loss. This ratio being constant, the higher the saturated permeability of the soil, the higher the rate of matric suction loss. In addition, if a steady-state rainfall preceded the transient event, the soil will present a greater rate of suction loss.

Much attention must be given to the soil-water characteristic curve (SWCC) and to the coefficient of permeability of different soils. It is found that the air-entry value of a soil greatly affects its permeability function and consequently, its response to infiltration. For the same saturated coefficient of permeability, the higher the air-entry value of a soil, the faster will be the loss of matric suction when a soil is subjected to infiltration. The numerical results are showing that this parameter should rather be overestimated than underestimated when performing stability analyses. This overestimation will lead to a higher rate of loss of matric suction in the soil when subjected to infiltration. Consequently a lower factor of safety will be calculated with time and the analysis will be on the safe side.

Differences in hydraulic characteristics between a fine and coarse grain soil are studied in this thesis. The differences are mainly in the saturated coefficient of permeability, the air-entry value, the desaturation coefficient and the volumetric water content. Due to these hydraulic differences, a coarse soil may be more prone than a fine soil to developing a perched water table during the infiltration process.

Changes in pore water pressures in the slope are controlled by the hydraulic properties. These changes are occurring first at the toe of the slope due to lower initial suction and consequently a higher coefficient of permeability. For the coarse soil, the zero pore-water pressure surface

moves gradually upslope with time. In the fine grain soil model, the rate of suction loss is nearly the same at the toe, the middle and at the top of the slope. These different infiltration patterns are leading to different types of rupture. In the case of a coarse soil, rupture may initiate at the foot of the slope as a consequence of positive pore pressure build-up. The fine soil is more prone to loss of matric suction along its entire slope. In this case, the infiltration pattern may lead to translational type of shallow sliding. A change in the geometry of the slope had more effect on the pore pressure distribution in a coarse soil than in a fine grain soil.

The thesis analyses a field situation where a slide occurred in Åmot, Norway during the wet fall of 2000. Using the input from site investigations including geophysical methods, special laboratory tests to determine the soil-water characteristics (SWCC) and the coefficient of permeability, the author performed a numerical back-analysis of the slope failure.

The SWCC of the soil was determined in the laboratory using the Tempe Pressure Cell apparatus and the constant-head test was used to calculate the saturated coefficient of permeability of the soil. The geophysical investigations were carried out by the author on the Åmot slope during the summer of 2004. These investigations gave good information about the soil type and the groundwater conditions within the slope.

The rainfall conditions during a normal year and the wet fall of year 2000 were compared. The numerical infiltration and stability analyses showed that the slope is predicted to be stable under normal rainfall condition, but fails when subjected to the rainfall conditions of the year 2000. The calculations are showing that the failure is due to a lowering of the suction and frictional strength during the intense rainfall. The calculated time to failure is in agreement with the observed event and shows that the event could have been predicted.

References

Arya, L.M., and Paris, J.F. 1981. A physicoempirical model to predict the soil moisture characteristic from particle-size distribution and bulk density data. *Soil Science Society of America J.*, Vol. 45, pp 1023-1030.

Aubertin, M., Mbonimpa, M., Bussière, B. and Chapuis, R.P. 2003. A model to predict the water retention curve from basic geotechnical properties. *Canadian Geotechnical J.*, 40(6), pp. 1104-1122.

Chen, H., Lee, C.F., Law, K.T. 2004. Causative Mechanisms of Rainfall-Induced Fill Slope Failures, *J. of Geotechnical and Geoenvironmental Engineering,* Vol. 130, No. 6, pp. 593-602.

Collins, B. D., and Znidarcic, D. (2004). Stability analyses of rainfall induced landslides, *J. of Geotechnical and Geoenvironmental Engineering*, Vol. 103, No. 4, pp. 362-372.

Donald, I.B. 1956. Shear strength measurements in unsaturated non-cohesive soils with negative pore pressures. *Proc. 2nd Australia-New Zealand Conf. Soil Mech. and Found. Eng.*, Christchurch, pp. 200-205.

Edgers, L. 2003. "Unsaturated soils and rain-induced slides – Effect of infiltration on pore pressures and stability". *NGI Report No. 20031087-2*, Norwegian Geotechnical Institute.

Fortier, R. 2003. *Document sur les methodes géophysiques*, Notes de Cours: GGL-10347 Géophysique Appliquée, Département de Géologie et de Génie Géologique, Université Laval, pp. 285.

Fredlund, D.G., Morgenstern, N.R. and Widger, R.A. 1978. The shear strength of unsaturated soils. *Canadian Geotechnical J.,* 15(3): 313-321.

Fredlund, D.G. and Rahardjo, H. 1993. *Soil Mechanics for Unsaturated Soils*. John Wiley and Sons, Inc., pp. 517.

Fredlund, D.G. and Xing, A. 1994. Equation for the soil-water characteristic curve. *Canadian Geotechnical J.*, 31: 521-532.

Fredlund, D.G., Vanapalli, S.K., Xing, A. and Pufahl, D.E. 1995. Predicting the shear strength function for unsaturated soils using the soil-water characteristic curve. Proc. *1st Int. Conf. on Unsaturated Soil*, Paris, Vol. 1: 63-69.

Fredlund, D.G, Xing, A., Fredlund, M.D. and Barbour, S.L. 1996. The relationship of the unsaturated soil shears strength to the soil-water characteristic curve. *Canadian Geotechnical J.,* 33(3): 440-448.

GEOMETRICS INC., OhmMapper Operation Manual, Copyright © November 2001.

GEOTOMO SOFTWARE 2004, RES2DINV version 3.54, Geoelectrical Imaging 2 & 3-D, www.geoelectrical.com, pp.129.

Hillel, D. 1998. *Environmental soil physics*, Academic, New York. pp. 757.

Høydal, Ø.A. 2003. "Unsaturated soils and rain-induced slides – Methodology for calculation of rain-induced landslides". *NGI Report No. 20031087-3*, Norwegian Geotechnical Institute.

Krahn, J. 2004. *Seepage Modelling with SEEP/W - An engineering methodology,* First Edition, Copyright by Geo-Slope International Ltd., pp. 412.

Krahn, J. 2004. *Stability Modelling with SLOPE/W - An engineering methodology,* First Edition, Copyright by Geo-Slope International Ltd., pp. 406.

Krahn, J. 2004. *Vadose Zone Modelling with VADOSE/W - An engineering methodology,* First Edition, Copyright by Geo-Slope International Ltd., pp. 432.

Lam, L., Fredlund, D.G. and Barbour, S. L. 1988. Transient seepage model for saturated-unsaturated soil systems: A Geotechnical Engineering Approach. *Canadian Geotechnical J.,* 24(4): 565-580.

Lambe, W.T., Withman, R.V. 1979. *Soil Mechanics. SI Version*. John Wiley & Sons. New York-Chichester-Brisbane-Toronto-Singapore. pp. 553.

Leroueil, S., and Hight, D. 2003. Characterisation and Engineering Properties of Natural Soils: *Proceedings of the International Workshop, Singapore, 2-4 December 2002*. pp. 170-192.

Ng, C. W. W., and Shi, Q. 1998. A numerical investigation of the stability of unsaturated soil slopes subjected to transient seepage, *Computers and Geotechnics*, Vol. 22, No. 1, 1-28.

Rahardjo, H., Li, X.W., Toll, D.G. and Leong, E.C. 2001, The effect of antecedent rainfall on slope stability, *Geotechnical and Geological Engineering*, Vol. 19, No. ¾, pp. 371-399.

REFLEXW, Version 3.0, 9x/NT-program for the processing of seismic, acoustic or electromagnetic reflection, refraction and transmission data, Copyright 1998-2003.

SEEP/W, Version 5.17. Geo-Slope International Ltd., Copyright © 1991-2005.

Senechal, P., Perroud, H. and Garambois, S. 2000, Geometrical and physical parameters comparison between GPR data and other geophysical data, *8th International Conference on Ground Penetrating Radar*, Australia, 2000.

SLOPE/W, Version 5.17. Geo-Slope International Ltd., Copyright © 1991-2005.

Soil Moisture Equipment Corp., Operating Instruction: Tempe Pressure Cell 1400/1405, Santa Barbara, California, www.soilmoisture.com, June1995.

Sillers, W.S, Fredlund, D.G. and Zakerzadeh, N. 2001. Mathematical attributes of some soil-water characteristic curve models, *Geotechnical and Geological Engineering J.*, 19: 243-283.

Tami, D., Rahardjo, H. and Leong, E. 2004. Effects of Hysteresis on Steady-State Infiltration in Unsaturated Slopes, *J. of Geotechnical and Geoenvironmental Engineering*, Vol. 130, No. 9, pp. 956-966.

Topp, G. C., Davis, J. L. and Annan, A. P. 1980. Electromagnetic determination of soil water content: Measurements in coaxial transmission lines, *Water Resources. Res.* 16(1), 574-588.

Tsaparas, I., Rahardjo, H., Toll, D.G., Leong, E.C. 2002. Controlling parameters for rainfall-induced landslides, *Computers and Geotechnics*, Vol. 29: 1-27.

Tsaparas, I., Rahardjo, H., Toll, D.G., and Leong, E. C. (2003). Infiltration characteristics of two instrumented residual soil slopes, *NRC Research Press Web site at http://www.cgj.nrc.ca* on 30 September 2003.

Vanapalli, S.K, Sillers, W.S., and Fredlund, M.D. 1998, The meaning and relevance of residual state to unsaturated soils, *Proc. 51st Canadian Geotechnical Conf., Edmonton.*

APPENDICES

APPENDIX A Typical Values for the SWCC *a*, *m* and *n* Parameters

Table A-1: Typical values for the *a*, *m* and *n* parameters describing the SWCC.

Material	a	n	m	Source
Uniform fine sand #1	2,0	4,36	0,32	1
Uniform fine sand #2	1,0	1,87	0,87	
Sandy loam	7,0	9,00	0,63	
Very fine sand	5,0	6,56	1,23	
Sandy silt (Coarse Tailings)	17,5	5,33	1,03	
Silty sand	20,0	4,50	1,08	
Well-graded #1	50,0	3,22	0,58	
Well-graded #2	148,0	4,48	1,06	
Silt #2	28,0	4,40	1,41	
Glacial till (uncompacted)	28,0	4,16	0,82	
Silt loam	50,0	2,79	1,74	
Sandy silty clay	115,0	3,83	0,94	
Silty clay (Fine tails)	55,0	2,79	0,64	
Uniform silt	105,0	5,49	0,74	
Clay/Silt	11,0	1,63	0,30	
Well graded #3 (high clay)	50,0	0,50	0,69	
Uniform sand	7,0	2,50	1,23	
Sand	8,0	2,40	2,02	
Fine sand	6,0	2,23	1,09	
Silt	22,0	4,69	0,99	
Silt (tailings)	11,0	3,97	0,45	

Sandy clayey silt	30,0	2,63	1,38	
Clayey silt	36,0	5,49	0,80	
Silty loam	67,3	7,32	0,50	2
Silty loam	87,0	8,09	0,59	
Till (σ_p=100 kPa)	427,0	0,61	2,62	
Till (σ_p=400 kPa)	127,2	17,35	0,05	
Kid Creek Tailings	248,0	1,63	1,19	
Sand	2,8	12,13	0,43	
Sand	1,0	2,53	1,53	
Sand	1,8	4,50	1,15	
Sand	19,0	4,16	1,20	
Silt	13,3	2,68	0,46	
Silt	2,0	2,71	1,08	
Slurried Regina Clay	15150,0	1,10	0,87	
Compacted Till	117,3	0,77	0,49	3
Decomposed Tuff (Hong Kong)	110,5	2,02	10,61	
Decomposed granite (Hong Kong)	3,0	2,40	0,35	4
Colluviums (Hong Kong)	0,1	2,20	0,25	
Fine Sand	1,9	6,30	0,87	5
Gravely Sand	0,2	4,44	1,13	

1- Seep/W library function

2- Fredlund and Xing (1994)

3- Fredlund, Vanapalli and Pufahl (1995)

4- Tami, Rahardjo and Leong (2004)

5- Fredlund and Rahardjo (1993)

APPENDIX B Finite Element Meshes (Different Geometries)

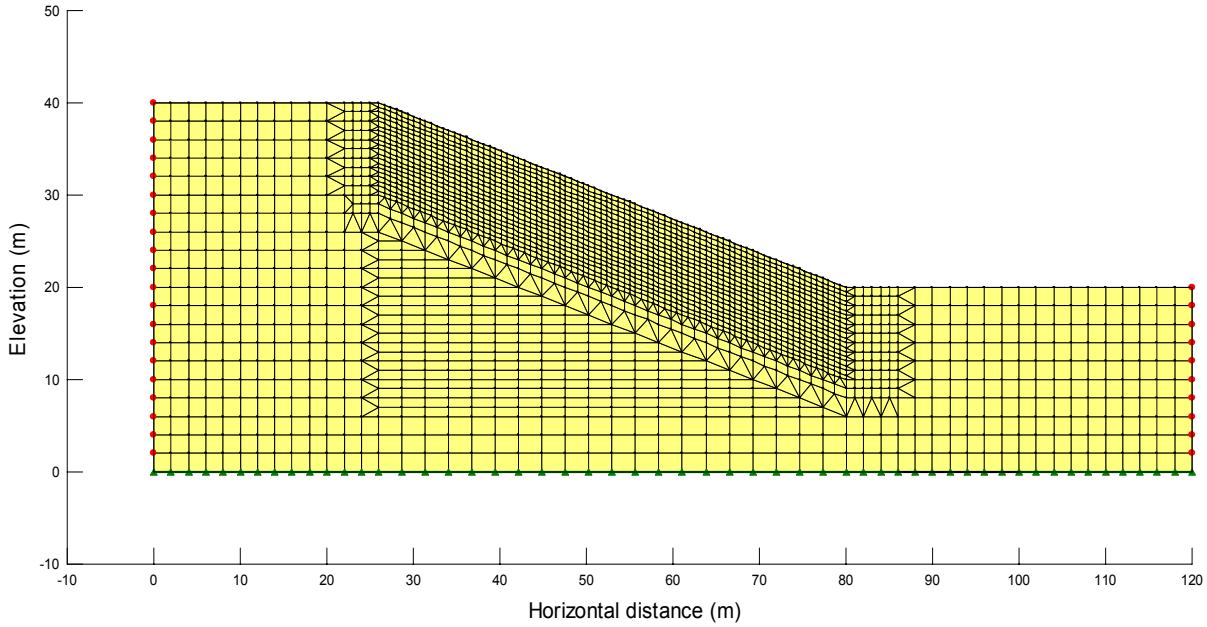

Figure B-1: Finite element mesh 20 degrees.

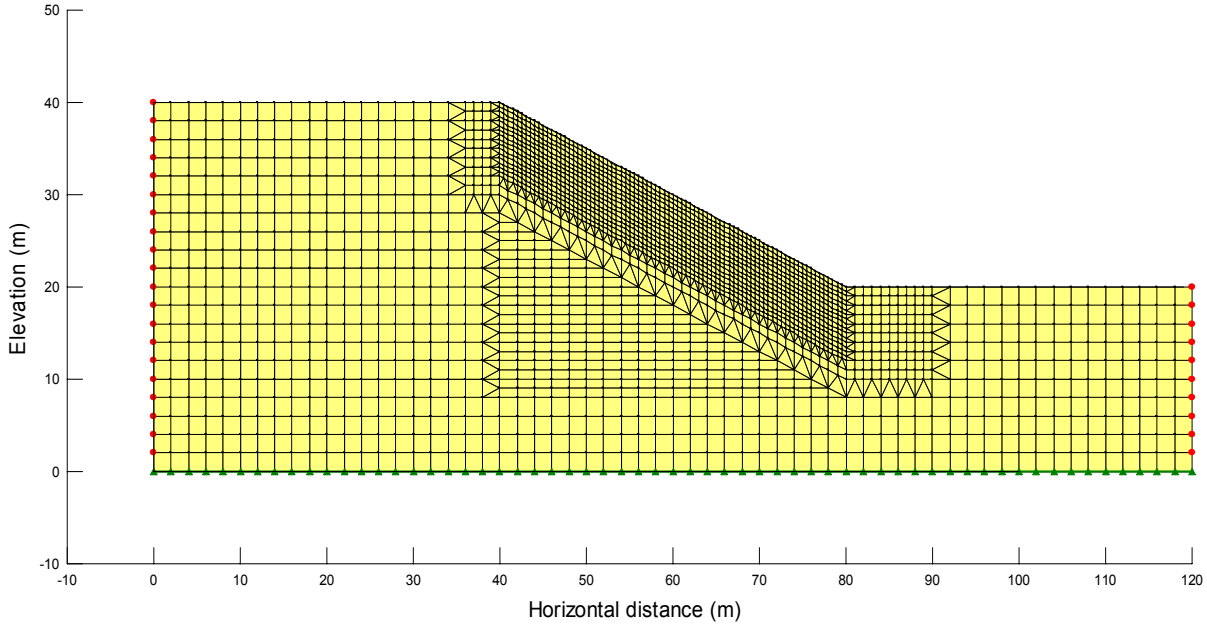

Figure B-2: Finite element mesh 26 degrees

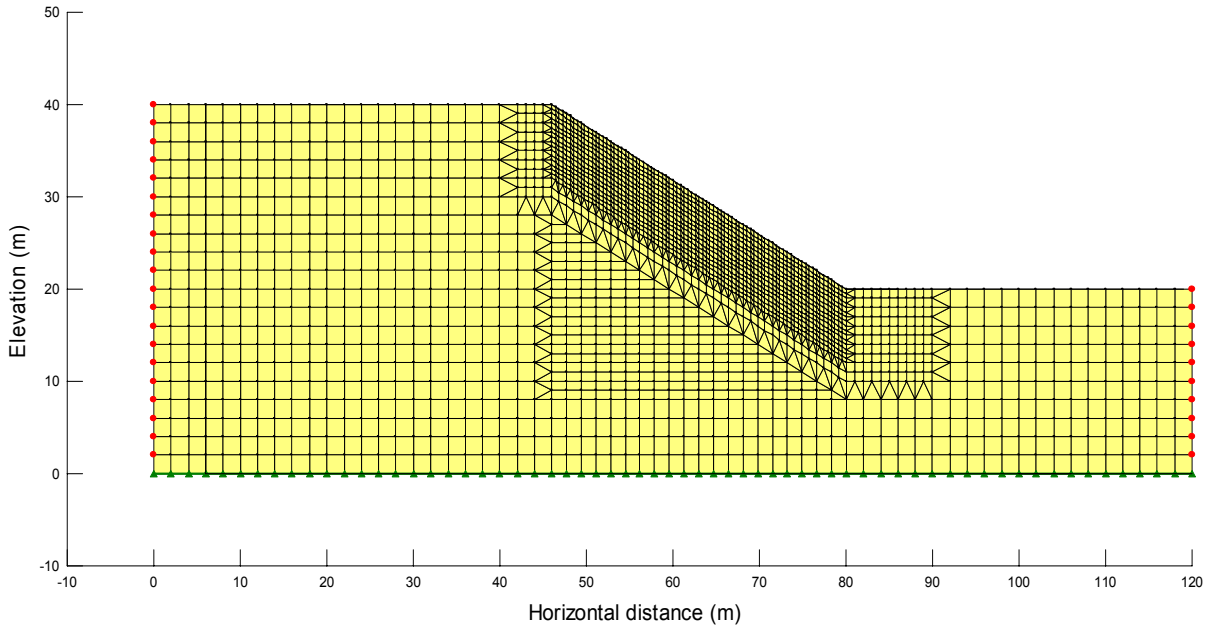

Figure B-3: Finite element mesh 30 degrees

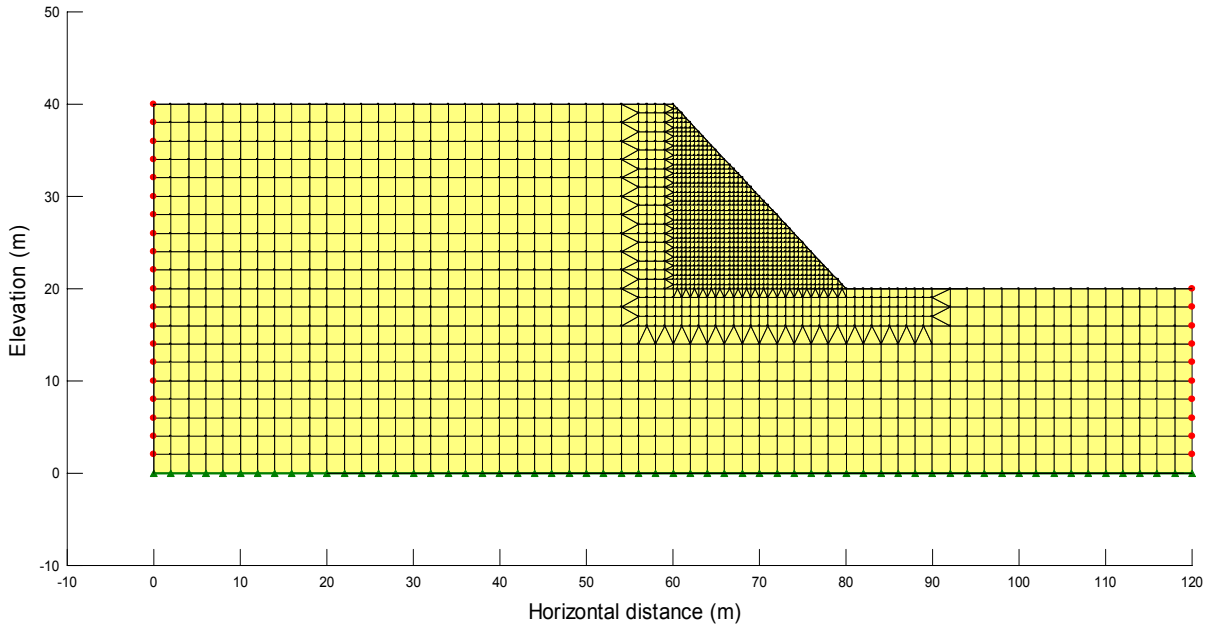

Figure B-4: Finite element mesh 45 degrees.

APPENDIX C The Åmot Slope

C.1 Location of Geophysical Profiles and in-situ measurements

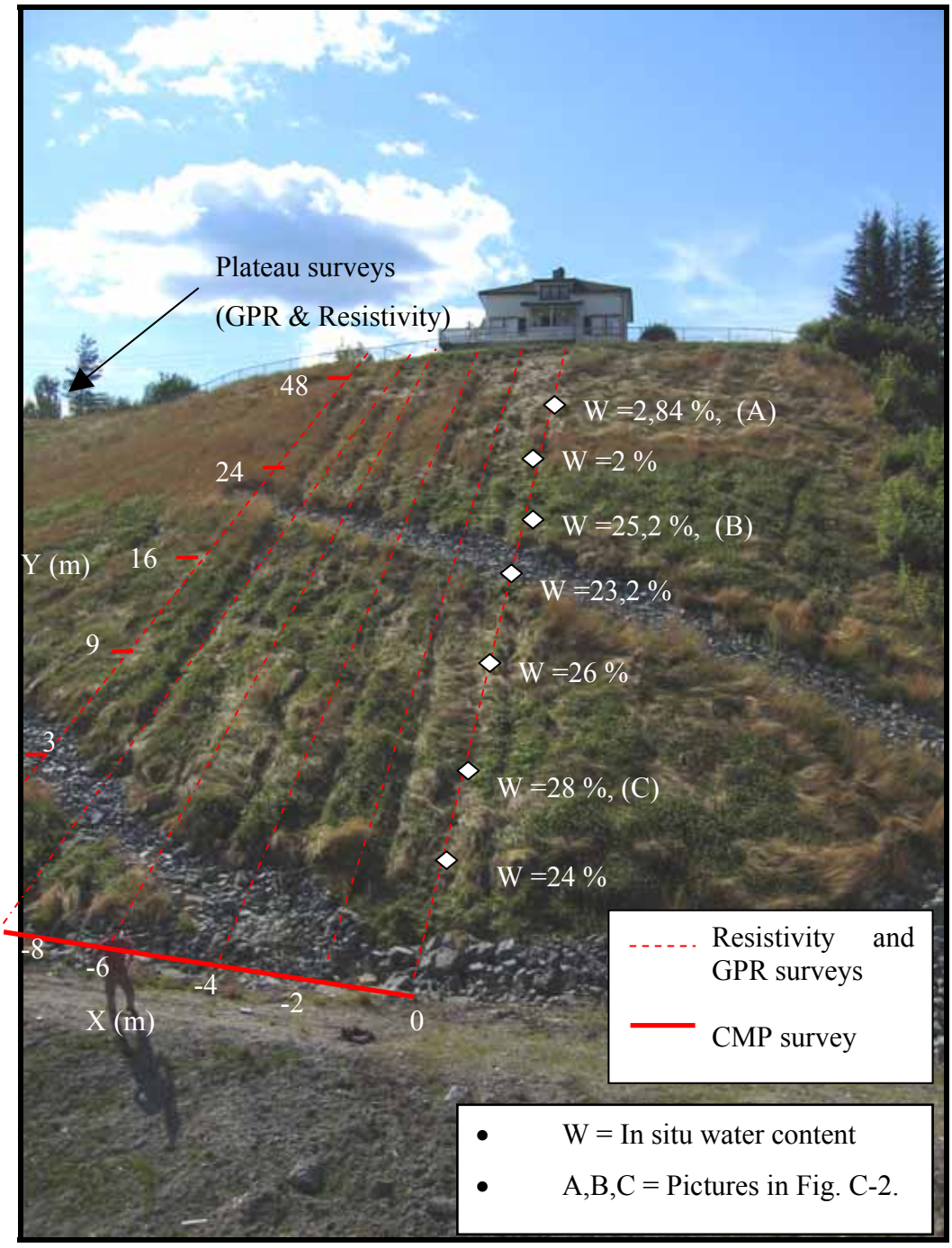

Figure C-1: Geophysical acquisition grid with water content measurements and dimension of the site. The slope is 48 m long and is lying at an angle of 2H:1V.

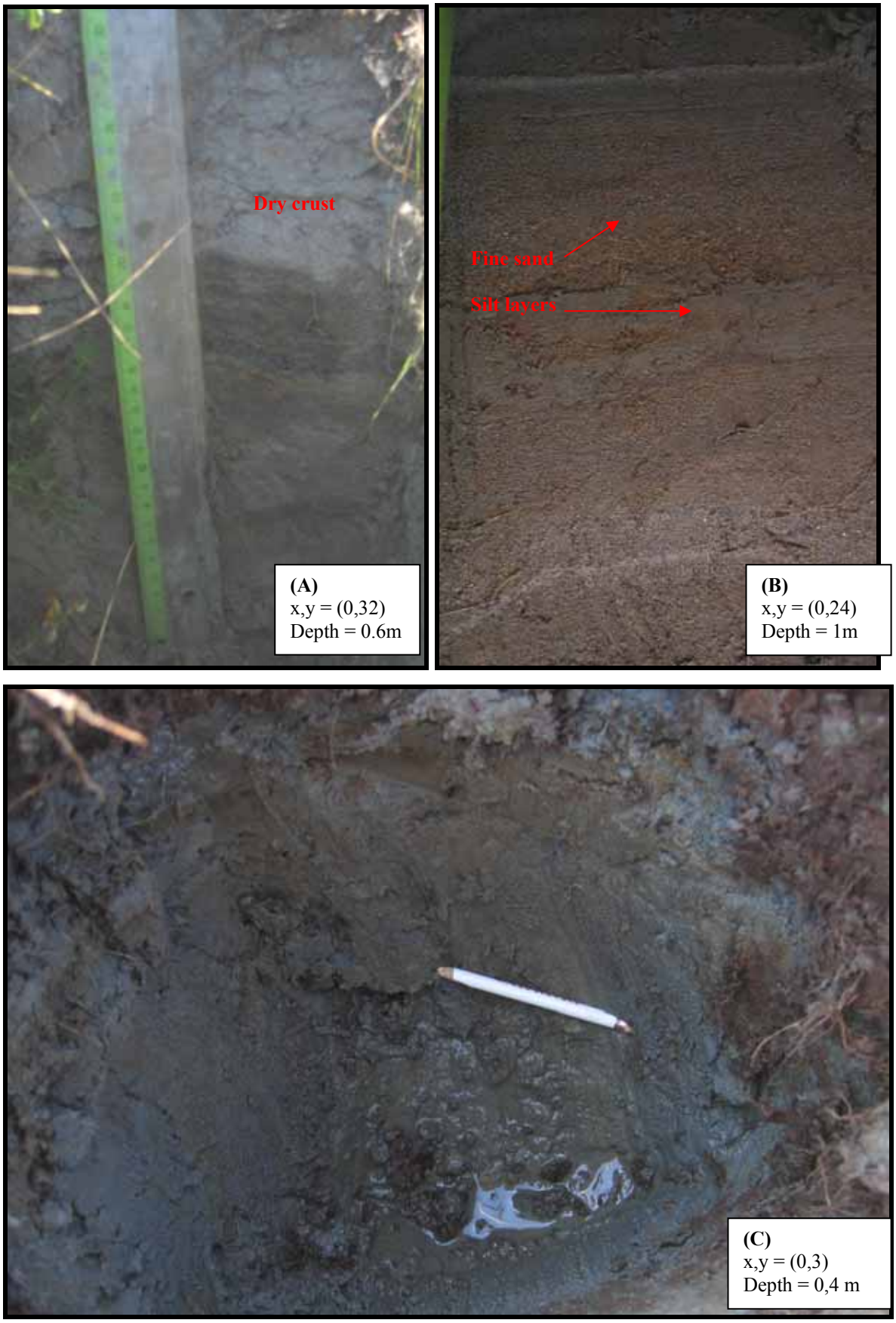

Figure C-2: Surface holes and soil characteristics at location A-C on profile X=0m.

APPENDIX D Ground Penetrating Radar

The ground penetrating radar (GPR) also called georadar is a non-destructive electromagnetic method. The instrument is presented in Figure D-1. This method permits a rapid profiling with high resolution of the subsurface structure. The GPR instrument constantly emits and receives high frequency electromagnetic signals as it is towed across the ground surface. The transmission frequency of the electromagnetic pulse depends on the type of antennae used during surveying. In this study, a 250 MHz shielded antennae was used to survey the slope. This antennae choice was a compromise between the penetration depth and the resolution. An important aspect to consider when preparing the survey is that radar energy transmission through clayey soils is really poor.

Changes in material type, density, porosity and water content produces contrasts in the electrical properties of the material. These contrasts are the cause of the reflected electromagnetic energy towards the surface. This reflected energy is detected by the receiver antennae. By recording the received energy and the propagation time from the emitting antennae through the soil and back to the receiver at different points along a survey line, a profile of the subsurface can be obtained. In order to transform the wave propagation time into a depth survey, knowledge of the wave velocity propagation is necessary.

D.1 Wave velocity propagation

Radar wave velocity is controlled by the relative permittivity (ε_r) of the material. The permittivity can be defined as the ability of the material to get electrically polarized. The electromagnetic wave velocity (V) is given by:

$$V = c \Big/ \sqrt{\varepsilon_r} \qquad \textbf{Equation D-1}$$

where c = 0.3 m/ns is the electromagnetic wave velocity in air.

Since the permittivity of water is 20 times larger than that of most geological materials, water is a dominant agent acting on the wave velocity propagation in a porous medium. Table 6-1, in the text, presents some electrical properties of common materials encountered in the field.

Knowing that the relative permittivity depends on the volume of water in the soil, Topp et al. (1980) developed an empirical equation relating the permittivity of the soil to its volumetric water content:

$$\varepsilon_r = 3.03 + 9.3\theta_v + 146\theta^2{}_v - 76.6\theta^3{}_v \qquad \textbf{Equation D-2}$$

This equation can be used to measure the in-situ volumetric water content along a survey when having a good definition of the wave velocity profile along this survey.

D.2 Survey modes

Two different types of survey method can be used with the ground penetrating radar. The first one, which is the most common, is called *reflexion survey*. For this method, the antenna separation is kept constant throughout the whole survey and they are moved at regular intervals to obtain a profile. Some important factors to consider in this method are the time window and the stack number in order to amplify the results and minimize the noise. The *time window* must be greater than 50% of the electromagnetic wave propagation time between the transmitting antennae to the target and back again from the target to the receiver antennae. This time window is a direct function of the wave velocity propagation and the depth of the receptor.

The second method, namely the common mid-point (CMP) survey, is used for evaluation of the electromagnetic wave propagation velocity in the soil. The way to conduct this survey is firstly to find a fixed mid-point at the surface of the soil. Thereafter, the two transmitting antennae are moved in opposite directions at equal intervals away from the common mid-point. After each interval, a trace is obtained and saved. By progressively increasing the distance between the antennae the reflector will gradually appear under the common mid point. The reflectors will be seen on traces having greater propagation time for every interval. Knowing the exact interval distance from the mid-point and the change in propagation time of the electromagnetic waves, the wave velocity in the material above the given reflector can be evaluated. With the CMP method and Equations D-1 and D-2, it is possible to calculate the relative permittivity of the soil and thereafter, the moisture content at diverse position in the slope.

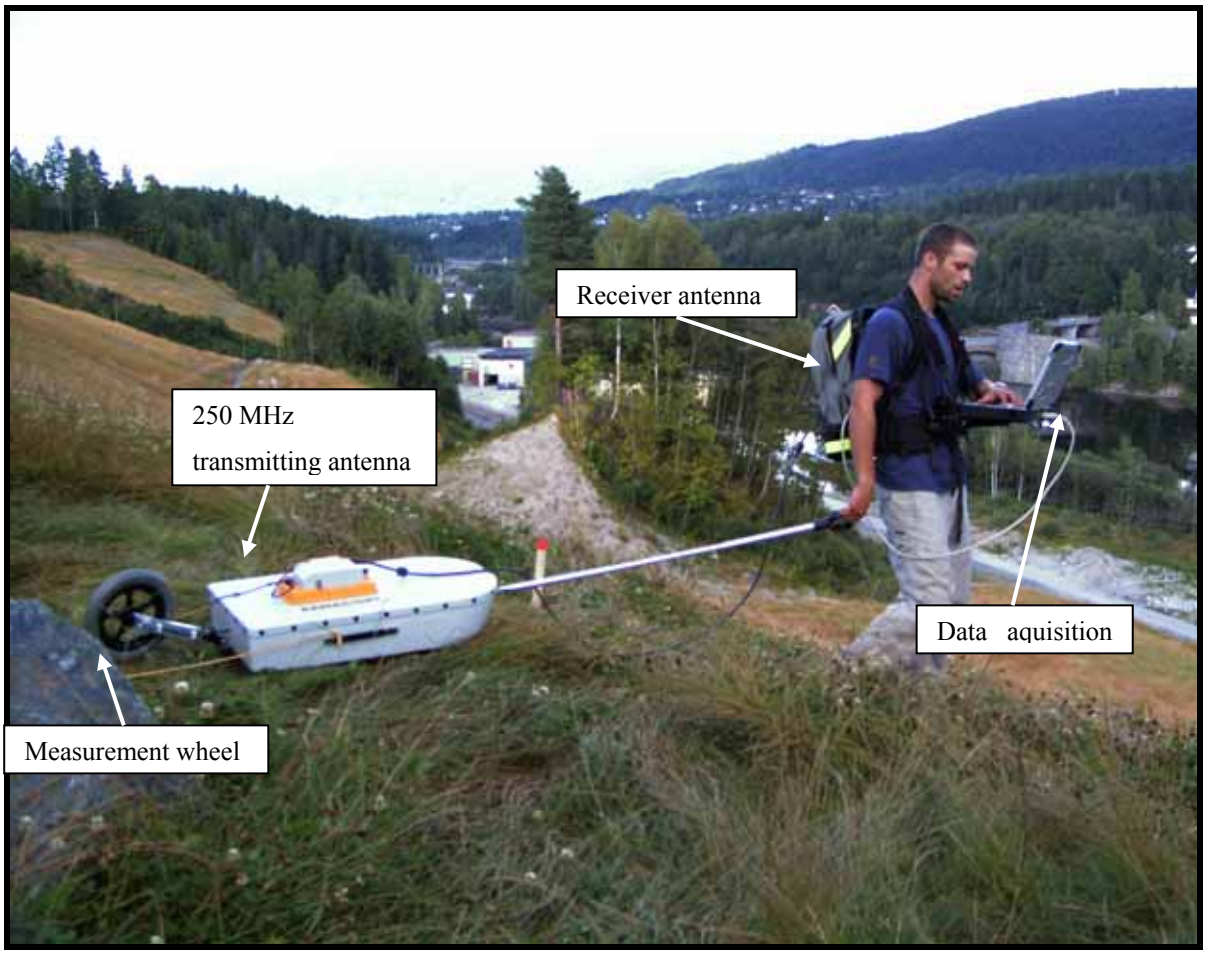

Figure D-1: Ground penetrating radar instrument. Measurements using the reflexion survey mode.

APPENDIX E Ground Penetrating Radar Results

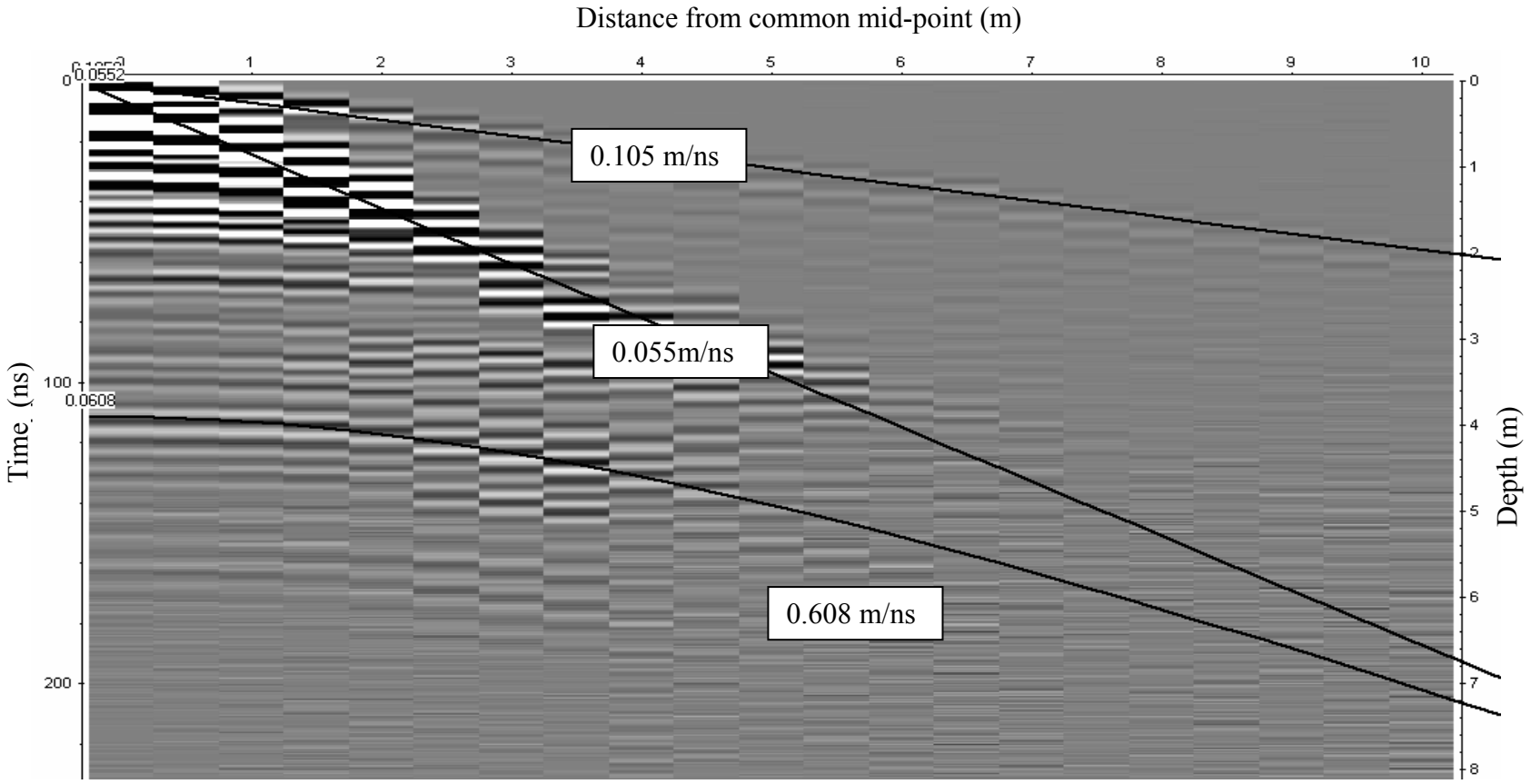

Figure E-1: Radargram from common-mid point surveying. Profile acquired at the bottom of the slope with a 100 MHz unshielded antennae.

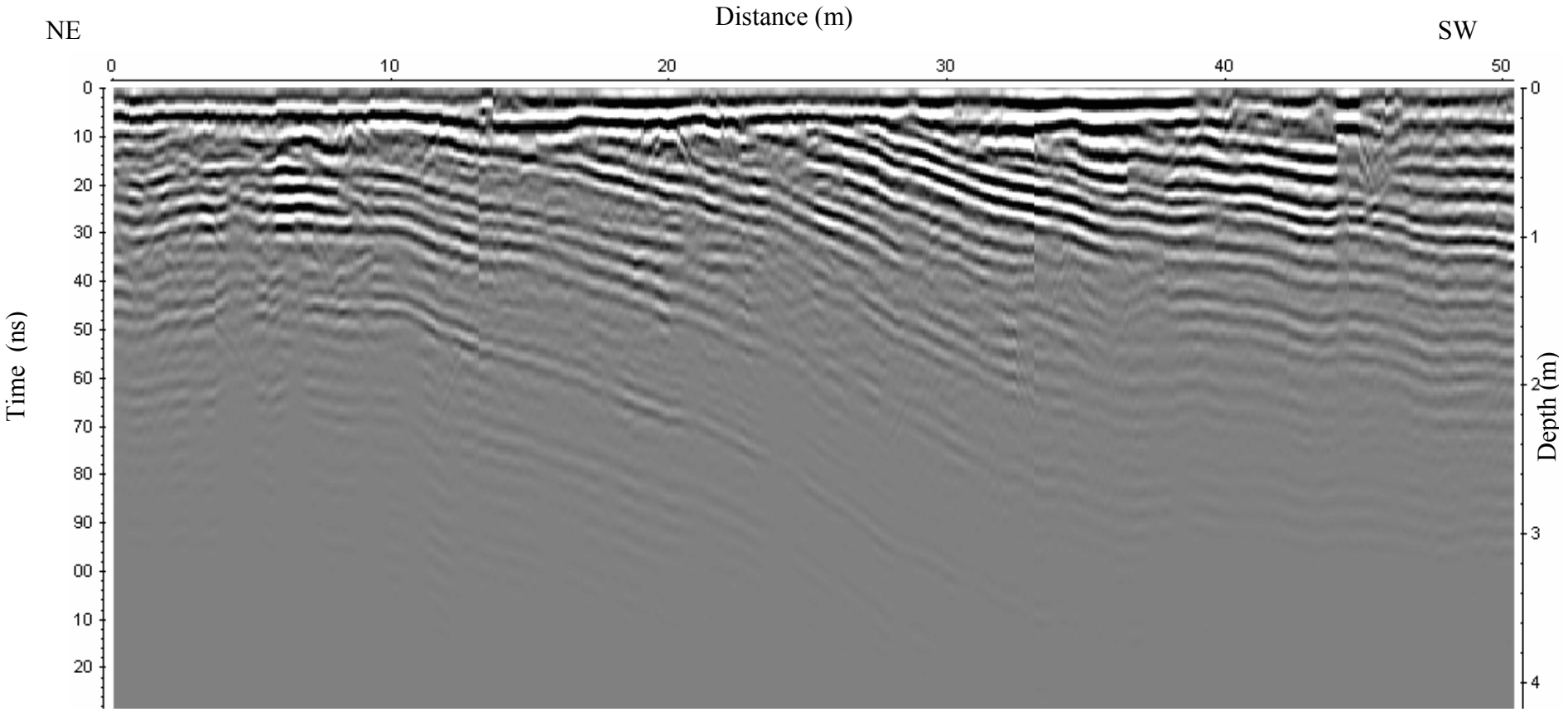

Figure E-2: Radargram from reflexion profile. Profile acquired on the plateau of the slope with a 250MHz shielded antennae.(Scale of 2H for 1V)

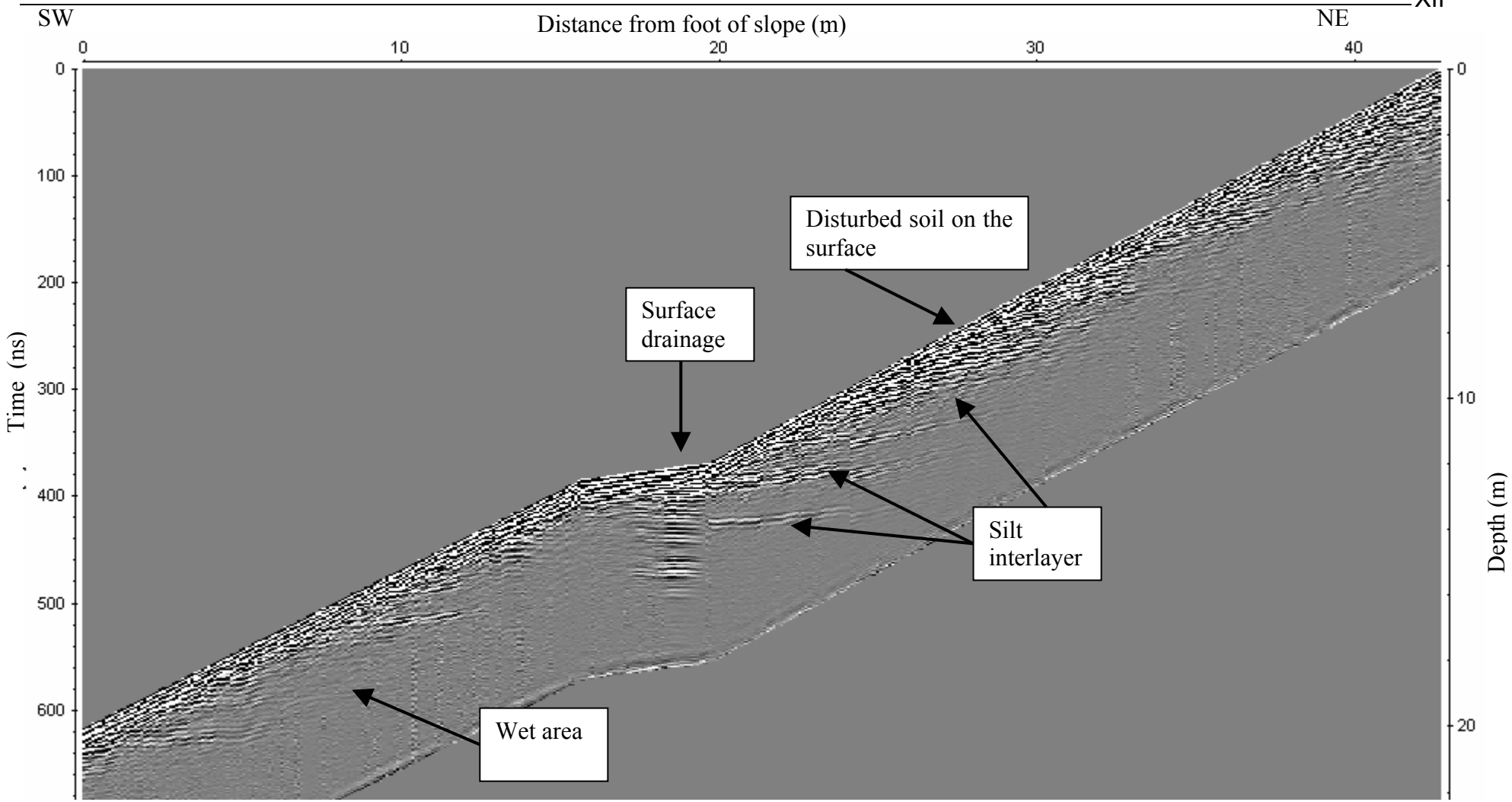

Figure E-3: Radargram from reflexion profile. Profile acquired along the slope at position x=0 with a 250MHz shielded antennae.(Scale of 1H for 1V).

APPENDIX F Electrical Resistivity

Electrical resistivity measurements of earth materials involve the introduction of an electric current into the ground and the measurement of the material resistance to the induced current. There are several variants of resistivity measurement methods. In this work, a method using a capacitively-coupled resistivity system was used.

F.1 OhmMapper description

The OhmMapper, from the company Geometrics Inc., is a capacitively-coupled resistivity meter designed to measure subsurface electrical properties of rocks and soil. It consists of an ungrounded dipole transmitter and receivers. Instead of using point electrodes like in the most common setups, line electrodes are used. These capacitively couple to the soil over their entire length. The simple coaxial array with the transmitter and receivers is pulled along a survey line by a single person. Data acquisition is performed by the Geometrics Data mapper console. In this method, an alternating current is capacitively coupled into the earth at a particular frequency by the voltage applied to the transmitting dipole. The resulting alternative voltage coupled to the receiver's dipole is measured at defined intervals length along the survey line.

The configuration of the OhmMapper is shown on Figure F-1. This arrangement is called a dipole-dipole configuration, where the transmitter and receivers are placed in line and separated by a number of dipole length.

The apparent resistivity (ρ_a) of a medium can be given by the following:

$$\rho_a = K\frac{\Delta V}{I} \qquad \textbf{Equation F-1}$$

where (ΔV) is the difference of potential between the transmitting and receiving dipole, (I) is the total current and (K) is a geometric factor which is function of the configuration and the space between the transmitting and receiving dipole. For the dipole-dipole configuration, Equation F-1 can be written as:

$$\rho_a = 2\pi \cdot n(n+1)(n+2)a\left(\frac{\Delta V}{I}\right) \qquad \textbf{Equation F-2}$$

In Equation F-2, (a) is the distance of separation between the potential and current dipole and (n) is the ratio between the rope length and the dipole length.

The apparent resistivity of the soil depends essentially on the following physical properties:

- Mineral concentration in pore-water
- Porosity of the soil
- Degree of saturation
- Clay content
- Temperature of the pore-water

Due to these properties and to the fact that the natural soil is not a homogenous and isotropic medium, electrical variations along the survey profile will appear.

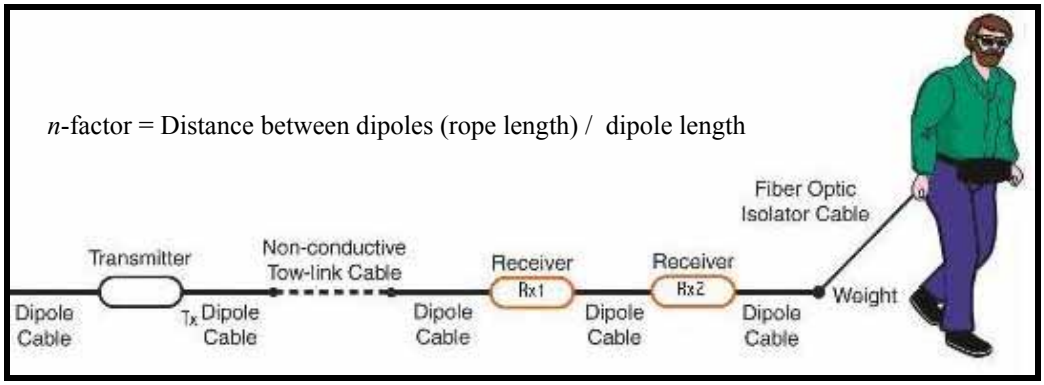

Figure F-1: Presentation of the OhmMapper configuration from www.geometrics.com

F.2 Data Collection Methodology with the Ohm-Mapper

The Ohm-Mapper apparatus was set to sample data every 0.5 seconds. Mark spacing was used every 2 m. With these mark points, the software can correctly position the data at even intervals between the marks. Multiple parallel lines with a 2 m separation were used to survey the slope (lines shown in Figure C-1).

In order to obtain depth pseudo-sections, multiple passes were required on each survey line. Every pass was conducted with a different dipole configuration. Data were acquired with 5 and 10 m dipoles and the space between the receiver and transmitter dipole could be changed from 2.5 to 30 m. The ratio between the distance of receiver and transmitter dipole to the dipole length is called the *n*-factor (see Figure F-1). This factor was varied from 0.5-3 in the acquisition procedure. The n-factor is directly related to the depth of investigation.

It was difficult to make passes with high n factors along the slope due to space constraint. In fact, for a configuration where the *n*-factor=3 (i.e. dipole of 5 m and 15 m of rope) the whole array length reached over 28 me. For the same configuration and the 10 m dipoles, the length of the array reached 53 m. Since the slope length is only 48 m, not many data were collected with high *n*-factors configuration. The depth of the pseudo-section within the slope is therefore not as great as one could wish, but is sufficient to see shallow surface details.

APPENDIX G Electrical Resistivity Results

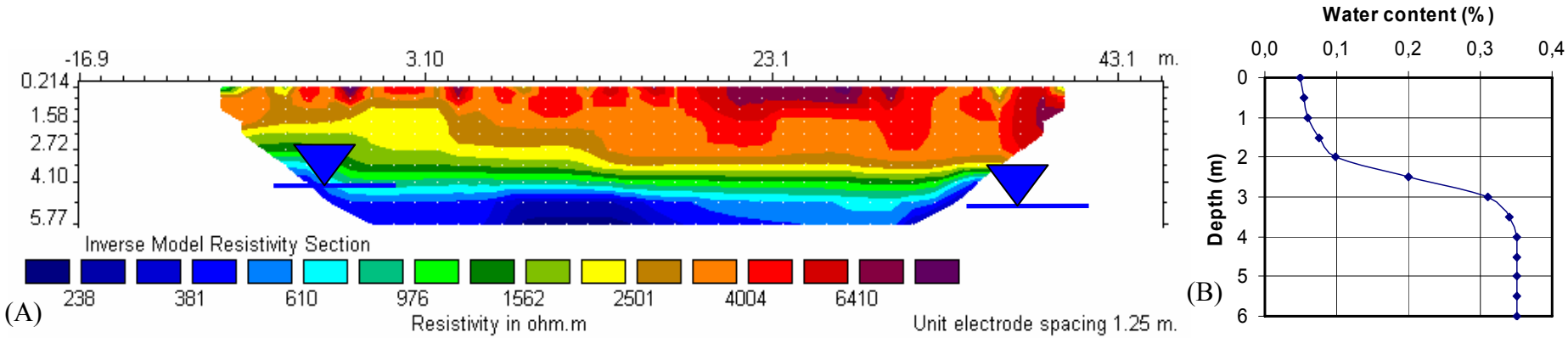

Figure G-1: (A)-Resistivity inversion results on the plateau above the slope (130m from crest of the slope). (B) Assumed corresponding volumetric water content profile.

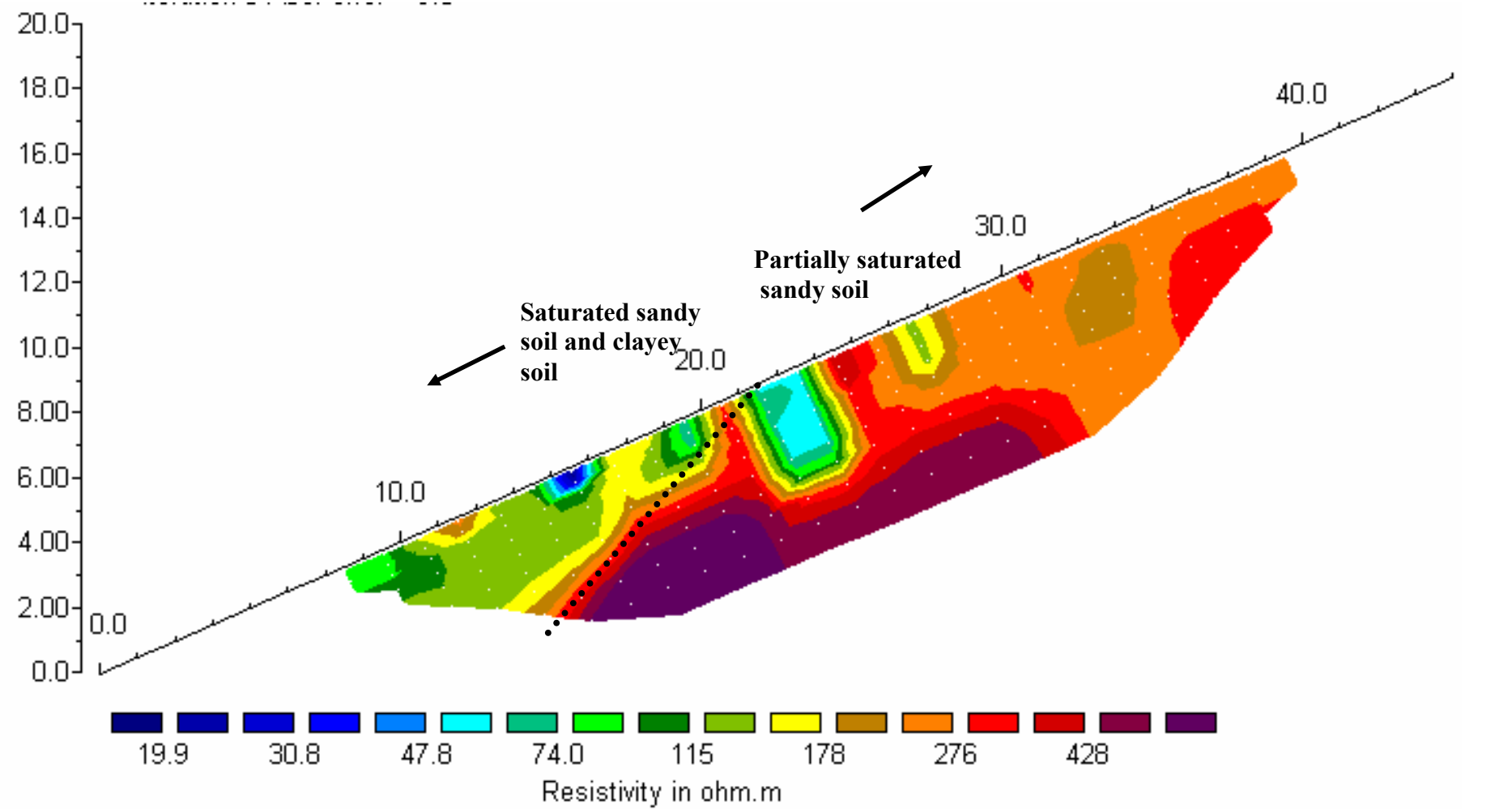

Figure G-2: 2-D resistivity inversion results along the slope at position x=0m.

APPENDIX H Laboratory Results-The Åmot Sand

H.1 Grain Size Distribution Curve

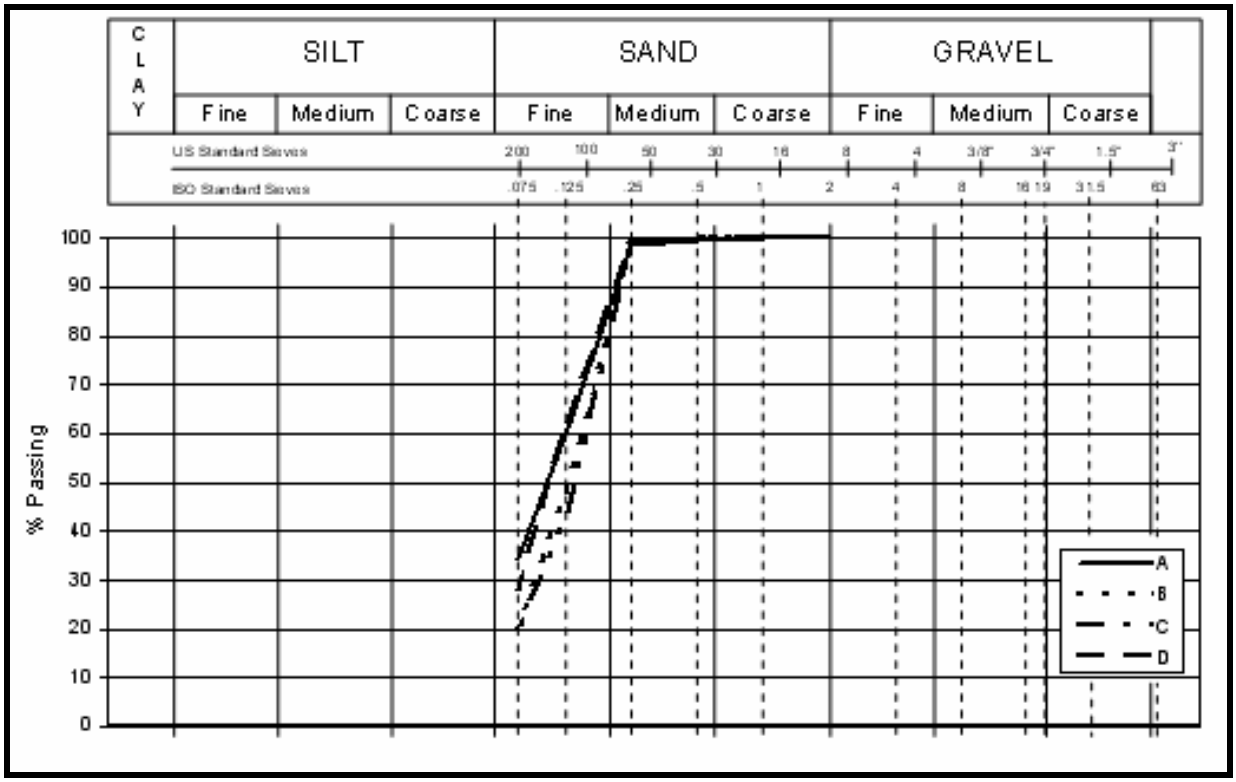

Figure H-1: Grain size distribution curve for the Åmot sand (dry sieving only).

H.2 Soil-water characteristic results (Tempe Pressure Cell)

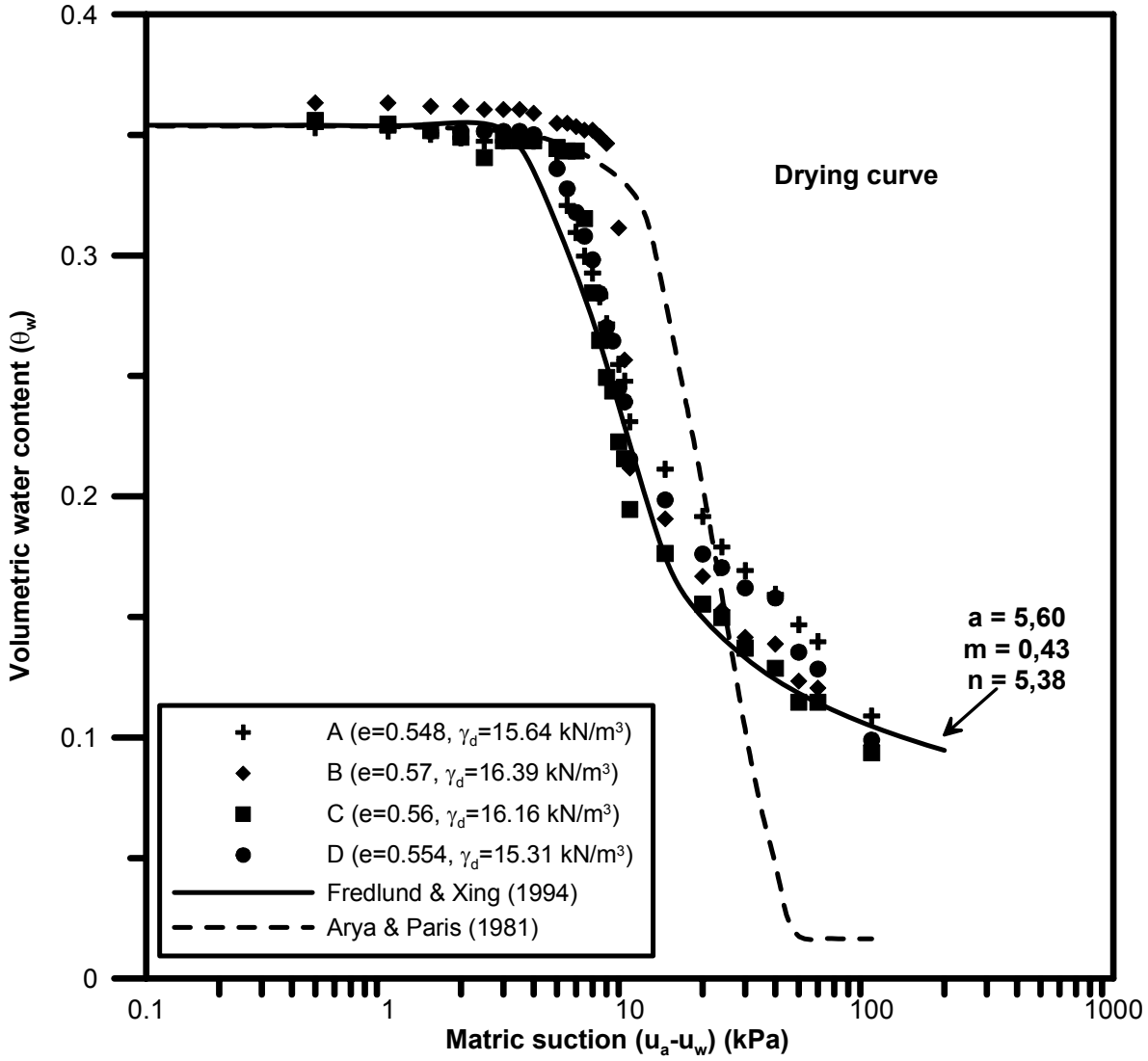

Figure H-2: Soil-water characteristic curve for a fine sand from Åmot, Modum. (Series #1)

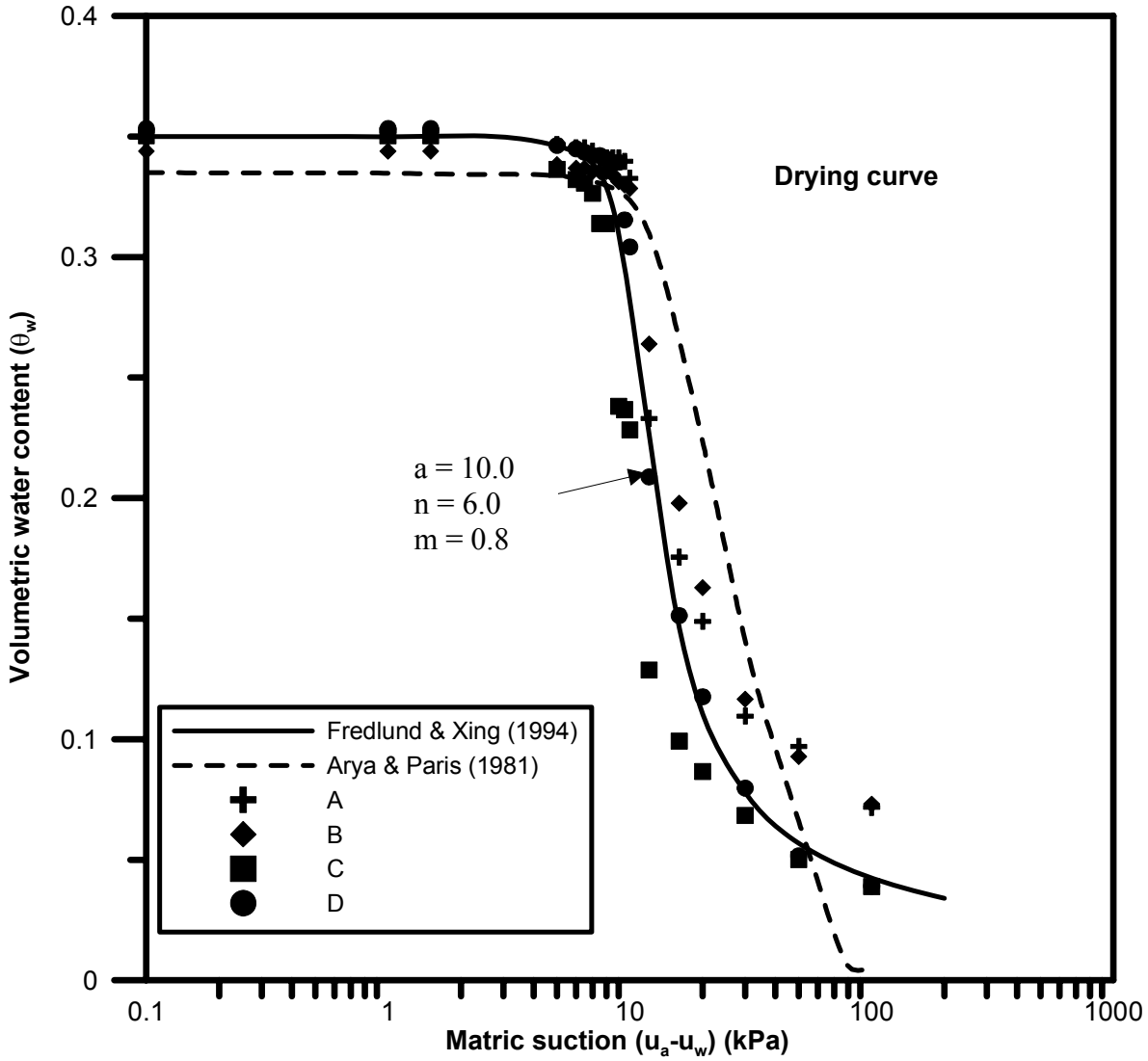

Figure H-3: Soil-water characteristic curve for a fine sand from Åmot, Modum. (Series #2)

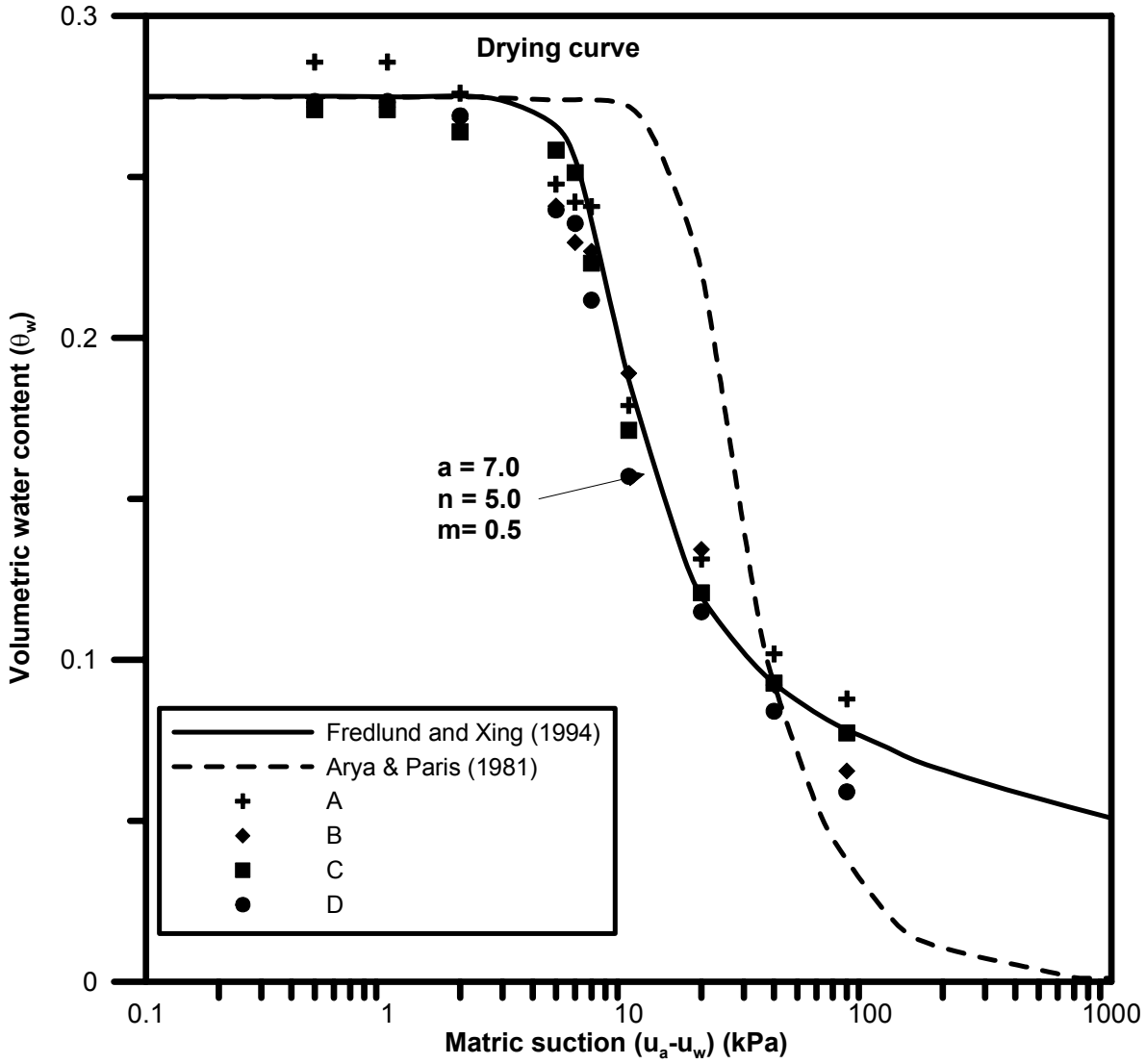

Figure H-4 Soil-water characteristic curve for a fine sand from Åmot, Modum. (Series #3).

H.3 Saturated hydraulic conductivity results (Constant-head experiment)

Table H-1: Constant-head permeability test results for the sand from Åmot (1st series).

Reading on burette (ml)	Δ V (cm^3)	Time (min)	ΔT_i (sec)	q (cm^3/s)	L (cm)	h (cm)	A (cm^2)	Gradient (i)	k (cm/s)	k (m/s)
25	0	0	0		2	67,5	35	33,75		
24,6	0,4	1	60	0,0067					5,64E-06	5,64E-08
24,2	0,4	2	60	0,0067					5,64E-06	5,64E-08
23,9	0,3	3	60	0,0050					4,23E-06	4,23E-08
23,6	0,3	4	60	0,0050					4,23E-06	4,23E-08
23,3	0,3	5	60	0,0050					4,23E-06	4,23E-08
23	0,3	6	60	0,0050					4,23E-06	4,23E-08
22,65	0,35	7	60	0,0058					4,94E-06	4,94E-08
22,3	0,35	8	60	0,0058					4,94E-06	4,94E-08
22	0,3	9	60	0,0050					4,23E-06	4,23E-08
21,7	0,3	10	60	0,0050					4,23E-06	4,23E-08
									$K_{avg.}$ =	4,66E-08

Table H-2: Constant-head permeability test results for the sand from Åmot (2nd series).

Reading on burette (ml)	Δ V (cm^3)	Time (min)	ΔTi (sec)	q (cm^3/s)	L (cm)	h (cm)	A (cm^2)	Gradient (i)	k (cm/s)	k (m/s)
23,8	0	0	0		2	67,5	35	33,75		
22	1,8	1	60	0,03					2,54E-05	2,54E-07
20,2	1,8	2	60	0,03					2,54E-05	2,54E-07
18,4	1,8	3	60	0,03					2,54E-05	2,54E-07
16,6	1,8	4	60	0,03					2,54E-05	2,54E-07
14,6	2	5	60	0,03					2,82E-05	2,82E-07
12,8	1,8	6	60	0,03					2,54E-05	2,54E-07
N.B : Washing of fine particles									$K_{avg.}$ =	2,59E-07

Table H-3: Constant-head permeability test results for the sand from Åmot (3rd series).

Reading on burette (ml)	Δ V (cm^3)	Time (min)	ΔTi (sec)	q (cm^3/s)	L (cm)	h (cm)	A (cm^2)	Gradient (i)	k (cm/s)	k (m/s)
19,5	0	0	0		2	67,5	35	33,75		
18,1	1,4	1	60	0,023					1,97E-05	1,97E-07
16,9	1,2	2	60	0,02					1,69E-05	1,69E-07
15,8	1,1	3	60	0,0183					1,55E-05	1,55E-07
14,7	1,1	4	60	0,0183					1,55E-05	1,55E-07
13,6	1,1	5	60	0,0183					1,55E-05	1,55E-07
12,5	1,1	6	60	0,0183					1,55E-05	1,55E-07
									$K_{avg.}$ =	1,64E-07